Bichromatic State-Independent Trapping of Caesium Atoms

Mukaddes Meliz Metbulut

A thesis submitted to the University College London
in partial fulfilment of the requirements for the
degree of Doctor of Philosophy

Department of Physics and Astronomy
University College London
April 2016

I, Mukaddes Meliz Metbulut, confirm that the work presented in this thesis is my own. Where information has been derived from other sources, I confirm that this has been indicated in the thesis.

Signed ..... Date.....

Abstract

State-insensitive trapping plays a significant role in many cold atom experiments. In this technique, trapping at a specific "magic" wavelength leads to identical shifts of the ground and excited states of a particular transition. Hence, the internal state of the trapped atoms remains essentially unaffected by the trapping light. This leads to increased coherence times and loading efficiency, and allows for the use of free-space manipulation techniques. However, the applicability of state-insensitive trapping is limited in terms of light sources available, with restrictions coming from either the required frequency or power. In this thesis, state-insensitive trapping of caesium atoms is considered. It can be achieved at the wavelength of 935.6 nm. However, the present work shows that this wavelength is impractical for experimental realizations of atom trapping in free space due to lack of laser sources with sufficiently high power. We therefore propose bichromatic trapping, as produced by two independent laser fields with different frequencies, to overcome the limitations related to monochromatic trapping. We show that bichromatic trapping extends the range of possible magic wavelengths compared to the specific magic wavelength associated with monochromatic trapping. Specifically, we present results for the magic wavelength combinations for caesium atoms with particular attention to the frequency range of currently available laser sources. Simultaneous state-independent trapping of atomic mixtures of caesium with rubidium and lithium atoms was also investigated, and appropriate magic wavelength combinations were identified. Additionally, species-selective state-independent trapping of atomic mixtures of caesium and lithium was explored and common wavelength pairs for tune-out and magic wavelengths of these atoms were determined.

To my family

Acknowledgements

At first I would like to thank Prof Ferruccio Renzoni for the opportunity to complete my PhD in his group. Without his patient guidance and encouragement, the work in this thesis would not have been possible.

I would also like to thank my predecessor Dr. Piyaphat Phoonthong for introducing me to the experiment and teaching the basic knowledge after I joined the lab. Thanks also to the other past and present group members Dr. Nihal Wahab, Dr. Arne Wickenbrock, Dr. Luca Marmugi, Soliman Eidris, Raffaele Nolli and Michela Venturelli who have helped me in one way or another. I thank Rafid Jawad for repairing a lot of the equipment and solving lot of electrical problems for me always with patience.

I owe my deepest gratitude to my sister Pınar Metbulut, my brother Berk Aktuğ and particularly my parents Cansev and Mustafa Metbulut, for their unconditional love and support throughout my PhD. My parents support and understanding was invaluable for me. Finally, I would like to express special thanks to my mother and my grandmother Mukaddes Özgün for always supporting me and teaching a lot throughout my life.

Contents

List of Tables

List of Figures

Chapter 1

Introduction

In 1905 Einstein's breakthrough prediction for the quantum theory of light has led to an idea for manipulating the atoms. Light is a source of quantized energy carrying momentum that can be transferred to/from atoms to manipulate both their internal and external degrees of freedom. The advent of the laser has revolutionized many fields of science. In particular, most significant development was achieved in atomic physics with laser cooling of atoms. Indeed, it opened a door to a new research field: cold atoms. The pioneers of the field were awarded the Nobel prize in 1997 [1–3] and 2001 [4, 5]. Currently, the study of cold atoms is one of the rapidly expanding research areas as it plays an important role both in fundamental and applied physics; such as optical clocks and quantum information systems.

The idea of laser cooling was proposed by Hänsch and Schawlow [6] in 1975. They suggested to use velocity dependent radiative forces to reduce the atomic velocity by means of the Doppler effect. The Doppler cooling method relies on the dissipation of thermal energy of the atoms via momentum exchange with the laser radiation. In this technique counter-propagating beams red-detuned with respect to atomic resonance are used and thereby an atom moving faster sees a stronger force opposing its motion leading to a net velocity dependent force opposing its motion. The first experimental demonstration of this technique was done with magnesium [7] and barium [8] ions. Later in 1980s two milestones were achieved for neutral atoms. First

was the experimental demonstration of optical molasses by Chu *et* al. [9]. He showed cooling of sodium atoms via Doppler cooling by using three counter-propagating beams in perpendicular configuration. Although the atoms in optical molasses are cooled to very low temperatures, they are not confined. Another milestone was the demonstration of magneto-optical trapping technique by Raab *et* al. in 1987 [10], which is based on the combination of the velocity and position dependent radiative forces for cooling and confinement respectively. Currently it is the starting point of all experiments to prepare high density of cold atoms due to its ability to both cool and trap atoms simultaneously. Several years after implementing the optical molasses, anomalous cooling of atoms was observed. At that time it was believed that the lowest achievable temperatures is limited by the Doppler temperature limit. However, lower temperatures beyond this limit were observed. This conflict was solved by the identification of sub-Doppler cooling mechanisms, which rely on the polarization gradient and optical pumping effects. Another cooling method, evoparative cooling, involves lowering the trap depth to allow hotter atoms to escape and thus cooling the remaining atoms via rethermalization.

Another technique of trapping atoms is optical dipole trap. It relies on the interaction between the atoms and a light field, whose intensity varies with space. This interaction leads to the so-called dipole force. The dipole force was first theoretically investigated by Askaryan in 1962 [11] and experimentally demonstrated by Bjorkholm in 1978 [12]. Later in 1986, Chu experimentally realized the first optical dipole trap of neutral atoms [13]. Essentially, the optical dipole trap employs the AC Stark shift produced by tightly focused beam, which leads to a trapping potential for the atomic ground state. In contrast to other trapping mechanisms it provides a potential independent of hyperfine state and spin projection of an atom [14, 15]. Therefore, it allows use of arbitrary magnetic fields and different hyperfine levels. Moreover, the use of far-off resonance dipole trap (FORT) ensures low scattering rates allowing long coherence times [15].

Recent progress in manipulation of atoms in optical dipole trap has attracted great interest as it offers a wide range of applications. Recent studies included the production of Bose-Einstein condensation [16], degenerate Fermi gases [17] and Fermi-Bose mixtures [18, 19]. However, in general the differential AC Stark shift induced between the different internal states of the trapped atom present several drawbacks. For instance, it causes decoherence significantly limiting the coherence time [20], which is an important parameter in experiments involving quantum state manipulation [20]. Moreover, it causes a line shift and its spatial dependence leads to a line broadening that makes continuous monitoring of trapped atoms difficult. It also affects the application of free space laser cooling techniques, and thus the efficiency of transferring atoms from a magneto-optical trap into a dipole trap. In fact, cooling is essential for an optical dipole trap not only for long storage times but also for avoiding motion-induced dephasing of the atoms [21, 22].

A solution to these problems was proposed by Katori [23]. He suggested tuning the trapping laser to a "magic" wavelength in a way that the differential light shift vanishes. Motivated by this, we performed calculations for light shift of the caesium atom and identified magic wavelengths providing state-insensitive trapping. However, in some cases state-insensitive trapping is impractical in terms of experimental realization due to lack of light sources at the required frequency or with sufficient power. Bichromatic trapping schemes involving the combination of trap and control laser was proposed to overcome the limitation imposed by single frequency state-insensitive trapping.

In this work, bichromatic state-insensitive trapping of Caesium atom was investigated and a set of magic wavelength combinations accesible by high power lasers were identified. Moreover, a further step for experimental implementation of state-insensitive bichromatic trapping scheme is described. Due to recent experiments on simultaneous trapping of two different atomic species, we extended the investigation of state-insensitive trapping to mixtures of atomic species and determined the magic wavelength sets producing simultaneous state-insensitive trapping of these species. The formalism to obtain the required equation to compute the AC Stark shift is described. All

the calculations were carried out using the mathematica software. Uncertainties in the input parameters of the calculations resulted in a negligible (well below 1%) uncertainty in identified magic wavelength combinations such that they have no effect on realization of the bichromatic state-insensitive trap.

This thesis is organized as follows. In chapter 2 the theory behind the laser cooling and trapping is presented. Our experimental setup including the vacuum system, the light sources, the imaging system and a further step to experimentally implement state-insensitive bichromatic trapping is described in chapter 3. Chapter 4 presents the investigation for bichromatic state-insensitive trapping of caesium atoms. Then chapter 5 and 6 numerical calculations for simultaneous state-insensitive trapping of caesium-rubidium and caesium-lithium mixtures are presented. Finally in the last chapter, the results are summarized and proposals for related future experiments are given.

Chapter 2

Laser Cooling and Trapping

The invention of lasers has revolutionized the field of atomic physics. Their use for manipulating and trapping atoms opened a new research area: cold atom physics. The use of laser for cooling atoms was first proposed in 1975 by Hänsch and Schawlow [6]. Later in 1985 laser cooling was experimentally demonstrated [9]. Then, magneto-optical trapping (MOT) was demonstrated in 1987 [10]. This has become a prerequisite as a cold atom source for various experiments. In this chapter the principles of laser cooling and trapping of neutral atoms are presented. It begins with briefly describing the light forces on atoms. Then it continues with examining the fundamental concepts of optical molasses, magneto-optical trap and dipole trap.

2.1 Light Forces on Atoms

There are two types of forces an atom can experience in a light field: the *scattering force (radiation pressure force)* and the *optical dipole force*. The former force results from the isotropic scattering of photons from a near resonance laser field. It is a dissipative force, hence it provides cooling of atoms. The latter force originates from the interaction between the induced atomic dipole moment of the atom and the laser field. This force is a conservative force, therefore it provides trapping. In this section, these forces are discussed.

2.1.1 Scattering Force

The scattering force or radiation pressure force relies on the conservation of momentum. When a two-level atom is interacting with a laser field having frequency close to the resonant frequency of the atomic transition, the atom absorbs photons from the laser field and becomes excited. Due to the conservation of momentum, there is a momentum transfer between the atom and the photons associated with the absorption and emission. In the absorption process, the momentum of the absorbed photon $\hbar k$ is transferred to the atom which thus acquires a momentum $\hbar k$ in the direction of the incoming laser beam. As the atom in the excited state is unstable it decays back to the ground state by emitting a photon. In the case the atom decays by stimulated emission the photon is emitted with the same direction as the incoming laser beam. Hence, the absorption and stimulated emission processes do not change the momentum of the atom. On the other hand, if it decays by spontaneous emission, the photon is emitted randomly in all directions. Due to the isotropic nature of the process the average change in momentum of the atom is zero. Consequently, the net momentum transfer from spontaneously emitted photons averages to zero over many absorption-emission cycles. Therefore, the scattering of photons leads to a net force in the propagation direction of the laser beam, that results in a decrease of the velocity of the atom in the opposite direction. The magnitude of this *scattering force* is calculated as product of the momentum of each absorbed photon $\hbar k$ and the photon scattering rate Γ_{scatt} and given by,

$$F_{scatt} = \hbar k \Gamma_{scatt}. \tag{2.1}$$

The photon scattering rate depends on the frequency, intensity of the laser field and the natural linewidth of the atomic transition Γ and it is given

by,

$$\Gamma_{scatt} = \frac{\Gamma}{2}\frac{s_0}{1+s_0+4(\frac{\Delta}{\Gamma})^2}, \tag{2.2}$$

where

$$s_0 = \frac{I}{I_s} = 2\frac{\Omega}{\Gamma}^2, \tag{2.3}$$

$$\tag{2.4}$$

$$\Omega = \frac{\langle g|\mathbf{d}\cdot\mathbf{E}|e\rangle}{\hbar}. \tag{2.5}$$

Here I is the laser intensity, $I_s = \frac{\hbar\Gamma\omega_0^3}{12\pi c^2}$ is the saturation intensity, $\Delta = \omega_L - \omega_0$ is the frequency detuning of the laser field from the atomic resonance, Ω is the Rabi frequency, $\mathbf{d}$ is the electric dipole moment and $\mathbf{E}$ is the electric field of the light. As equation 2.5 shows the Rabi frequency is associated with the strength of the coupling between the light field and the transition from the ground state $|g\rangle$ to the excited state $|e\rangle$ of the atom.

Thus the scattering force can be written as

$$F_{scatt} = \hbar k\frac{\Gamma}{2}\frac{s_0}{1+s_0+4(\frac{\Delta}{\Gamma})^2}. \tag{2.6}$$

At high intensities ($I \gg I_s$) the scattering force saturates to a limiting value of $F_{max} = \hbar k\frac{\Gamma}{2}$. In addition to its intensity dependence, if the atom is moving towards the beam with a velocity v instead of being at rest, then the detuning of the laser beam from the atomic resonance "seen" by the atom is Doppler shifted to $\Delta + kv$. Therefore the scattering rate and subsequently the scattering force become velocity dependent leading to dissipation and

cooling. In this case the scattering force can be expressed as

$$F_{scatt} = \hbar k \frac{\Gamma}{2} \frac{s_0}{1 + s_0 + 4(\frac{\omega_L - \omega_0 + kv}{\Gamma})^2}. \tag{2.7}$$

2.1.2 Optical Dipole Force

The dipole force is determined by the interaction between the induced atomic dipole moment of the atom and the spatially varying intensity of the light field. The dipole potential originates from the shift in energy levels of an atom placed in an oscillating electric field. This shift is termed the AC Stark shift. The gradient of this shift leads to a dipole force. The energy shift can be expressed as [24]

$$\Delta E = \frac{\hbar \Omega^2}{4\Delta}, \tag{2.8}$$

where Δ is the detuning of the laser field from atomic resonance and Ω is the Rabi frequency. The equation 2.8 indicates that the magnitude of the energy shift depends both on the intensity of the light field and its coupling with the transition. When the intensity of the light field is not spatially homogeneous, there is gradient of energy shift leading to the optical dipole force. Depending on the sign of the detuning of the light field, the dipole force is either attractive or repulsive. For red detuning of the light field ($\Delta > 0$) the atoms are attracted to the higher intensity region, while they are repelled from it for blue detuning of the light field ($\Delta < 0$). The dipole force is a conservative force, unlike the scattering force, and it can confine the atoms in the focus of a laser beam. A more detailed discussion about the dipole force and potential is presented in section 2.5.

2.2 Optical Molasses

In laser cooling and trapping experiments the scattering force is used to cool atoms utilizing a technique called *Doppler Cooling*. This technique was first suggested by Hänsch and Schawlow in 1975 [6]. As its name implies it is based on the Doppler effect which leads to a frequency shift of a laser beam experienced by a moving atom. Therefore, Doppler cooling produces a velocity dependent scattering force in a way that faster moving atoms experience a larger force opposing their motion. This process can be explained by focusing on the one dimensional case where an atom is moving with velocity v and is illuminated by two red detuned counterpropagating laser beams collinear with the direction of motion. The frequency detuning from the atomic resonance for the beam propagating in the same direction as the atom is Doppler shifted to $\Delta - kv$, whereas it is $\Delta + kv$ for the beam propagating in opposite direction. In other words, the Doppler shift brings the atom closer to resonance with the counterpropagating laser beam, while it brings the atom further away from the resonance with the copropagating laser beam. This leads to an imbalance in the scattering rates caused by the each beam. Since the moving atom absorbs more photons from the beam in opposite direction to its motion, there is a net momentum transfer between atom and laser beam opposing its motion. Thus, a moving atom experiences a net force opposing its motion as shown in figure 2.1.

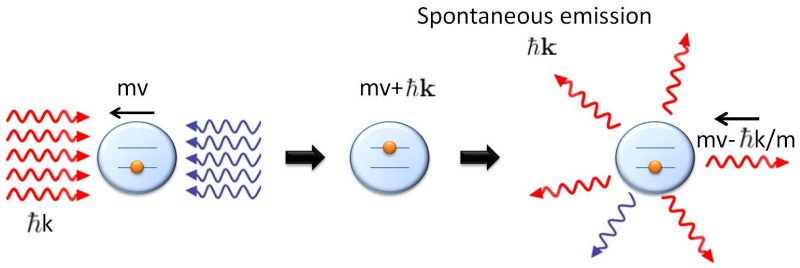

Figure 2.1: An atom moving with velocity v absorbs a photon with momentum ħk from the beam propagating in opposite direction to its motion. After absorbing the photon it becomes excited. Then with spontaneous emission in random direction it decays back to ground state and its momentum decreases due to recoil.

This can be mathematically expressed by the difference of scattering force from each laser beam

$$F_{molasses} = \hbar k \frac{\Gamma}{2} \left(\frac{s_0}{1 + s_0 + 4(\frac{\omega_L - \omega_0 - kv}{\Gamma})^2} - \frac{s_0}{1 + s_0 + 4(\frac{\omega_L - \omega_0 + kv}{\Gamma})^2} \right). \quad (2.9)$$

In the limit of low velocities ($kv \ll \Gamma$) the equation 2.9 can be simplified by expanding it in Taylor series in first order in v to obtain

$$F_{molasses} \approx -8\hbar k^2 v s_0 \left(\frac{\Delta}{\Gamma \left(1 + s_0 + 4\frac{\Delta}{\Gamma}\right)^2} \right), \quad (2.10)$$

which is a damping force. As it is velocity dependent, the energy loss of the atoms results in cooling. This force can be expressed in the form of

$$F_{molasses} = -\alpha v, \quad (2.11)$$

where α is the damping coefficient. The equation 2.11 shows that for small velocities the net force exerted by laser beams is linearly proportional to the velocity, which is analogous to the drag force experienced by an object moving in a viscous liquid. Inspired by this analogy, this technique was named as *optical molasses* and first demonstrated experimentally in three dimensions by Chu et al in 1985 [25].

When an atom decays by spontaneous emission, photons are emitted isotropically. So the net momentum transfer averages to zero over many absorption-emission cycles. Although the net force due to spontaneous emission is zero, fluctuations accumulate. Since the spontaneous emission occurs isotropically, an atom recoils in random directions leading to a random walk in velocity space. In consequence, spontaneous emission causes heating. According to the equation 2.10 if there is no other influence on the motion of atoms except from the molasses force, then the velocity of the atoms can decelerate to zero and subsequently they can reach the temperature of 0 K

which would violate the laws of thermodynamics. However, if the heating due to spontaneous emission is taken into account, there is a limit on the lowest obtainable temperature by the optical molasses technique which is called the Doppler cooling limit. This limit is reached when the rate of cooling is equal to the rate of heating. The Doppler cooling limit as calculated by setting the heating and the cooling rates equal is

$$T_D \approx \frac{\hbar\Gamma}{2k_B}, \tag{2.12}$$

where k_B is the Boltzmann constant. The equation 2.12 shows that the Doppler cooling limit is determined by natural linewidth of the cooling transition. The natural linewidth of the caesium (Cs) atom is $\Gamma = 2\pi \times 5.22\text{MHz}$, hence its temperature limit corresponds to $125\mu\text{K}$. The Doppler cooling limit was obtained with the assumption of nondegenerate two-level system in the presence of homogeneous laser field. In reality, counterpropagating laser beams with $\sigma^+ - \sigma^-$ or lin$\perp$lin polarization configurations are used which creates inhomogeneous fields. Furthermore, in the absence of external magnetic fields the atomic states are degenerate. Therefore the temperature of atoms can be lower than the Doppler limit in optical molasses as shown theoretically in [26] and experimentally in [27]. This will be explained in the following.

As free atoms in a vapour move in all directions, the use of optical molasses in all three orthogonal directions is required. This is easily achieved by extending the molasses scheme to three dimensions by using three pairs of counterpropagating beams along three orthogonal axes. These beams are obtained from a single laser source so that they all have the same frequency. Furthermore, each counterpropagating beam has approximately the same intensity so not to set the atoms into directed motion.

2.3 Sub-Doppler Cooling

In the previous section it was established that Doppler cooling leads to the formation of optical molasses. However, it was experimentally observed that it is possible to reach temperatures below the Doppler cooling limit [27] indicating the existence of other cooling mechanisms in addition to Doppler cooling. These new cooling mechanisms are referred as sub-Doppler cooling or polarization gradient cooling. These sub-Doppler cooling processes provide temperatures close to the recoil limit.

In the previous section, Doppler cooling was explained based on two assumptions. Firstly, the two counterpropagating laser beams were treated independently, hence neglecting the possibility of interference between beams. However, interference of these two-counterpropagating beams may produces a polarization gradient pattern. This results in spatially varying light shifts of atomic energy levels. Secondly, a nondegenerate two-level model of atom was considered which does not reflect the structure of real atoms. Indeed, alkali atoms like caesium atom are multi-level atoms having hyperfine structure with magnetic sublevels. Taking into account these two factors and incorporating the optical pumping between groundstate sublevels the cooling mechanism can be explained more accurately.

In sub-Doppler cooling, there are two important polarization configurations for two counterpropagating laser beams: the lin$\perp$lin and the $\sigma^+ - \sigma^-$ configuration. Both of these configurations lead to temperatures below the Doppler limit but the mechanisms for reaching these temperatures are different.

lin$\perp$lin Configuration

In this configuration, atoms interact with two linear orthogonally polarized counterpropagating laser beams. The resultant polarization of the total field depends on the relative phase of the two counterpropagating laser beams and thus varies spatially. It changes from linear (horizontal) to σ^- to linear (vertical) to σ^+ and back to linear (horizontal) again, with a spatial period equal to half of the laser wavelength as shown in figure 2.2.

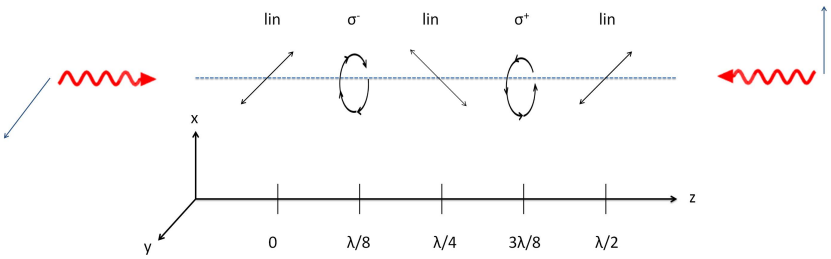

Figure 2.2: The polarization gradient of a standing wave in lin⊥lin configuration. The polarization of the standing wave changes from σ^- to σ^+ in a quarter laser wavelength.

This polarization gradient has a significant effect on the magnitude of the light shifts of the magnetic sublevels of the atom. This polarization gradient leads to periodic spatial variation of the light shifts, and an atom moving through this laser field experiences different light shift potentials depending on its internal state. The strength of these light shifts are determined by the transition rates between the magnetic sublevels which are associated with their Clebsch-Gordon coefficients. This can be explained by considering the simple case of a transition from the ground state $|J_g = 1/2\rangle$ to the excited state $|J_e = 3/2\rangle$. The magnetic sublevels and the squares of their Clebsch-Gordon coefficients are shown in figure 2.3. For an atom initially at position $z = \lambda/8$ the polarization is purely σ^-. As described in figure 2.3, the allowed transitions are $|J_g, m = -1/2\rangle \rightarrow |J_e, m = -3/2\rangle$ and $|J_g, m = 1/2\rangle \rightarrow |J_e, m = -1/2\rangle$ and the squared Clebsch-Gordon coefficient of the former is three times greater than that of the latter one. This corresponds to three times greater light shift of the former transition compared to the latter. This situation is opposite at the position $z = 3\lambda/8$ where the polarization is purely σ^+. In consequence, spatial variation of polarization leads to spatial variation of the light shift of the $|J_g, m = -1/2\rangle$ and $|J_g, m = +1/2\rangle$ sublevels.

For the case considered above the variations of the light shift of the sublevels are sinusoidal and the maximum potential of one sublevel coincides with the minimum of the other sublevel as shown in the figure 2.4. The spatial variation of the light shifts are mathematically given by

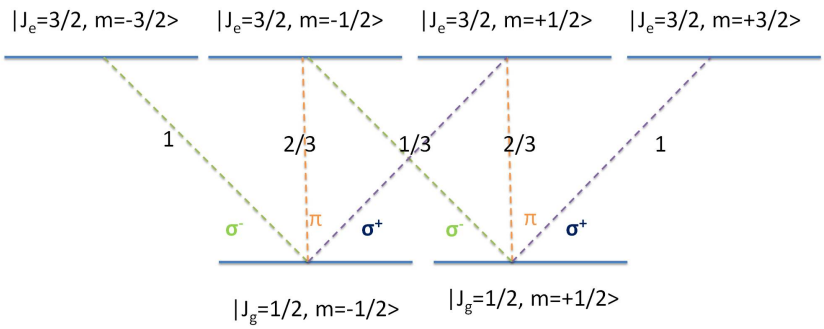

Figure 2.3: Squares of Clebsch-Gordon coefficients for the transition from the ground state $|J_g = 1/2\rangle$ to the excited state $|J_e = 3/2\rangle$.

$$U_{\pm}(z) = \frac{U_0}{2}\left(-2 \pm cos(2kz)\right), U_0 = -\frac{\hbar\Delta}{3}\frac{\Omega^2}{\Delta^2 + \frac{\Gamma^2}{4}}, \tag{2.13}$$

where k is the wavevector of the laser beam, U_0 is the maximum light shift, Ω is the Rabi frequency and Δ is the detuning of the laser beam from resonance.

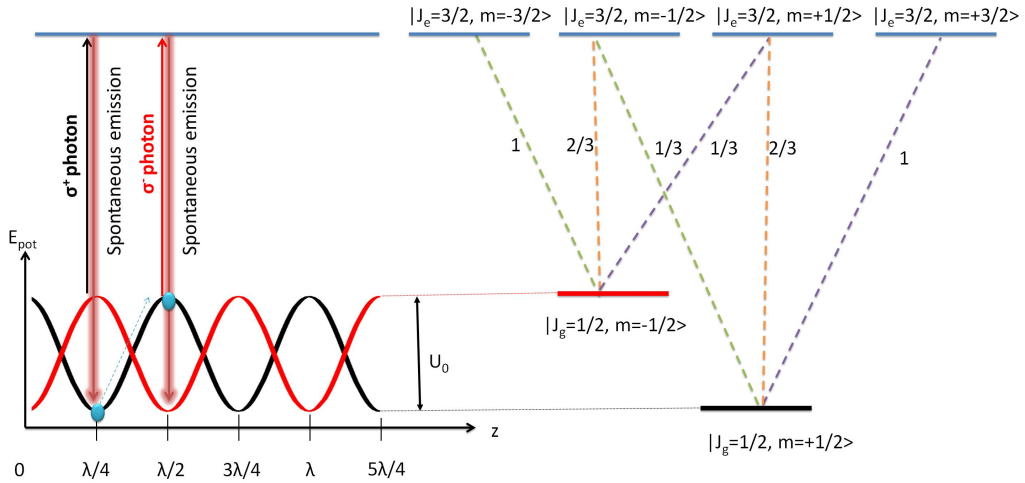

Figure 2.4: The polarization gradient of a standing wave and the resulting periodic potential

The figure 2.4 describes how the combination of optical pumping processes and the modulated light shifts of the ground state sublevels cools the atoms. An atom moving through this periodic potential starts to interchange its en-

ergy between kinetic and potential energy. If it stays in the same sublevel its total energy remains constant. However, because of the optical pumping a portion of kinetic energy is lost in every cycle. If the atom is considered to be initially at sublevel of $|J_g, m = 1/2\rangle$ and at position $z = \lambda/4$, then the dominant polarization is σ^+ and the atom is at the bottom of the potential well as shown in figure 2.4. At this position the ground state sublevel $|J_g, m = 1/2\rangle$ has lower potential energy than the $|J_g, m = -1/2\rangle$ sublevel. Therefore, as the atom moves along the z-axis it climbs the potential "hill" created by the light shift and its kinetic energy is converted into potential energy. When it reaches to top of the "hill" at $z = \lambda/2$, the polarization changes from σ^+ to σ^- and by absorbing σ^- photon the atom is excited to the state $|J_e, m = -1/2\rangle$. Two results are then possible; the atom decays back to the original sublevel to be reexcited or it can decay to the $|J_g, m = -1/2\rangle$ sublevel. In the latter case the atom falls to the bottom of the potential well by spontaneous emission so its potential energy becomes low and starts to climb again. Since the emitted photon has higher frequency than the absorbed photon, during this process the atom loses kinetic energy approximately equal to the amount of potential depth which leads to dissipation of energy. Therefore, as it climbs the top of the "hill" remaining kinetic energy is converted into potential energy. Through absorption-emission cycles the atom loses significant amount of kinetic energy. When the kinetic energy becomes less than the potential depth, it cannot climb anymore. In summary, as the atom moves through the polarization gradient its loses its kinetic energy due to optical pumping and starts to cool down until it is trapped in a potential well. This cooling mechanism is referred as *sub-Doppler cooling*. Because of the analogy between this sub-Doppler cooling process and the greek mith of Sysiphus, it is also called *"Sysiphus cooling"*.

As in the Doppler cooling there is a lowest temperature limit that can be reached in sub-Doppler cooling. This limit is deduced by considering the competition between cooling and heating of the atoms. This minimum temperature is called *recoil limit* T_r and given by the relation

$$k_B T_r = \frac{\hbar^2 k^2}{2m}, \tag{2.14}$$

where m is the mass of the atom.

$\sigma^+ - \sigma^-$ Configuration

In this configuration, atoms interact with two counterpropagating laser beam with σ^+ and σ^- polarizations. The polarization of the resultant total electric field is linear everywhere in space but rotates 360° about the direction of propagation with period of one wavelength of the laser beam as shown in figure 2.5. Contrary to the lin⊥lin configuration the resulting polarization leads to a spatially uniform light shift, thus Sisyphus cooling does not occur. Instead it causes velocity dependent forces resulting from a motion induced atomic orientation. In the rest frame of the atom, the electric field vector of the polarization rotates and acts as a quantization axis for the local polarization to precess around it. So for an atom in its rest frame the direction of polarization remains fixed. This can be explained by considering an atom with transition of $|J_g = 1\rangle \rightarrow |J_e = 2\rangle$ at rest. In this case atom experiences a fixed polarization direction so the $|J_g = 1, m = 0\rangle$ sublevel is shifted more than the $|J_g = 1, m = 1\rangle$ and the $|J_g = 1, m = -1\rangle$ sublevels because of the difference in their transition probabilities as the squares of the Clebsch-Gordon coefficients indicate in figure 2.6. Therefore, more atoms are optically pumped into the $|J_g = 1, m = 0\rangle$ sublevel. On the other hand, for an atom moving along the standing wave the direction of polarization rotates, hence the quantization axis. Because of this reason the optical pumping process to sublevels other than $|J_g = 1, m = 0\rangle$ sublevel starts in order to follow the rotating quantization axis. Since the optical pumping process lags the change in the direction of laser polarization, the population distribution among the sublevels lags the initial population distribution with all the atoms pumped in the $|J_g = 1, m = 0\rangle$ sublevel. This leads to an imbalance in population of the atoms among the sublevels and subsequently a difference in the scattering rates of each of the counterpropagating beams. Therefore, a net damping force opposing the direction of motion and cooling

the atoms arises. In consequence, the time lag between the atomic orientation and the precessing polarization direction causes an imbalance in population of sublevels resulting in a damping force that cools the atoms.

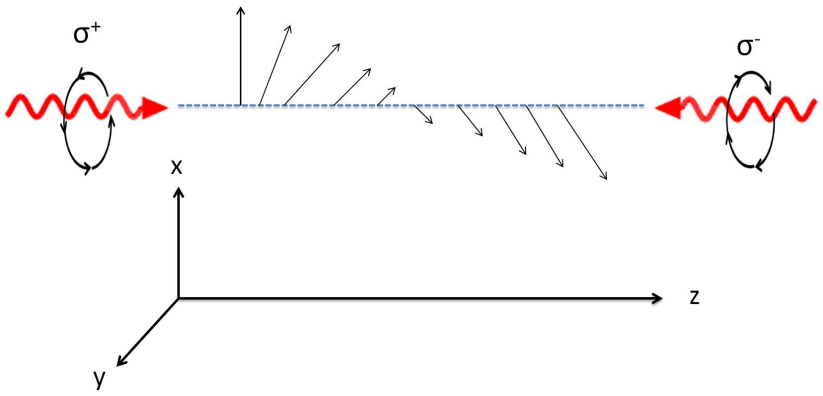

Figure 2.5: Two counterpropagating laser beams of σ^+ and σ^- polarization forms a standing wave with polarization linear everywhere but its direction rotates with period of λ.

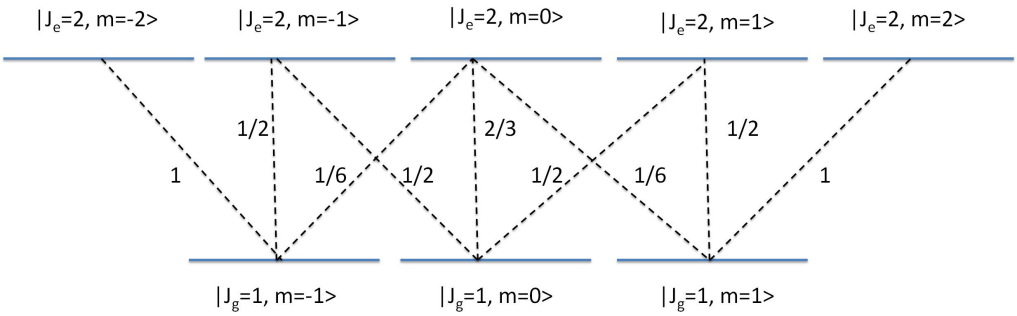

Figure 2.6: Squares of Clebsch-Gordon coefficients for the transition from ground state $|J_g = 1\rangle$ to excited state $|J_e = 2\rangle$.

2.4 The Magneto-Optical Trap

Although the optical molasses provides cooling of atoms to micro-Kelvin temperatures, the atoms will eventually diffuse out of the molasses region as the molasses force is only velocity dependent. In order to achieve both cooling and spatial confinement a position dependent force is required. The magneto-optical trap (MOT) is based on the combination of velocity and position dependent forces. The former force provides cooling and the latter provides spatial confinement. The cooling of atoms is obtained with laser beams via Doppler and sub-Doppler cooling. However, for spatial confinement the addition of quadrupole magnetic field is required. Indeed, the magneto-optical trap is realized by using three pairs of red-detuned circularly polarized counterpropagating beams and a quadrupole magnetic field as shown in figure 2.7. In fact the magnetic field does not confine the atoms by itself, but causes an imbalance in the radiation forces of laser beams with circular polarization. The quadrupole magnetic field is obtained by using a pair of coils with currents in opposite directions, which is the so-called anti-Helmholtz configuration. The center of the coils, which coincides with the intersection of the laser beams, has a zero magnetic field constituting the center of the magneto-optical trap.

The mechanism of the MOT can be explained by considering the one dimensional case for a two-level atom with a ground state angular momentum $|J_g = 0\rangle$ and an excited state $|J_e = 1\rangle$ with three Zeeman sub-levels. The application of the magnetic field removes the degeneracy in the excited state of the atom splitting it into three sub-levels as illustrated in figure 2.8.

The magnetic field produces a Zeeman shift in the excited state of the atom given by

$$\Delta E_{Zeeman} = g_J \mu_B m_J B, \tag{2.15}$$

where g_J is the Landé g-factor and μ_B is the Bohr magneton. The quadrupole magnetic field creates a linear magnetic field gradient in the trapping region producing a spatially dependent Zeeman shift in the energy of the

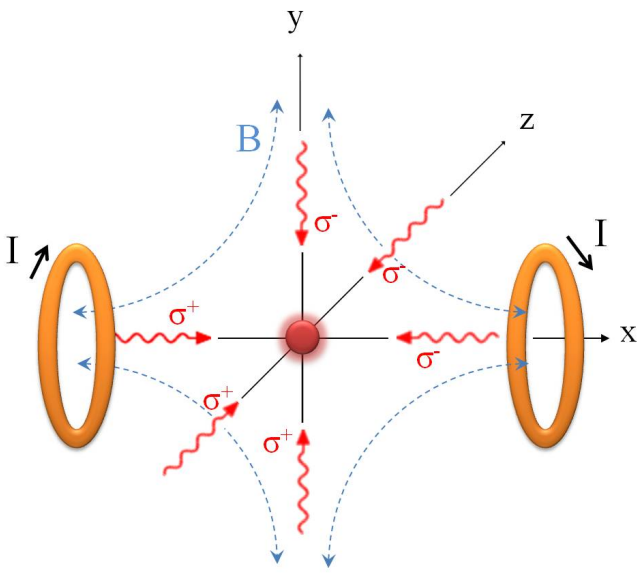

Figure 2.7: Working principle of the MOT. The anti-Helmholtz coil pair produces a magnetic field gradient leading to a spatially dependent force. The counterpropagating beams with σ^+ and σ^- polarizations are tuned to the cooling transition of the atoms.

$|J_e = 1, \Delta m_e = \pm 1\rangle$ states. When the two counterpropagating beams with circular polarisations σ^+ and σ^- and frequency ω red detuned from the atomic resonance are applied, the scattering force experienced by the atom is position dependent. The imbalance in radiation forces caused by the position dependent Zeeman shift can be explained by considering an atom moving away from the trap center. If the atom is at a position $z > 0$ the transition $\Delta m = -1$ is shifted down in energy. Therefore it is closer to resonance with the frequency of the σ^- laser beam. On the other hand, the energy is shifted up for $\Delta m = 1$ transition. Due to the selection rules and the Zeeman shift of the energy, $\Delta m = -1$ transition is excited by σ^- laser beam. Therefore an atom at $z > 0$ absorbs more photons from the σ^- laser beam than than the σ^+ laser beam leading to a scattering force that pushes the atom towards the trapping center. A similar process occurs for an atom located at $z < 0$, and absorbing more photons from the σ^+ laser beam. In consequence, the position dependent Zeeman effect causes an imbalance in

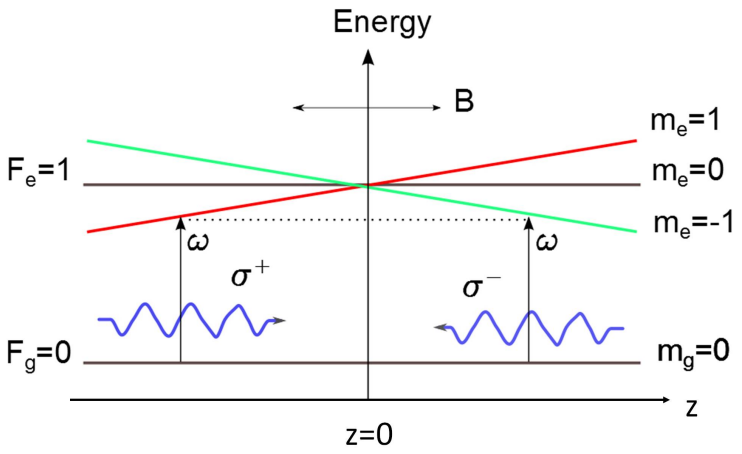

Figure 2.8: The working principle of the MOT is described for a simple two level atom in a linearly varying magnetic field, for an atomic transition $|J_g = 0\rangle$ to $|J_e = 1\rangle$. Two red detuned counterpropagating laser beams with σ^+ and σ^- polarizations illuminate the atoms. The magnetic field gradient causes Zeeman splitting of the magnetic sublevels depending on the position of the atoms. Selection rules and different Zeeman shift of the sublevels leads to an imbalance in the scattering force that pushes the atoms back to the center of the trap region.

the scattering forces. This leads to a restoring force, which pushes the atoms towards the trap center. Consequently, the magneto-optical trap provides cooling via the Doppler effect and confinement via the position dependent Zeeman effect.

The position dependent frequency shift caused by the Zeeman effect can be incorporated into the detuning of the scattering force in equation 2.6. Hence the effective detuning of the MOT becomes

$$\Delta_{eff} = \Delta \pm kv \pm \beta z, \tag{2.16}$$

where $\beta z = \frac{g\mu_B}{\hbar}\frac{dB}{dz}z$ is the Zeeman shift at position z and $\frac{dB}{dz}$ is the magnetic field gradient. Then the restoring force applied by the MOT is obtained as [28]

$$F_{MOT} = F_{scatt}^{sigma^+}(\Delta - kv - \beta z) - F_{scatt}^{sigma^-}(\Delta + kv + \beta z) \tag{2.17}$$

$$\cong -\frac{\partial F}{\partial \omega}(kv + \beta z) \tag{2.18}$$

$$= -\alpha v - \frac{\alpha\beta}{k} z, \tag{2.19}$$

where α is the damping coefficient given in equation 2.11 and $\frac{\alpha\beta}{k}$ is the spring constant. The atoms under the effect of this force undergo over-damped simple harmonic motion. Therefore, the atoms in the trap region are slowed by Doppler cooling and pushed towards the trap center by the position dependent force 2.19. This scheme can be easily extended to three dimensions by using three circularly-polarized orthogonal counterpropagating beams to obtain a magneto-optical trap [10]. The magneto optical trap can trap atoms from a room temperature vapour, therefore it is the starting point of all experiments with cold atoms.

A real atom has a multi-level structure rather than the two-level structure described above. For caesium the cooling transition is from the $6S_{1/2}(F_g = 4)$ ground state to the $6P_{3/2}(F_e = 5)$ excited state. In case an excited atom decays to another ground state $6S_{1/2}(F_g = 3)$ that is not coupled to the cooling laser beam, this results in a leakage in the cooling cycle and the cooling terminates. In order to counteract such effect, another laser that is tuned from the $6S_{1/2}(F_g = 3)$ to the $6P_{3/2}(F_g = 4)$ state is required to recycle the atoms for cooling. This additional laser beam is called "repumper" laser.

2.5 The Dipole Trap

There are many ways for manipulating and confining atoms utilizing electric and magnetic fields. The magneto-optical trap uses the radiation force of photons resonant with the atomic transition and magnetic field gradients. The dipole trap is based on the electric dipole interaction with light. The dipole force arises from the interaction of the induced atomic dipole moment with the driving inhomogenous electric field. The dipole force was first theoretically investigated by Askaryan in 1962 [11] and experimentally demonstrated by Bjorkholm in 1978 [12]. Later in 1986 Chu was the first to experimentally demonstrate the use of dipole force for trapping of neutral atoms [13]. Dipole traps typically have trap depths in the mK range [15] and allow storage times of few minutes [29]. However, atoms have to be precooled by appropriate methods in order to be efficiently transferred into a dipole trap because of their shallower trap depth compared to other traps based on scattering force. As the dipole trap is conservative, it does not have the ability to cool the atoms. In most of the cases, the atoms are preecooled in a MOT, which is able to capture them from room temperature vapour and cool them down to the μK regime. Despite the precooling process the fraction of atoms transferred to the dipole trap is limited because of the high scattering rates and subsequent heating due to recoil of the atoms. But in far-off resonance optical dipole traps (FORT), a large detuning from atomic resonance is used,that leads to low scattering rates and subsequently negligible recoil heating [30].

In this section, the physics behind the dipole trap is described. Firstly, the interaction between atom and the light field is discussed by considering the classical point of view. This is followed by a discussion of multi-level atoms in a quantum mechanical picture. Finally, dipole trapping with Gaussian beams is described.

2.5.1 Classical Point of View

From a classical point of view, the dipole force can be understood in terms of electric polarizability of an atom. In free space, an atom in its ground state does not have an electric dipole moment. When it is placed in an electric field, its charge distribution is distorted and the atom becomes polarized. A dipole moment oscillating at the driving frequency of electric field is introduced. The amplitude of the dipole moment is simply related to the amplitude of the electric field as

$$p = \alpha E, \tag{2.20}$$

where the proportionality factor $\alpha = \alpha(\omega)$ is the polarizability, which is complex valued and frequency dependent. In the Lorentz model, the atom is treated as a harmonically bound electron, with charge e and mass m_e, interacting with a classical radiation field and oscillating at frequency ω_0 corresponding to the atomic transition frequency. The equation of motion of the electron is given by

$$\ddot{x}(t) + \Gamma_\omega \dot{x}(t) + \omega_0^2 x(t) = \frac{e}{m_e} E(t). \tag{2.21}$$

The charge distribution of the atom is equivalent to the distribution of the dipole moment as the expression $\mathbf{p} = e \cdot \mathbf{d}$ indicates, where $\mathbf{d}$ is the displacement between the nucleus and center of the electron cloud. Therefore the induced dipole moment obeys the same differential equation than that of the electron. Then the equation for the dipole moment can be written as

$$\ddot{p}(t) + \Gamma_\omega \dot{p}(t) + \omega_0^2 p(t) = \frac{e}{m_e} E(t), \tag{2.22}$$

where Γ_ω is the damping rate, which describes the energy loss of the dipole. By integrating this equation the induced dipole moment is obtained as

$$p(t) = \frac{e^2 E(t)}{m_e} \left(\frac{1}{\omega_0^2 - \omega^2 - i\omega\Gamma_\omega} \right). \tag{2.23}$$

Then the polarizability α and the damping rate Γ_ω are extracted as

$$\alpha = \frac{e^2}{m_e}\left(\frac{1}{\omega_0^2 - \omega^2 - i\omega\Gamma_\omega}\right), \tag{2.24}$$

$$\Gamma_\omega = \frac{e^2\omega^2}{6\pi\epsilon_0 m_e c^3}. \tag{2.25}$$

By introducing the on-resonance damping rate $\Gamma \equiv \Gamma_{\omega_0} = (\omega_0/\omega)^2\Gamma_\omega$ the expression for the polarizability becomes

$$\alpha = 6\pi\epsilon_0 c^3 \frac{\Gamma/\omega_0^2}{\omega_0^2 - \omega^2 - i(\omega^3/\omega_0^2)\Gamma}. \tag{2.26}$$

The interaction energy of the dipole moment with the driving field is given by

$$W = -\mathbf{p}\cdot\mathbf{E} = -\alpha|E|^2\cos\theta. \tag{2.27}$$

where θ is the angle between the dipole moment and the electric field. The driving electric field oscillates at frequencies that are too fast for the atom to follow. Therefore it only senses the time average of the interaction energy, which cancels the rapidly oscillating terms. Then the interaction potential between the induced dipole moment and the electric field is given by

$$U_{dip} = -\frac{1}{2} < \mathbf{p}\cdot\mathbf{E} > = -\frac{1}{2\epsilon_0 c} Re(\alpha) I, \tag{2.28}$$

where ϵ_0 is the electric permittivity of free space and $I = \frac{1}{2}\epsilon_0 c|E|^2$ is the intensity of the laser beam. The gradient of the dipole potential gives a conservative dipole force given by

$$\mathbf{F}_{dip}(\mathbf{r}) = -\nabla U_{dip}(\mathbf{r}) = \frac{1}{2\epsilon_0 c} Re(\alpha)\nabla I. \tag{2.29}$$

Thus the interaction dipole potential and the dipole force depend on the intensity of the laser beam and on the real part of the polarizability $Re(\alpha)$, which is dispersive. The real part of the polarizability changes sign around resonance leading to two regimes for the dipole force. When the frequency of

the driving field is smaller than the atomic resonance frequency ($\Delta < 0$), the induced dipole oscillates in phase with the driving field. Thus the atom is pulled towards regions of higher intensity. On the other hand, if the frequency of the driving field is bigger than the atomic resonance frequency ($\Delta > 0$), the induced dipole is in phase opposition to the driving field. In this case, the atom is repelled from regions of high intensity. The imaginary part of the polarizability, which describes the out-of-phase component of the oscillation leads to absorption of driving energy and then re-emission as dipole radiation from the atom. The power absorbed from the electric field is given by

$$P_{abs} =< \dot{\mathbf{p}} \cdot \mathbf{E} >= Im(\alpha)\frac{I}{\epsilon_0 c}\omega. \tag{2.30}$$

The cycles of absorption and subsequent re-emission processes lead to the scattering rate

$$\Gamma_{sc}(\mathbf{r}) = \frac{P_{abs}}{\hbar\omega} = \frac{1}{\hbar\epsilon_0 c} Im(\alpha) I(\mathbf{r}). \tag{2.31}$$

In consequence, the dipole interaction potential is a function of the real (dispersive) part of the polarizability $Re(\alpha)$, whereas the scattering rate is function of its imaginary (absorptive) part $Im(\alpha)$.

In case of a far-off resonant trap (FORT), the far-detuned frequency and the negligible saturation result in a very low scattering rate ($\Gamma_{sc} \ll \Gamma$). The polarizability is thus approximated by the polarizability of the classical harmonic oscillator subject to the classical radiation field. Then, in this regime the dipole potential and the scattering rate are obtained as

$$U_{dip}(\mathbf{r}) = -\frac{3\pi c^2}{2\omega_0^3}\left(\frac{\Gamma}{\omega_0 - \omega} + \frac{\Gamma}{\omega_0 + \omega}\right) I(\mathbf{r}), \tag{2.32}$$

$$\Gamma_{sc}(\mathbf{r}) = \frac{3\pi c^2}{2\hbar\omega_0^3}\left(\frac{\Gamma}{\omega_0 - \omega} + \frac{\Gamma}{\omega_0 + \omega}\right)^2 I(\mathbf{r}), \tag{2.33}$$

where ω and ω_0 are the laser frequency and the resonance frequency of the classical oscillator respectively. The expressions obtained for the dipole interaction potential and scattering rate can be simplified by using the rotating-

wave approximation. When the laser field is tuned far below resonance such that $\omega/\omega_0 \approx 1$, then the term with denominator $\omega + \omega_0$ inside the brackets can be neglected, which is the rotating-wave approximation. Then the expressions for the dipole interaction energy and the scattering rate become

$$U_{dip}(\mathbf{r}) = -\frac{3\pi c^2}{2\omega_0^3}\frac{\Gamma}{\Delta}I(\mathbf{r}), \tag{2.34}$$

$$\Gamma_{sc}(\mathbf{r}) = \frac{3\pi c^2}{2\hbar\omega_0^3}\left(\frac{\Gamma}{\Delta}\right)^2 I(\mathbf{r}). \tag{2.35}$$

These expressions show that the dipole potential scales as $1/\Delta$, while the scattering rate scales as $(1/\Delta)^2$. The relation between scattering rate and the dipole potential is given by

$$\hbar\Gamma_{sc} = \frac{\Gamma}{\Delta}U_{dip}. \tag{2.36}$$

Thus for a given dipole potential the scattering rate can be reduced by increasing both the intensity and the detuning of the laser beam.

At high intensities ($I >> I_{sat}$), the coupling strength of the atom to the electric field is large compared to the damping rate Γ of the atom. In this case, the atom cannot be treated separately from the light field. Instead it is considered as a two-level quantum system interacting with the field. Then the damping rate Γ is determined by the dipole matrix element between ground state $|g\rangle$ and excited state $|e\rangle$, which is given by [15]

$$\Gamma = \frac{\omega_0^3}{3\pi\epsilon_0\hbar c^3}|\langle e|\hat{\mu}|g\rangle|^2 \tag{2.37}$$

where $\hat{\mu} = -e\mathbf{r}$ is the dipole operator. For D lines of alkali atoms, the classical result of the damping rate given in equation 2.25 approximates well to the true spontaneous decay rate of the excited state to within a few percent.

2.5.2 Multi-level Atom

In the preceding subsection, a two-level atom with a single ground and a single excited state was considered. However, a real atom has multi-levels and the light field couples to several levels simultaneously. Although the two-level atom model is sufficient to describe the physics behind the dipole trap, it is not suitable for precise calculations of the trap depth for Caesium as it does not include all the physical effects. Caesium atoms have complex substructure including fine and hyperfine interactions. The former one arises due to spin-orbit interaction and the latter one arises due to coupling of nuclear spin I to the total angular momentum J causing a splitting in energy levels of the atom. As a consequence, this leads to a state dependent dipole potential. Therefore, a more realistic approach can be followed by taking into account several levels of the atom. For a multi-level atom, the total dipole potential or total light shift for a state $|i\rangle$ is obtained by summing all possible contributions from couplings to other states $|j\rangle$, as mathematically expressed by

$$U_{dip}(r) = \frac{3\pi c^2 \Gamma}{2} I \sum_j \frac{|C_{ij}|^2}{\omega_{ij}^3 \Delta_{ij}}, \tag{2.38}$$

where Δ_{ij} is the detuning of the laser field from the corresponding $|i\rangle \rightarrow |j\rangle$ transition and C_{ij} is the Clebsch-Gordon coefficient, whose amplitude $|C_{ij}|^2$ is proportional to the transition strength between a state $|i\rangle$ and a state $|j\rangle$. However, for practical calculations the expression 2.38 is hard to apply due to the large number of levels to be considered. A simplified expression can be obtained for large laser detuning exceeding the hyperfine splitting of the atom. We consider the specific case of alkali atoms. These atoms have hyperfine structure with ground state $S_{1/2}$ and splitted excited states $P_{1/2}$ (D1 line) and $P_{3/2}$ (D2 line). For these elements, the hyperfine states remain unresolved for laser detunings larger than the hyperfine splitting. Then based on the equation 2.38, a general expression for the total dipole potential for the ground state m_F sublevel is given by [15]

$$U_{dip}(r) = \frac{\pi c^2 \Gamma}{2} I \left(\frac{2 + q g_F m_F}{\omega_{3/2}^3 \Delta_{3/2}} + \frac{1 - q g_F m_F}{\omega_{1/2}^3 \Delta_{1/2}} \right), \tag{2.39}$$

where g_F is the Lande g-factor, the detunings $\Delta_{1/2}$ and $\Delta_{3/2}$ are the detunings from the transitions from the D1 and D2 lines respectively, and q is term characterizing the polarization of the laser beam: for linear polarization (π) of the dipole trap beam $q = 0$ and for circular polarizations ($\sigma^{\pm}$) $q = \pm 1$. A circular polarisation of the trap beam causes the dipole trap potential to be magnetic sublevel dependent [31], since the shift of the magnetic sublevels is equivalent to a fictitous magnetic field [32, 33]. However for linear polarization (π) the dipole trap potential is independent of magnetic sublevels because they are shifted by the same amount. Thus the dipole potential for a linearly polarized laser beam simplifies to

$$U_{dip}(r) = \frac{\pi c^2 \Gamma}{2} I \left(\frac{2}{\omega_{3/2}^3 \Delta_{3/2}} + \frac{1}{\omega_{1/2}^3 \Delta_{1/2}} \right). \tag{2.40}$$

In case of low intensity of light field, the shifts in energy levels of the atom can be calculated by using time-independent perturbation theory. Then the AC Stark shift of a multi-level atom is given by

$$\Delta E_i = \sum_i \frac{|\langle J_j F_j m_j | \hat{\mu} \cdot \mathbf{E} | J_i F_i m_i \rangle|^2}{4\hbar \Delta_{eff}}, \tag{2.41}$$

where m is magnetic quantum number, F is total angular momentum, J is total electronic angular momentum $|J_i F_i m_i\rangle$,$|J_j F_j m_j\rangle$ are the initial and final states of the corresponding transition. The effective detuning is given by

$$\frac{1}{\Delta_{eff}} = \frac{1}{\omega_0 - \omega} + \frac{1}{\omega_0 + \omega}. \tag{2.42}$$

In order to calculate the energy shift the dipole matrix elements in the equation must be reduced. When the m dependence is removed, the dipole matrix becomes

$$|\langle J_j F_j|\hat{\mu}\cdot\mathbf{E}|J_i F_i\rangle|^2 = |\mathbf{E}|^2(2F_j+1)\begin{pmatrix} F_i & 1 & F_j \\ m_i & q & -m_j \end{pmatrix}^2 |\langle J_j F_j||\hat{\mu}||J_i F_i\rangle|^2, \quad (2.43)$$

where I is nuclear spin and$q$ is the polarisation of the dipole trap beam ($q = 0$ for linear polarization and $q = \pm 1$ for circular polarization). Then it is further simplified to factor out the F_j and F_i dependence by using the following relations:

$$\langle J_j F_j||\hat{\mu}||J_i F_i\rangle = (J_j||\hat{\mu}||J_i)(-1)^{F_i+J_j+I_j+1}\sqrt{(2F_i+1)(2J_j+1)}\begin{Bmatrix} J_j & J_i & 1 \\ F_i & F_j & I \end{Bmatrix}, \quad (2.44)$$

$$(J_j||\hat{\mu}||J_i)^2 = (2J_j+1)\frac{3\pi\epsilon_0\hbar c^3}{\omega_0^3\tau}, \quad (2.45)$$

where τ is the lifetime from the higher state to a lower state.

Finally, by combining all these expressions the total AC stark shift experienced by the atom is obtained as

$$\Delta E = |\mathbf{E}|^2(2F_i+1)\sum_i \frac{3\pi\epsilon_0\hbar c^3}{4\Delta_0\omega_0^3\tau}(2F_j+1)(2J_j+1)\begin{pmatrix} F_j & 1 & F_i \\ m_i & q & -m_j \end{pmatrix}^2 \begin{Bmatrix} J_i & J_j & 1 \\ F_j & F_i & I \end{Bmatrix}^2. \quad (2.46)$$

By using this formula, the AC Stark shift of the excited and ground states of the caesium atom can be computed by using mathematica software. The AC stark shifts of the ground state $6S_{1/2}$ and the excited state $6P_{3/2}$ as function of dipole trap laser wavelength is plotted in figure 2.9 for linearly polarized laser beam with intensity of 3×10^9 W/m^2 by including contributions from the states up to 15S, 11P and 11D (data taken from [34–36]). In this graph, the light shift of the ground state $6S_{1/2}$ is plotted with red dashed line and $F_e = 4$ level of the excited state $6P_{3/2}$ are plotted in other colours for all sublevels.

In general, for red-detuned far-optical dipole trap the AC Stark shift experienced by an atom in the ground state is negative while it is positive for the excited state. This causes a broadening in the transition frequency between the ground and the excited states. It follows that the application of free-space laser cooling mechanisms is no longer effective. Furthermore, as the ground and the excited states experience different AC stark shifts the trapped atoms experience different dipole potentials in the ground and excited states. Because of this reason, the dipole force on the trapped atoms fluctuates leading to heating.

It is possible to address these problems by performing state-insensitive trapping. In 1999 Katori *et* al. suggested controlling the light shifts of the ground and the excited states by tuning the wavelength of the trap laser. In this way, at a certain wavelength the light shifts of the excited and the ground state become equal so the transition frequency of the trapped atom is equal to that of the atom in free space. The wavelength at which the differential light shift of the ground and excited state is zero is referred as "magic wavelength" [23]. Therefore, at the magic wavelength the dipole trap becomes state-insensitive. It follows that the trapped atoms can be optically addressed as if they were in free space. Furthermore, laser cooling mechanisms such as Doppler cooling can be performed during loading the atoms from the MOT to the dipole trap.

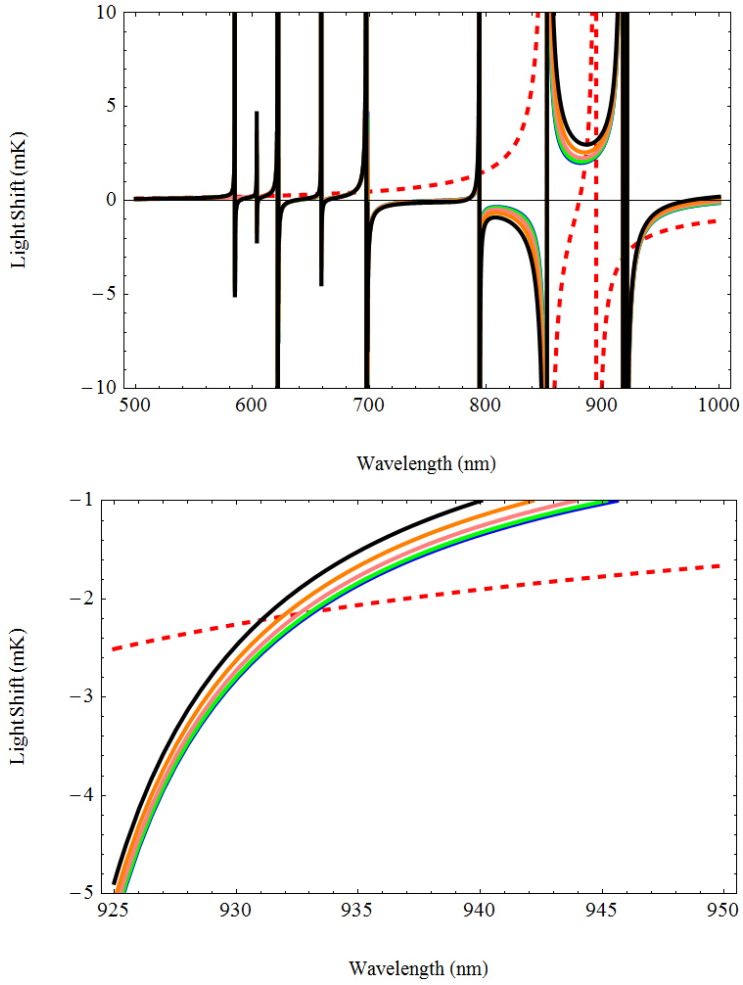

Figure 2.9: Calculation of the AC-Stark shift of the excited and ground states of the caesium atom as functions of the laser wavelength for a laser intensity of 3×10^9 W/m^2 and linear polarization. The light shift for the ground state $6S_{1/2}$ is plotted in red dashed line. The light shift for the $F_e = 4$ level of the excited state $6P_{3/2}$ is plotted in blue, green, pink, orange and black lines for the the sublevels $m = 0, \pm1, \pm2, \pm3, \pm4$ respectively. For the ground state all the sublevels are degenerate while they are split for the $F_e = 4$ level of the excited state.

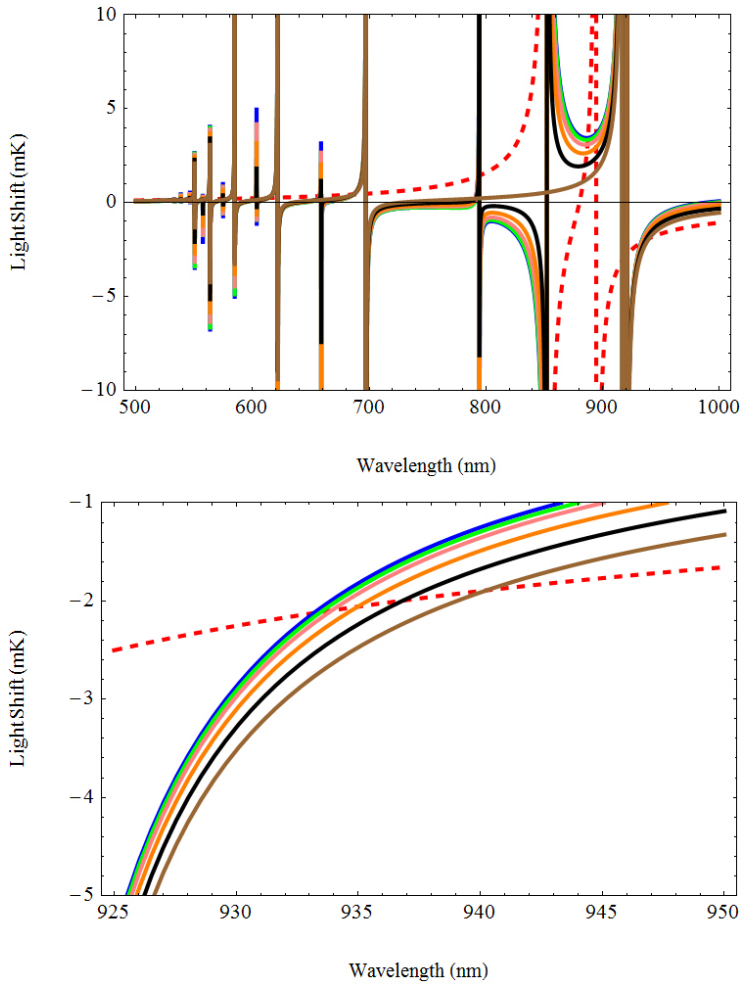

Figure 2.10: Calculation of the AC-Stark shift of the excited and ground states of the caesium atom as functions of the laser wavelength for a laser intensity of 3×10^9 W/m^2 and linear polarization. The light shift for the ground state $6S_{1/2}$ is plotted in red dashed line. The light shift for the $F_e = 5$ level of the excited state $6P_{3/2}$ is plotted in blue, green, pink, orange, black and brown lines for the the sublevels $m = 0, \pm1, \pm2, \pm3, \pm4, \pm5$ respectively. For the ground state all the sublevels are degenerate while they are split for the $F_e = 5$ level of the excited state.

2.5.3 Gaussian Beam Dipole Traps

Position dependent intensity distributions lead to a dipole potential and a force. In case of red detuning ($\Delta < 0$), the dipole potential is attractive towards the maximum of the intensity, therefore a single focused laser beam is sufficient to trap atoms. This was first suggested by Ashkin in 1978 [37] and realized by Chu et al. in 1986 [13]. In this section, a description of a Gaussian beam and the parameters of the resulting dipole trap is given. Dipole traps are assumed to be far-off resonant traps throughout the following subsections.

Focused Beam Dipole Trap

The simplest way to create a dipole trap is to use a single laser beam, which is red-detuned and tightly focused creating a maximum intensity region for atoms to be trapped. In the paraxial ray approximation, a focused laser beam is represented by a Gaussian beam with TEM_{00} mode. The spatial intensity distribution of a focused Gaussian beam with total power P propagating along the z-axis is given by

$$I(r,z) = I_0 \left(\frac{\omega_0}{\omega(z)}\right)^2 exp\left(\frac{-2r^2}{\omega^2(z)}\right), \tag{2.47}$$

where $r^2 = x^2 + y^2$ is the radial distance from the position of maximum intensity and $I_0 = 2P/\pi\omega^2(z)$ is the maximum intensity of the beam. The Gaussian laser beam is characterized by the beam waist which specifies the $1/e^2$ radius of the beam. Its dependence on the axial distance z is given by

$$\omega(z) = \omega_0\sqrt{1 + \left(\frac{z}{z_R}\right)^2}, \tag{2.48}$$

where ω_0 is the beam waist defining the minimum radius of the focused beam and z_R is the Rayleigh length denoting the distance from the focus of the beam to the point where the radius increases to $\sqrt{2}\omega_0$. These characteristic parameters of the focused Gaussian beam are illustrated in the figure 2.11

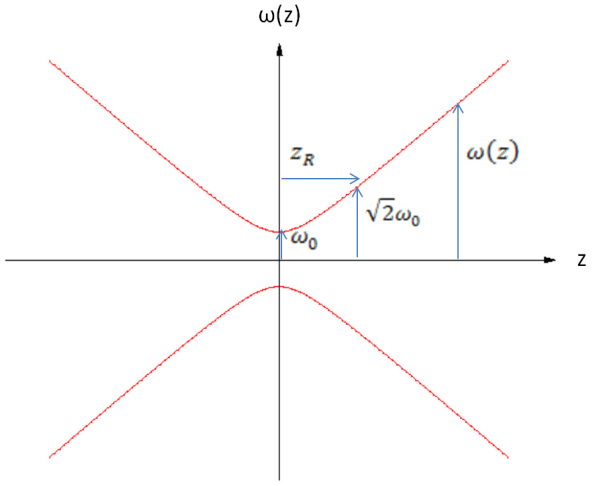

Figure 2.11: Focused Gaussian beam and its intensity distribution.

As the dipole potential is proportional to the intensity of the laser beam, they have same spatial dependence. By placing the $I(r, z)$ into the equation 2.34, the dipole potential can be obtained as

$$U_{dip} = \frac{3\pi c^2}{2\omega_{0^2}} \frac{\Gamma}{\Delta} I_0 \left(\frac{\omega_0}{\omega(z)} \right)^2 exp \left(\frac{-2r^2}{\omega^2(z)} \right). \tag{2.49}$$

The depth of the dipole trap created is defined as the optical potential at the position of maximum intensity $U_0 = |U(r = 0, z = 0)|$. The atoms are trapped in the dipole trap whenever their thermal energy $k_B T$ is smaller than the optical potential U_0. The trapping region is specified by the geometric properties of the laser beam. In case of fixed wavelength, the geometric characteristics of the Gaussian beam are entirely determined by the beam waist ω_0. The Rayleigh length is given by

$$z_R = \frac{\pi \omega_0^2}{\lambda}. \tag{2.50}$$

The atoms are trapped around the center of the laser beam at the maximum intensity position. Thus the ratios r/ω_0 and z/z_R are smaller than one. In this case, the dipole potential in equation 2.49 can be expanded in series to

the first orders of r/ω_0 and z/z_R. As a result, it can be approximated as a simple cylindrical harmonic oscillator which is given by

$$U_{dip}(r,z) = U_0 cos(kz)\left(1 - 2\left(\frac{r}{\omega_0}\right)^2 - \left(\frac{z}{z_R}\right)^2\right). \tag{2.51}$$

The three dimensional visualization of this potential is shown in figure 2.12. By solving this equation the oscillation frequencies of a trapped atom in the radial and the axial direction are obtained respectively as

$$\omega_r = \sqrt{\frac{4U_{dip}}{m\omega_0^2}}, \tag{2.52}$$

$$\omega_z = \sqrt{\frac{24U_{dip}}{mz_R^2}}. \tag{2.53}$$

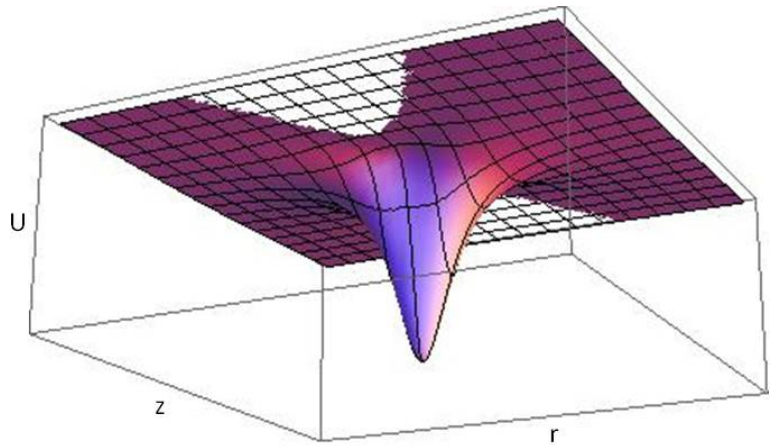

Figure 2.12: 3D Visualization of focused beam dipole potential at 935.6 nm for 200 mW power with beam waist of 5μm.

1D Lattice Dipole Trap

A one dimensional lattice trap is a trap determined by a standing wave, created by either retro-reflecting a single laser beam or adding two identical counterpropagating laser beams. Interference of the laser beams forms the

standing wave, resulting in a periodic potential. The spatial intensity distribution of a Gaussian laser beam in one dimensional lattice configuration is given by

$$I(r,z) = I_0 cos^2(kz) \left(\frac{\omega_0}{\omega(z)}\right)^2 exp\left(\frac{-2r^2}{w^2(z)}\right), \tag{2.54}$$

where the maximum intensity I_0 of a Gaussian standing wave can be expressed by using the total power of the two beams P and their beam waist ω_0,

$$I_0 = \frac{4P}{\pi\omega_0^2}. \tag{2.55}$$

Because of the interference between the beams, the maximum intensity of the standing wave is four times higher than that of the single beam. This is also reflected in the magnitude of the dipole potential, which is given by

$$U_{dip}(r,z) = 4U_0 cos^2(kz) \left(1 - 2\left(\frac{r}{\omega_0}\right)^2 - \left(\frac{z}{z_R}\right)^2\right). \tag{2.56}$$

By approximating the equation 2.56 as harmonic potential, the axial and radial trapping frequencies are obtained as

$$\omega_r = \frac{2\pi}{\lambda}\sqrt{\frac{2U_{dip}}{m}}, \tag{2.57}$$

$$\omega_z = \frac{2}{\omega_0}\sqrt{\frac{U_{dip}}{m}}. \tag{2.58}$$

The 3D visualization of the 1D lattice dipole trap along the radial and axial position are shown in figure 2.13.

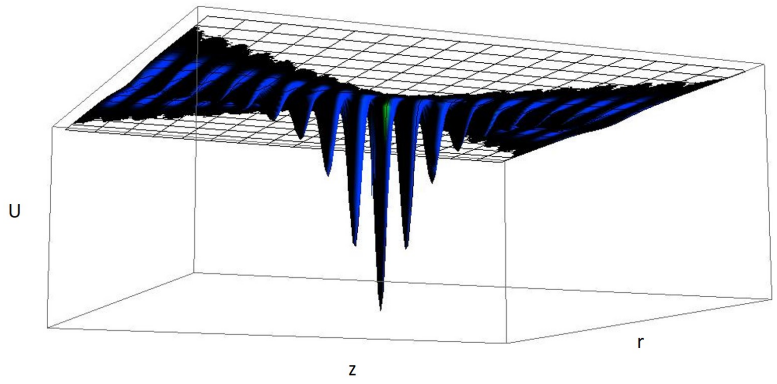

Figure 2.13: 3D Visualization of 1D lattice dipole trap at 935.6 nm for 200 mW power with beam waist of 5μm.

Chapter 3

Experimental Setup

This chapter describes the components in our experimental setup. These includes the vacuum system, the light sources and the imaging system.

3.1 Vacuum System

In laser cooling and trapping experiments, the reduction of the background gas pressure is of great importance. High background pressure causes a decrease in the confinement time due to the collisions between trapped and background thermal atoms. Therefore, to achieve long confinement time a low background pressure is essential, which can be obtained with ultra-high vacuum (UHV) systems (typically less than 10^{-9} mbar). On the other hand, the MOT can capture atoms from the low velocity tail of a room temperature atomic vapour. Thus, a high background pressure is required to be able to capture a significant amount of atoms even though the atoms which are not captured cause collisions. It follows that a single MOT is not suitable to both capture a significant number of atoms and obtain long confinement times. It is possible to address these problems present in the single MOT configuration by using a differentially pumped double MOT system [38]. In this system, the collection and holding functions of a MOT are separated into two different vacuum chambers: the atomic source chamber and the science chamber. In the former chamber the vapour pressure is higher, hence the

loading rate is high. On the other hand, the background pressure is lower in the science chamber allowing a longer confinement time. The differential pumping between the two chambers is maintained by two separate vacuum pumps. These two chambers are connected to each other through a hole, which is used to maintain the transfer of the atoms cooled in the first MOT to the second MOT. The low velocity cold atomic beam formed in this way is the so called low-velocity intense source (LVIS) [39], which is described in the next subsection.

A schematic of our vacuum system consisting of the atomic source and the science chamber is shown in figure 3.1. The upper chamber is the LVIS atomic source chamber where the first MOT is loaded from the atomic vapour. To achieve an ultra-high vacuum pressure (UHV), an ion pump (20 l/s) is connected to the chamber. A pressure below 10^{-8} mbar can be reached. Then the cold atom beam extracted from the LVIS is transferred to the science chamber through a a blank flange with a hole of 1.5 mm diameter and 20 mm length, which serves as a differential pumping tube between the higher pressure region of the LVIS and the lower pressure region of the science chamber. The lower part of the chamber, which is the so called science chamber, is connected both to an ion pump (55 l/s) and a NEG getter pump to provide lower pressure (below 10^{-12} mbar) compared to the atomic source chamber. The science MOT is formed inside the glass cell attached to the metal flange. The glass cell is made of quartz glass and has dimensions of 30×175 mm with thickness of 5 mm. The advantage of using a glass cell is the free optical access it provides.

3.1.1 LVIS

Many cold atom sources have been demonstrated in UHV systems so far. These includes cold atomic beams provided by Zeeman slowers [40, 41], by chirped cooling [42], by broadband light [43] and by isotropic laser light cooling [44]. Their disadvantage is their transverse diffusion and high number of thermal background atoms. In addition, there are sources using precooled atoms such as the 2D MOT [45] and the low-velocity intense source (LVIS)

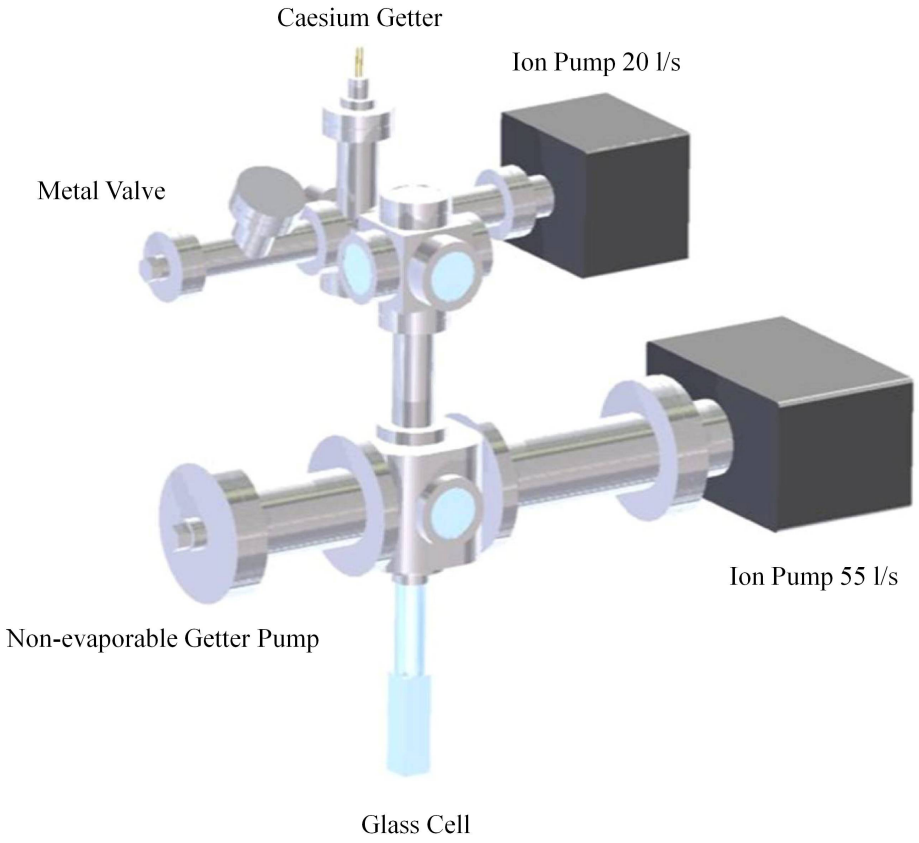

Figure 3.1: Vacuum System

[39]. Among these sources, LVIS has the advantage of simplicity. Therefore, in our setup LVIS is used as source of cold atoms.

The LVIS relies on atoms emitted from a MOT via an imbalance in the radiation pressure forces. In this way, atoms are extracted efficiently from one arm of a standard MOT configuration. So the LVIS MOT is very similar to a standard MOT with three orthogonal circularly polarized counterpropagating laser beams intersecting at the center of a quadrupole magnetic field apart from the dark region in one of the intersecting beams. This dark region in one beam causing the radiation imbalance is created by a hole in one of the retro reflecting mirrors and the corresponding wave plate. Hence the atoms reaching the trap center are accelerated out of the trap due to the imbalance in the radiation pressure along that axis. Consequently, a continuous beam

of cold atoms produced in the LVIS MOT is extracted via the hole and then loaded into the second MOT.

In the LVIS MOT atoms are captured from the background. Therefore the atoms from the low velocity tail of the room temperature velocity distribution are captured and cooled more efficiently compared to the more thermal atoms in the background. Thus the atoms having larger velocity do not spend enough time in the trap to be cooled sufficiently so they move away from the trap center. These atoms are filtered by the hole, hence the atoms extracted from the LVIS MOT are the ones captured from the low velocity tail of the room temperature velocity distribution and further cooled.

The LVIS MOT is optimized to provide a large atom flux to the second MOT. The flux is increased by aligning the position of the MOT to be at the center of the hole. As the LVIS is obtained from the imbalance in the radiation pressure forces the velocity of the LVIS atoms is determined by the number of photons scattered from the unbalanced part of the beam along the LVIS direction.

3.1.2 Getters

The atom source for the experiment is a caesium dispenser (SAES Getters, CS/NF/8/25 FT10 + 10, 5G00608), which is mounted on an electrical 8-pin feedthrough located at the top of the chamber. The release of the caesium atoms is activated via heating created by applying current through the dispenser. To obtain a constant release rate of caesium atoms, the current is applied by a DC power supply. In our setup 16 dispensers are mounted in total, thus when one of them runs out of caesium we can switch to another without having to open the vacuum chamber.

3.1.3 Magnetic Coils

Different sets of coils are used in our setup, for the MOT and for the compensation of the earth magnetic field. The first one is the quadrupole coil assembly used to provide the magnetic field gradient for magneto-optical

trapping. It consists of two coils in anti-Helmholtz configuration. The magnitude of the generated magnetic field gradient determines the strength of the confinement in the trap center. The coils for the first MOT have a diameter of 10 cm and are capable of producing a magnetic field gradient of 15 G/cm with a current of 3.5 A passing through them, while the coils for the second MOT have a diameter of 10 cm and are capable of producing a magnetic field gradient of 37 G/cm with a current of 4.7 A. In order to achieve fast switching of the magnetic field of the second MOT, a MOSFET (Metal Oxide Semiconductor Field-Effect Transistor) is connected in series between the coils and the power supply. The voltage at the gate input of the MOSFET is proportional to the current flowing through the coils. Its value is set by a computer and regulated by a PID controller. Due to high power dissipation in MOSFET circuit, it is mounted on a water cooled copper plate. The schematic of its circuit is given in appendix A.

External stray magnetic fields such as the Earth's magnetic field and other ambient magnetic fields due to ion pumps and power supplies may cause problems in the experiment carried out. Specifically, during the optical molasses phase residual magnetic fields cause a Zeeman shift leading to imbalance in the scattering force. Such an imbalance may change the zero magnetic field position of the MOT. Therefore, a compensation system consisting of three pairs of coils in the Helmholtz configuration are used to nullify the stray magnetic field in the trapping region. These coils are built in a square mechanical frame with side length of 40 cm and placed along all three spatial axes. Each of the coil pair is supplied by a different DC current supply and ≈ 0.5 amperes of current is sufficient to compensate the background magnetic field.

3.2 Laser System

The essential requirements for a laser system for cooling and trapping of atoms are output power, tunable frequency and narrow linewidth. For the MOT, this was achieved by using commercially available semiconductor diode lasers. However, for the dipole trap more power is required. Therefore, a laser power amplifier system based on a tapered amplifier chip was used. A semiconductor diode laser and a tapered amplifier were used in a master-slave configuration to obtain a master oscillator power amplifier (MOPA) system, which provides high power. This section starts with the description of the lasers, their frequency stabilization and the optical elements used for the MOT. Then, the description of the MOPA system used for the dipole trap follows.

3.2.1 External Cavity Diode Laser

Semiconductor diode lasers have quite common usage in cold atom experiments. These lasers were first used for the purpose of cooling in 1986 [39, 46] and for the trapping of caesium atoms in 1988 [47]. Their popularity originates from their easy alignment, control, compact structure and low cost compared to other lasers in same spectral range. Nevertheless, they have both advantages and disadvantages. Their low power and broad spectral linewidth are problems that can be solved easily.

The linewidth of a free running diode laser is spectrally narrowed by means of an external cavity formed with a diffraction grating mounted in the Littrow configuration, as illustrated in figure 3.2. In this configuration the beam reflecting off the grating is the output beam, whereas the first order diffracted beam is used as an optical feedback to auto-inject the laser diode. The emitted frequency of the external cavity diode laser (ECDL) laser is determined by its gain profile on which the internal cavity modes and the external cavity modes have mutual effect. A free running diode laser has a very broad gain profile so several modes might have similar gain resulting in multi-mode emission. But when it is injected with a frequency selective

element such as the grating, the internal cavity modes have different weight for the gain. The mode coinciding with the external cavity mode determined by the grating is the most favored mode. Therefore, the frequency fed back to the diode laser gains more power compared to other modes and subsequently becomes dominant. In consequence, the feedback from the grating is frequency selective and the orientation of the grating determines the center frequency of the laser diode. Another factor affecting the emitted center frequency in addition to the orientation of the grating is the length of the external cavity as it determines the resonant modes. When both the grating orientation and the cavity length cause change in frequency synchronously mode-hop suppression is achieved [48].

The output beam of a diode laser is very astigmatic and divergent. Therefore, the assembly of an external cavity diode laser starts with correcting the beam. First of all, the beam is collimated by a short focal length lens with high numerical aperture, placed in front of the diode laser. Then, the external cavity is formed by a holographic diffraction grating which is oriented in such a way that the first diffraction order of the beam is reflected back into the diode laser and the zero order becomes the output beam. Next, the astigmatism of the output beam is corrected with a pair of anamorphic prisms, which changes the elliptical shape of the laser beam into a circular shape.

The frequency of ECDL depends on both the operation current of the diode laser and the length of the cavity. In order to set-up the diode laser we proceed as follows. At first, the current of the diode is set close to the operational value specified by the manufacturer. Then, in order to obtain the frequency required for experiments with caesium atoms, the current applied to the laser diode is scanned until the fluorescence in a caesium vapour glass cell is observed. In order to tune the frequency more precisely, the cavity length is changed with small increments by a piezoelectric transducer element (PZT) attached behind the grating. As a result, precise control of the cavity length is achieved through the applied voltage to the PZT. On the other hand, undesired changes in the cavity length due to mechanical vibrations and thermal expansion must be avoided to retain the stability of

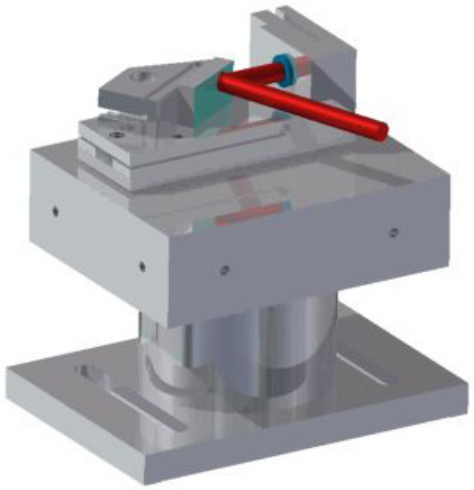

Figure 3.2: Illustration of our external cavity diode laser in the Littrow configuration. The light emitted from the laser diode is collimated with a lens and then reflected by a diffraction grating. The first order diffracted beam is fed back into the laser diode to provide feedback and the zeroth order beam is used as output beam.

the laser frequency. The former is achieved by enclosing the entire setup in an aluminum box. And the latter one is accomplished by placing the entire mounting block on a Peltier element in order to regulate the temperature that is stabilized via a servo controller with an AD590 temperature sensor.

Although the optical feedback from the grating significantly reduces the linewidth of the laser, its frequency has still tendency to drift. In order to employ diode lasers in laser cooling experiments, their frequency should be locked to a particular atomic transition as described in subsection 3.2.2. For this purpose a portion of laser output is used for frequency stabilization and usually the remaining power is insufficient for the experiment. In order to overcome this power problem, an injection-locking method is used by adopting a master-slave configuration [49]. In this configuration, a small amount of master laser output is sent into a free running slave laser to inject it. Under the right conditions of current and temperature, the slave laser carry the same spectral characteristics with the master laser. Therefore, in this method only the frequency of the master laser is locked and its frequency

characteristic is transferred to the slave laser by means of optical injection without the need for an external cavity and further frequency stabilization. Thus the entire power of the slave laser is available for the experiment.

3.2.2 Frequency Stabilization

In laser cooling and trapping experiments, a stability of the laser frequency of the order of the linewidth of the atomic transition is required. Therefore, an active frequency stabilization was implemented to lock the laser frequency to a particular atomic transition. The method used in our setup to perform this stabilization was the Doppler Free Dichroic Atomic Vapour Laser Lock (DF-DAVLL) [50]. This method is based on the creation of a Zeeman shift in degenerate atomic states and the introduction of a dichroism in an atomic vapour. This can be explained by considering a $J_g = 0 \rightarrow J_e = 1$ transition with $m = 0, \pm 1$ magnetic sublevels, which are degenerate in the absence of a magnetic field. Thus the σ_+ and σ_- polarization components of a laser field are absorbed equally. However, in the presence of a weak magnetic field the degeneracy in the magnetic hyperfine levels is lifted so that the there is a difference in the absorption rates of these shifted Zeeman components depending on the polarization of the laser beam used. The σ_+ polarized beam drives the transition $\Delta m = +1$ and the σ_- polarized beam drives the transition $\Delta m = -1$, hence the difference in their absorption generates the error signal from the atomic reference for the stabilization.

In the experiment, a homogeneous weak magnetic field is applied to the vapour cell. In this way, the magnetic levels of the atoms are split and the medium becomes dichroic. A portion of the output power of the laser is used to obtain two counterpropagating pump and probe beams passing through the vapour cell as illustrated in figure 3.3. The linearly polarized resonant beam passes through the cell and then it is retro-reflected. As the linearly polarized beam is composed of equal amplitude of two orthogonal circularly polarized beams, while passing through the vapour cell the center frequencies of their absorption profiles are shifted by equal amounts but opposite sign due to Zeeman effect. The intensities of these circularly polarized components can

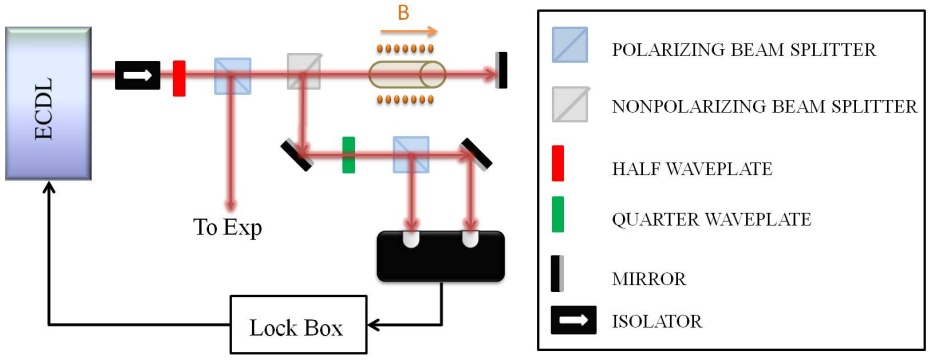

Figure 3.3: Schematic of the Doppler Free Dichroic Atomic Vapour Laser Lock. A small portion of the laser output was sent through the non-polarizing beam splitter and the vapour cell. This beam acts as a pump beam while the retro-reflected beam acts as the probe beam. The magnetic field applied to the atomic vapour along the propagation direction of the beam induces a dichroism in the medium. Therefore, the rates of absorption become different for two orthogonal circular polarizations of the beam. In order to analyze this the probe beam passes through a quarter-wave plate and a polarizing beam splitter. This decomposes the linearly polarized probe beam into two orthogonal linearly polarized beams. Then the intensities of these beams are electronically subtracted from each other at the photodiode providing the desired error signal for the stabilization.

be analyzed by employing a combination of a quarter-wave plate (QWP) and a polarizing beam splitter (PBS), which decomposes the linearly polarized beam into two orthogonal circularly polarized beams. Then the intensities of these circularly polarized beams are monitored by a pair of photodiodes and electronically subtracted from each other . Their subtraction generates the antisymmetric dispersion like error signal for the stabilization. Thus the frequency of the laser can be locked to the zero crossing point of the error signal, where the observed net photo current is zero. As a result of this, the laser intensity fluctuations become ineffective over the laser frequency lock. Nevertheless, the magnitude of the applied magnetic field affects the shape of the error signal and subsequently the quality of the lock. As the magnitude of the magnetic field increases so does the shift of the center frequency of the absorption profiles. This leads to a shallow slope of the error signal and to an increase in the capture range of the lock point. In addition, it is possible

to change the frequency lock point either by electronically adding an offset voltage or optically by rotating the quarter-wave plate.

There are two such frequency stabilized lasers used in our setup. These are the master laser (cooling laser) and the repumper laser. The master laser is tuned to $6S_{1/2}(F = 4) \rightarrow 6P_{3/2}(F = 5)$ transition and the repumper laser tuned to $6S_{1/2}(F = 3) \rightarrow 6P_{3/2}(F = 4)$ transition, whose DAVLL error signals are shown in figure 3.4.

Optical Layout

The lasers required for magneto-optical trapping are the master (cooling) and the repumper laser. The main laser of the experimental setup is the master laser that cools the atoms with sub-Doppler cooling. It is used in master-slave configuration since the output power remaining after frequency stabilization is insufficient. The master and slave lasers are located on separate optical tables and the injection beam is carried to the slave laser via a single mode polarization maintaining fiber. The optical layout of the master and the slave lasers employed in the experiment is shown in figure 3.5. The master laser is an external cavity diode laser. The shape of the output laser beam is converted from elliptical into circular by an anamorphic prism pair. Next, the laser beam passes through the isolator that prevents optical feedback into the laser, which would affect the stability of the laser frequency. After that a portion of the laser beam is split for frequency stabilization via a DF-DAVLL. Its frequency is locked to the $6S_{1/2}(F = 4) \rightarrow 6P_{3/2}(F = 3/5)$ crossover transition. As a result, it becomes 226.5 MHz red-detuned with respect to the cooling transition $6S_{1/2}(F = 4) \rightarrow 6P_{3/2}(F = 5)$. The laser beam is then sent through a double pass acousto-optic modulator (AOM) to shift the laser frequency slightly below the cooling transition. The power of the shifted beam is not enough to operate a magneto-optical trap. Therefore it is coupled to a polarization-maintaining single mode fiber laser to carry this beam to another optical table for injecting a slave laser. To realize a double MOT two slave lasers are employed in our setup as the output power of one slave laser remains insufficient. As shown in figure 3.5 a portion of the

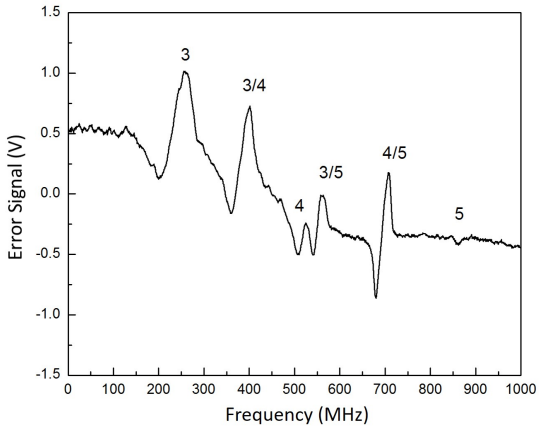

(a) master laser

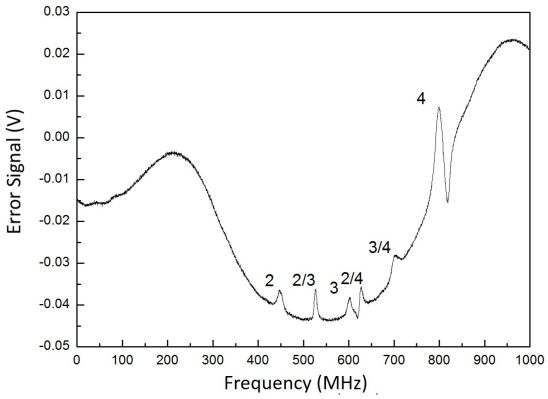

(b) repumper laser

Figure 3.4: DF-DAVLL error signals of a)master and b) repumper lasers. The upper graph indicates the error signal from the $F = 4$ ground state of Caesium. The numbers denote the excited state of the transition driven by the laser. The lower graph indicates the error signal from the $F = 3$ ground state with numbers in the figure indicating the excited state of the transition driven by the laser.

first slave laser is used to inject the second slave laser.

Another laser required to operate a MOT is the repumper laser. Its function is to compensate the leakage of atoms from the cooling transition caused by the decay of atoms from the $6P_{3/2}(F = 4)$ excited state to the

$6S_{1/2}(F = 3)$ ground state. Therefore in order to pump the atoms back to the $6S_{1/2}(F = 4)$ ground state the repumper frequency is locked to the $6S_{1/2}(F = 3) \rightarrow 6P_{3/2}(F = 4)$ transition by DF-DAVLL. The remaining power of the repumper laser after the frequency stabilization is split into two to provide repumping light for both MOTs.

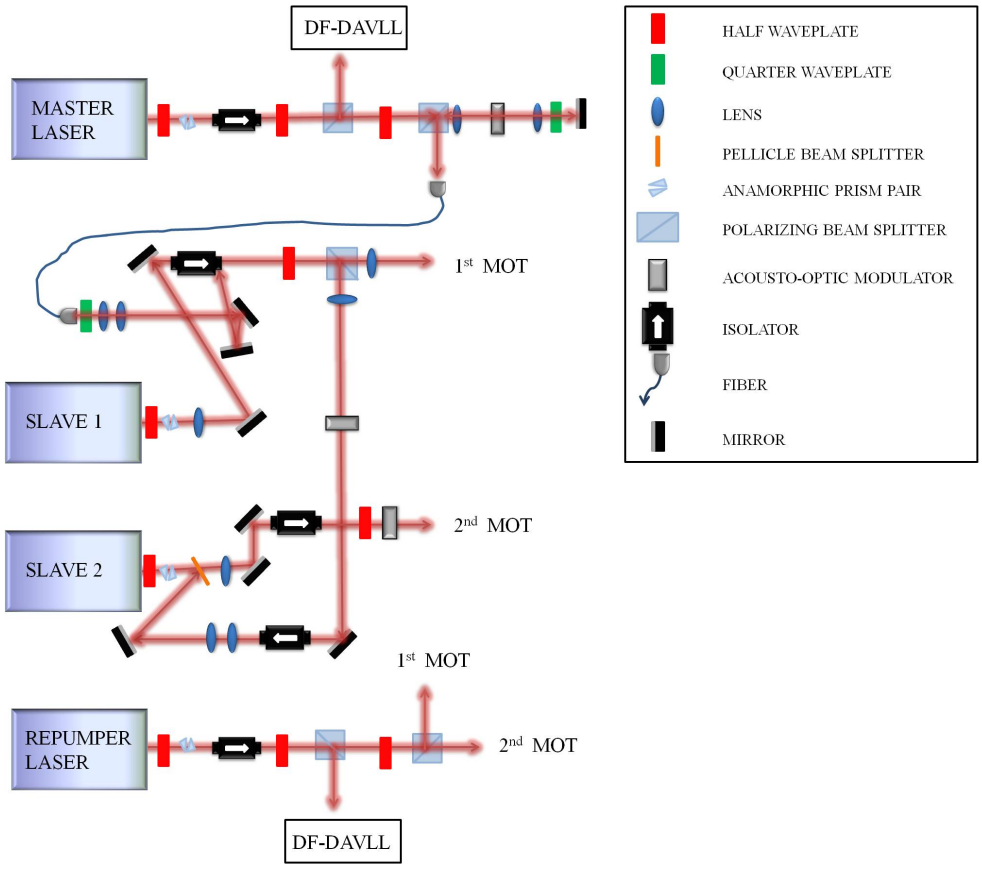

Figure 3.5: Schematics of the optical layout of the master laser, its slave lasers and the repumper laser.

3.2.3 The Dipole Trap Laser

Semiconductor lasers usually have a very low output power ranging from few mW to 50 mW because the transverse dimension of their waveguide is of the order of the wavelength to maintain single mode operation. Although this value is sufficient for most atom trapping experiments there are some mechanisms that need significantly larger output power, such as optical dipole trapping. On the other hand, broad area lasers have larger transverse dimension of waveguide so that the gain region is bigger resulting in more output power. However, despite their higher output they have the disadvantage of multi-mode operation [51]. It is possible to combine the advantages of semiconductor diode lasers and broad area lasers in one unit. Tapered amplifiers increase the power of a semiconductor diode laser while maintaining its spectral characteristic. The tapered amplifier chip consists of two regions that are straight index-guided and tapered gain-guided regions as illustrated in figure 3.6.

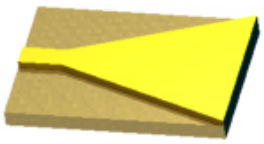

Figure 3.6: Illustration of tapered amplifier chip

To achieve amplification of power the tapered amplifier chip is injected by a master oscillator at its input facet, which then exits at the rear facet. The straight index guided part of the amplifier act as a modal filter exciting only the fundamental mode. Furthermore, in this region low input power is required to achieve sufficiently high power density. However, the straight index guided part on its own does not provide high enough power. Otherwise this causes optical Kerr effect changing the refractive index of the material depending on the intensity of the input beam. Subsequently this results in self focusing of the input and eventually cause the destruction of the chip. On the other hand, the gain-guided region of the chip is tapered in order to

maximize its efficiency by providing uniform power density amplification [52]. The tapered region ensures that the energy density does not reach a critical value so that the single mode operation is maintained. Both the front and back facets of the chip are anti reflection coated ($< 0.01\%$) to suppress the eigenmodes of the tapered amplifier chip itself, ensure a low power density in the tapered amplifier and minimize reflections as these can result in destructive interference and subsequent intensity fluctuations leading to multi-mode operation.

In our experiment, the goal was to implement a state-insensitive 2D lattice dipole trap. To achieve the required power for this, a two master oscillator power amplifier system operating at the magic wavelength of Cs (935 nm) was built. In this section, the construction and the alignment of the MOPA is described. Next, information about the optical layout of the system is given. Then it is followed by the characterization of the MOPAs.

Construction and Alignment

In our setup a master oscillator[1] acts as a seed laser to inject the single pass tapered amplifier chip[2], thus realizing a master oscillator power amplifier (MOPA) system. The mechanical construction of the tapered amplifier is shown in figure 3.7. The injection (master) beam is coupled in and the amplified beam is coupled out of tapered amplifier (TA) chip with a high numerical aperture lens[3] mounted on a fiber port[4], which allows fine alignment in five degrees of freedom. The temperature of the tapered amplifier chip is stabilized via a temperature controller since its gain profile is affected by the temperature. The chip is mounted on a copper block in order to increase the thermal inertia. The temperature is regulated by a Peltier element placed under the copper block and monitored by an AD590 sensor. The power of

[1] M9-935-0100-S50 diode laser from Axcel Photonics

[2] m2k-TA-0785-1000-DHP(F) from m2k-laser

[3] GLC-8.0-8.0-830 lens with f=8 mm NA=0.8 from Melles Griot for couple seed laser and C240TME-B lens with f=7.5 mm and NA=0.3 from Thorlabs to couple out the light from tapered amplifier chip

[4] 9095 XY fiber positioner from New Focus

the tapered amplifier is supplied by a commercial current controller[5].

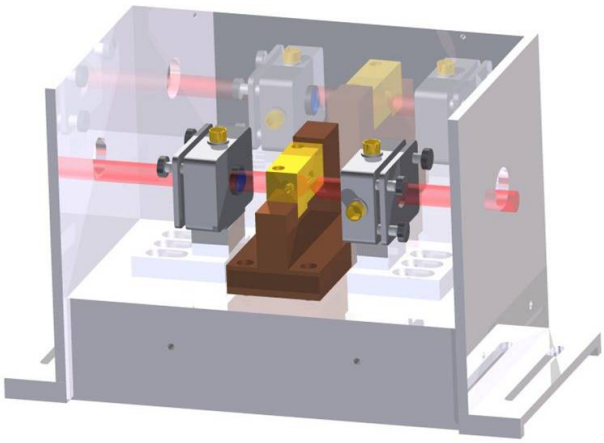

Figure 3.7: Tapered Amplifier assembly

The alignment of the TA starts with tightly focusing the injection beam onto the chip with a high numerical aperture lens. In order to ensure efficient coupling, the injection beam is overlapped with the collimated amplified spontaneous emission of the TA chip. Then the efficiency of the power amplification is optimized by adjusting the position of the focusing lens. After the amplified beam is emitted from the front facet of the TA chip it is collimated by another aspheric lens with high numerical aperture and short focal length. The horizontal dimension of the front facet of the TA chip is much wider than its vertical dimension. Therefore, the beam emitted along the horizontal axis is highly diffracted, whereas the beam diffracting along the vertical axis behaves like emitted from a point source. Hence, the focal length of the beam along two orthogonal axes are different. Consequently, the output beam collimated by the aspheric lens is highly astigmatic.

[5]LDC240C from Thorlabs

Optical Layout

The optical layout of the dipole trap laser system is shown in figure 3.8. The MOPA system consists of a master oscillator amplified by a single pass tapered amplifier. The master oscillator is a grating stabilized ECDL. Its injection beam (35 mW) is coupled to the TA by overlapping it with the amplified spontaneous emission emitted backwards from the tapered amplifier. In order to achieve mode matching between the two beams, the shape of the ECDL beam is modified. Firstly, an anamorphic prism pair was used to change the shape into circular and then a telescope is used to magnify the size of the beam. An optical isolator (40 dB) is placed between the master oscillator and the tapered amplifier to prevent feedback from the overlapped beam of the tapered amplifier to the master oscillator. In addition, an optical isolator (60 dB) is also used after the tapered amplifier to protect it from any reflection that can destroy the amplifier chip. The amplified beam emitted from the tapered amplifier is highly astigmatic. Therefore, a cylindrical lens (f = 150 mm) is placed after the tapered amplifier to correct the shape of the output beam. For the dipole trap experiment the beam quality is important. The easiest way to achieve spatial filtering of a beam is coupling it to a single mode fiber. Therefore, the size of the beam is decreased by a telescope so to be able to couple it to the fiber. Although there is a significant loss at the obtained power from the MOPA after the optical isolator (transmitting $\approx 80\%$) and the optical fiber (coupling 62%), the use of a single mode fiber is beneficial both for spatial filtering and to reduce the pointing instability of the beam.

The master oscillator laser used in our experiment is not capable of providing sufficient power for both tapered amplifiers. Therefore, it is used to inject the first tapered amplifier. Then a portion of the output of this MOPA is split to inject the second tapered amplifier. In consequence, two MOPAs having same spectral properties with the master oscillator were obtained.

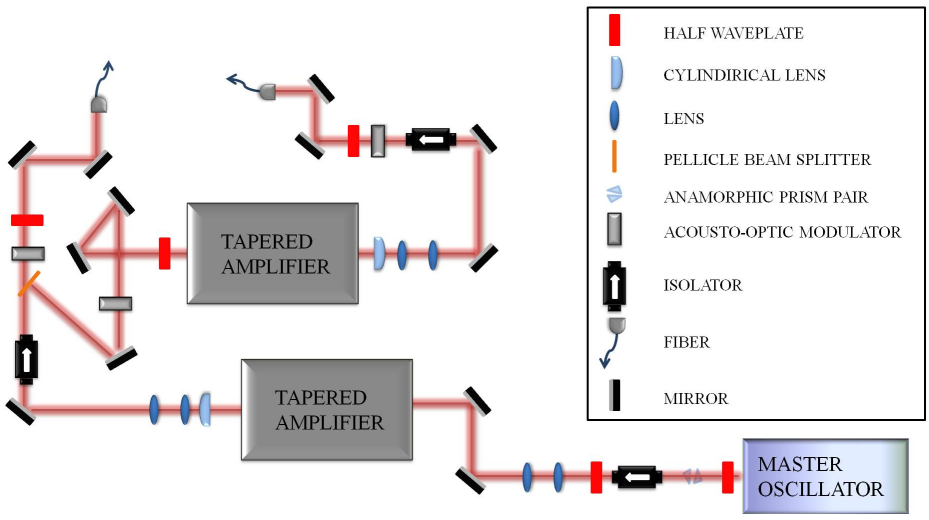

Figure 3.8: Schematics of the optical layout of the MOPA setup

Characterization

The output power of the MOPA depends on three parameters: the power of the injection beam, the operating temperature and the operating current of the tapered amplifier. In order to determine the optimum operating conditions of the MOPA, the output power of the tapered amplifier is measured for different parameters. It is found that amplified spontaneous emission of the tapered amplifier is suppressed more at lower temperatures. Therefore, the tapered amplifier is operated at $10°C$ in our setup. The output power of the MOPA was measured for various values of the operating current as shown in figure 3.9. The tapered amplifier can be operated at maximum current of 2 A without seed laser, whereas this value increases to 2.8 A with a seed laser. When the MOPA is injected it shows a threshold for output power. According to the data of figure 3.9, the threshold of the amplification is around at 1.3 A, and beyond this value the power increases linearly with the current of tapered amplifier. In order to further examine the amplification characterisctics, the output power of the TA for different values of the injection power was measured. It was observed that the output power of the tapered amplifier at fixed operating currents increases linearly and then

quickly saturates at certain seed power as shown in figure 3.10. This value approximately corresponds to 30 mW.

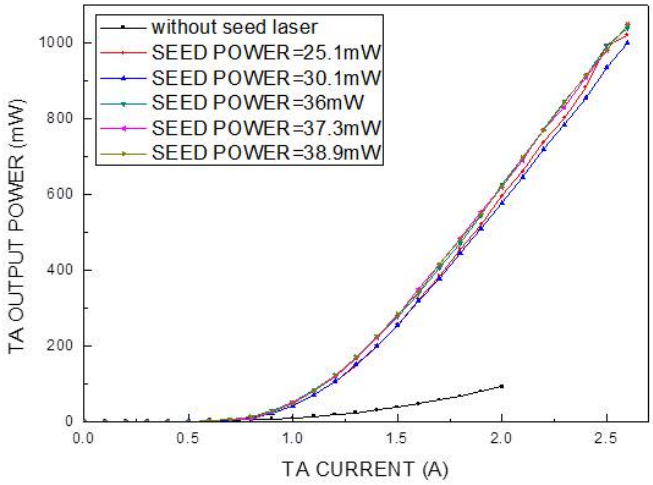

Figure 3.9: TA power characterization for different operating currents

In order to verify the injection of the two tapered amplifiers the beat signal of their output was detected via a ultrafast photodiode. The resulting beat-note signal is shown in figure 3.11. The detected beat note signal have a width of 71.12 kHz indicating an efficient injection of the tapered amplifiers by the seed laser.

Technical noise induced by the laser, such as beam pointing instability and intensity fluctuation, is a well known problem in dipole trapping. These noises cause fluctuations in trap depth and thus have an appreciable limiting effect on the lifetime of the trapped atoms. By coupling the trapping beam to a fiber, noise due to pointing instability was converted into intensity fluctuations. The intensity fluctuations of the tapered amplifier was stabilized by monitoring portion of the beam coupled to fiber, which is fed back to a feedbeack circuit to control the intensity variations via an acousto-optic modulator. Then, appreciable portion of the beam was used by the acousto-optic modulator to compensate for the variations in the intensity. This resulted

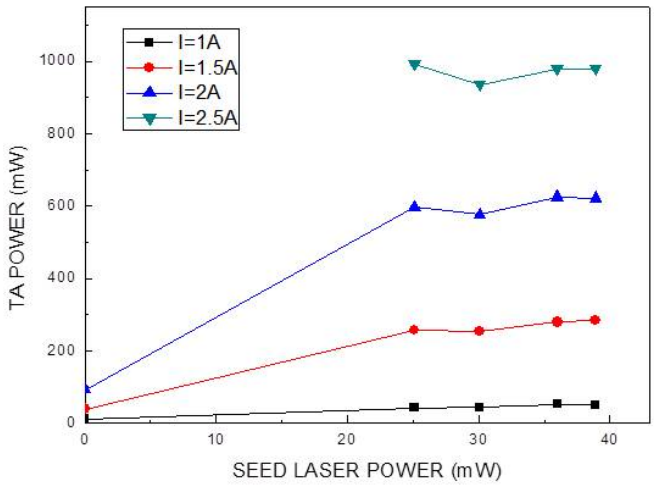

Figure 3.10: Tapered amplifier power vs seed laser power for different injection current of the tapered amplifier

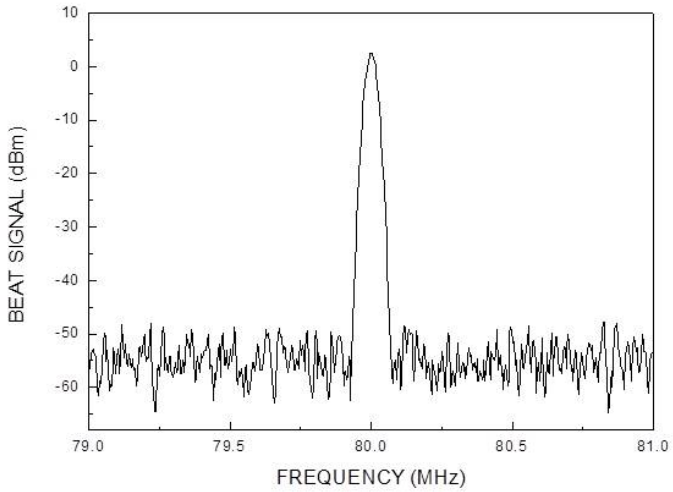

Figure 3.11: Beat-note signal of two tapered amplifiers

in a further loss in the achieved power from the MOPA system. First 16% of the power emitted by the tapered amplifier was lost after the collimation

optics and the optical isolator. A portion (11%) of the remaining power was used to inject the second tapered amplifier. Then, 30% of the laser beam was used for intensity stabilization by acousto-optic modulator and the stabilized beam is coupled to the optical fiber with 62% efficiency. Despite the power emitted by the tapered amplifier is 1 W (for the injection current of 2.5 A), final power achieved after the fiber is 290 mW. However damage in the tapered amplifier chip led to destruction of the MOPA system. Since the maximum output power of the master oscillator at magic wavelength of 935.6 nm is ≈40 mW, which is insufficient to deep optical potentials. This makes single frequency state-insensitive trapping impractical. To overcome this problem, bichromatic trapping is proposed and possible magic wavelength combinations are theoretically determined in the next chapter.

3.2.4 Implementing Bichromatic State-insensitive Trap

The idea of bichromatic trapping is based on combination of two optical dipole traps at different wavelengths. By a proper choice of intensity ratio of the two trapping beams, the effect of the light field can be balanced to achieve state-insensitive trapping. The main technical challenge of bichromatic trapping is to setup the combined trap. It can be realized in crossed-beam or two parallel superposed single beam configuration.

The bichromatic trapping can be integrated in the existing experimental setup for the single-frequency state-insensitive trapping. Illustration of the bichromatic scheme which consists of two superposed single tapping lasers is given in figure 3.12, which are orange Raman fiber laser operating at 585 nm and Nd:YAG laser operating at 1064 nm. Since high power lasers work sufficiently stable only at high output power, required amount of power is achieved by directing the laser beam onto a polarizing beam splitter. Thus, a portion of the output power is used for the trapping whereas the remaining power is blocked by a beam dump. The typical optical layout is similar for both trap lasers. The laser beam is collimated by a telescope and passed through an acousto-optic modulator which is used for fine adjustment for the power of the laser beam and as a switch to turn on and off the trapping

beam. Then the trap beam is spatially filtered by a single mode polarization-maintaining fiber. It also reduces pointing instability of the laser beams, which is important as the two trapping beams must be spatially overlapped. Next, the two optical trapping beams of 585 nm and 1064 nm are combined by a polarizing beam splitter. The required parameters for these two trapping beams were investigated in detail in section 4.4. According to the calculations the required intensity ratio of the two lasers for state-insensitive trapping is $I_{\lambda=585}/I_{\lambda=1064}= 0.42$. The spot size of 5 μm for both lasers is obtained by the objective lens (described in section 3.3) with beam waists of 2.6 mm and 4.9 mm for 585 nm and 1064 nm respectively. MOT beams and optical trap beams are aligned along the same axis because of limitations in optical access to the science cell in our setup. To combine these beams a dichroic mirror (reflects the MOT beam and transmits the optical trap beam) is used. As shown in figure 3.12, there is a lens before the dichroic mirror to focus the MOT beam. In this way, the objective lens collimates the MOT beam whereas it focuses the dipole trap beam. Both the objective lens and the optics after the fiber are mounted on a xyz-translational stage, which allow fine adjustment for focus position of the objective lens.

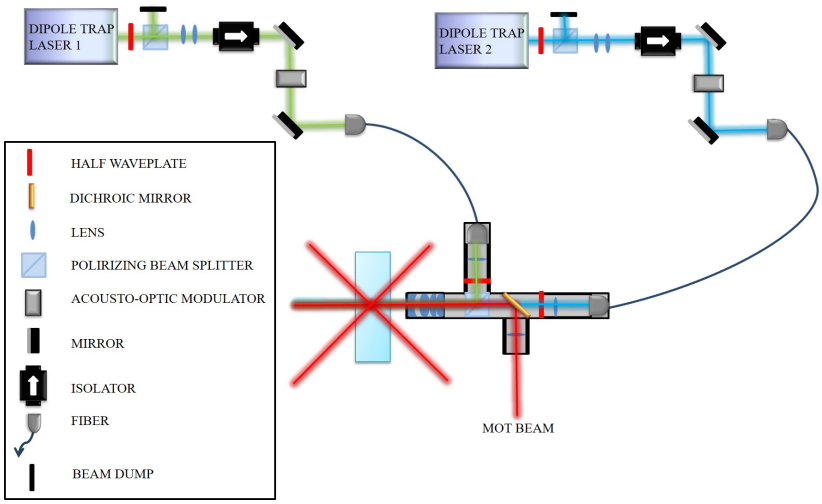

Figure 3.12: Illustration of bichromatic trapping scheme

When the state-insensitive trapping is realized, the AC Stark shift caused by the trapping light vanishes. Therefore, in order to experimentally test a magic wavelength, the induced light shift is measured. The validity of magic wavelength combination of $585 - 1064$ nm can be tested by comparing the induced light shift for different trapping wavelengths. Accordingly, one of the wavelength is tuned around the specified magic value (585 nm) whereas the other one remains fixed (1064 nm). The light shift induced by the trapping laser can be measured by another laser. A blue-detuned depumper laser is shifted up by an acousto-optic modulator to be on resonance with $6S_{1/2}F_g = 4 - 6P_{3/2}F_g = 3$ transition, which is shifted because of the optical trapping beams. To measure the light shift of this transition number of trapped atoms is measured for a fixed holding time as a function of detuning of the depumper laser for each trapping wavelength. When the differential AC Stark shift of $6S_{1/2}F_g = 4 - 6P_{3/2}F_g = 3$ transition is compensated by controlling the detuning of the depumper laser, the number of trapped atoms will be maximum. As the light shift vanishes in case of state-insensitive trapping, maximum number of atoms are trapped at magic wavelength without requiring detuning of the depumper laser.

3.3 Imaging System

An imaging system with high sensitivity and resolution is required in micro dipole trap experiments. In our experiment trapped atoms are observed by detecting the fluorescence signal with two types of detectors: an intensified CCD camera (ICCD) and a single photon counting module (SPCM). In this section, the image forming optics, the working principles of the intensified CCD camera and of the single photon counting module are described.

3.3.1 Image Forming Optics

Illustration of our imaging system is given in figure 3.14. The fluorescence of trapped atoms is assumed to be isotropically distributed. A fraction of fluorescence signal is collected and collimated by the objective, which is one

of the building blocks of the imaging system. Our objective is adapted from a design by Wolfgang Alt [53]. It consists of four BK7 lenses mounted in an aluminum tube with a numerical aperture (NA) of 0.29, a solid angle of 0.021, a diffraction limited spot size of 2.4 μm and a focal length of 43.4 mm at 852 nm. Fluorescence imaging requires efficient collection of photons, suppression of stray light and low noise. Fluorescence not originating from the trapped atoms is undesired as it contributes to the background noise. Therefore, in order to suppress the background light the rest of the imaging optics are mounted in a black plastic tube. Behind the objective lens a dichroic mirror is placed, which reflects light at 852 nm and transmits at 935 nm. In order to achieve a fine alignment, the objective lens and the dichroic mirror are mounted on a xyz translational stage. Then a bi-convex lens with a focal length of 500 mm is placed to focus the fluorescence signal on both the intensified CCD camera and the single photon counting module. In order to further reduce the effect of the background light adjustable irises are placed between the objective lens and the intensified CCD camera. Finally at the end of the tube the light beam is divided into two by a non-polarizing beam splitter and sent to the intensified CCD camera and the single photon counting module. In order to block undesired wavelengths and reduce the background noise, bandpass filters are placed in front of both detectors.

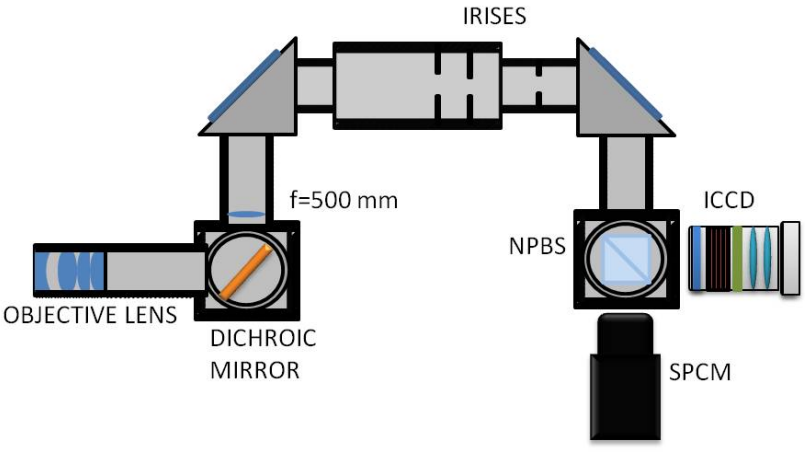

Figure 3.13: Schematics of the Imaging System

3.3.2 Working Principle of the Intensified CDD Camera

The intensified CCD camera is used to collect the image formed by the optical system described in the previous section. It consists of a image intensifier unit connected to a digital CCD camera through a $1:1$ relay lens. Use of a low noise cooled CCD on its own requires an exposure time varying between few seconds to minutes for efficient imaging of a small cloud of atoms. However, the integration of the intensifier unit reduces the required exposure time to the millisecond range. Basically, an intensifier unit is a high-voltage vacuum tube, consisting of a photocathode plate at the input, a phosphor screen on the output and a microchannel plate (MCP) in between them as illustrated in figure 3.14. The photons passing through the intensifier unit strike the photocathode plate and subsequently electrons are emitted due to the photoelectric effect. The probability for an electron to be emitted is determined by the quantum efficiency of the photocathode. Our intensifier unit has a multialkali photocathode having a quantum efficiency of 2% at 852 nm and spectral response between 185 nm and 900 nm. Then the electrons emitted from the photocathode are accelerated towards the microchannel plate by an electric field that can be controlled. The microchannel plate is a conductive glass substrate consisting of millions of parallel traversing microchannels so that the electrons passing through each microchannel leads to the emission of secondary electrons. As the electrons strike several channels, this results in the emission of thousands of electrons. By tuning the electric field accelerating the electrons, the gain of the amplification can be controlled. At maximum gain, an amplification factor of around 10^6 electrons per input electron emission is achieved. Finally, the electrons leaving the MCP hit the phosphor screen, where their kinetic energy is converted into emission photons with wavelength of 500 nm.

Then the emitted photons couple to the digital CCD camera, which has a quantum efficiency of 70% at 500 nm. The CCD camera is operated at $-30°C$ via a Peltier element in order to reduce dark current noise originating from thermally generated electrons. The CCD chip consists of 1344×1024

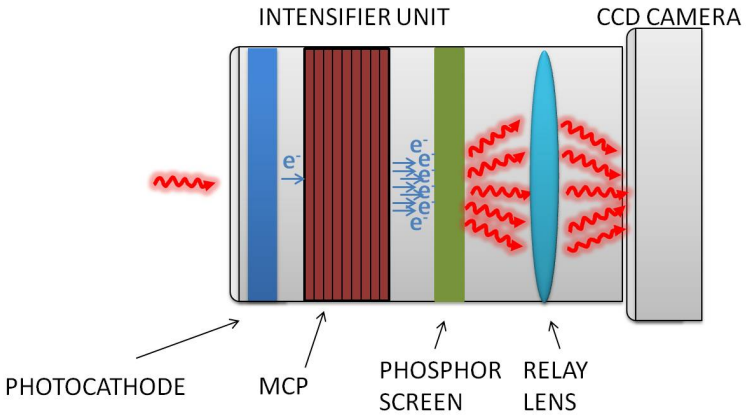

Figure 3.14: Working Principle of the ICCD Camera: photons entering the intensifier unit are converted into electrons at the photocathode and accelerated towards the microchannel plate. As the electrons pass though the microchannel plate secondary electrons are emitted and they are converted into photons again at the phosphor screen. Then the photons are imaged on the CCD camera via a $1:1$ relay lens.

pixels each with dimensions of $6.45 \times 6.45\ \mu m$ and readout resolution of 12 Bits. After the image is acquired by the camera the signal is sent to a computer through a serial bus IEEE 1394 (Fire Wire), which allows to control the exposure time and triggering for synchronization with sequence of the experiment. The intensifier unit is connected to computer via USB connection, which enables control of gain independently of the CCD camera.

3.3.3 Working Principle of the Single Photon Counting Module

Working with a small number of atoms requires high sensitivity detectors such as the single photon counting module (SPCM). It uses a silicon based avalanche photodiode (APD) that is capable of counting single photons over the wavelength range of $400 - 1060$ nm. It is basically a p-n diode with high gain consisting of two regions: an absorption region where the incoming photons are absorbed and a multiplication region where a high electric field provides current gain through avalanche multiplication due to impact ion-

ization. In Geiger mode operation, an APD is biased above its breakdown voltage and it conducts large currents. Therefore a single photon can generate current in detectable range. When a photon is detected, a TTL pulse with width of 15 ns is emitted at the output of the detector. But there is a dead time of 35 ns between each pulses and the dark count rate of the detector is 350 counts/s.n The emitted TTL pulses are counted by ORTEC 449 ratemeter within 100 ms time interval. In this way TTL pulses are converted into voltage which is displayed and recorded by an oscilloscope.

Chapter 4

Bichromatic State-Insensitive Trapping of ^{133}Cs

The core of the results presented in this chapter was also published in M. M. Metbulut, F. Renzoni, *Bichromatic state-insensitive trapping of caesium atoms*, Journal of Modern Optics 62.sup2 (2015): S52-S58.

4.1 Introduction

The dipole trap is one of the corner stones of the progress in cold atom experiments. It has found rapidly increasing usage in experiments on single atom manipulation [54], precision spectroscopy [22], atomic clocks [22, 55], degenerate Fermi gases [56, 57], cold molecules [58] BEC [59], quantum control [60] and quantum spectroscopy [61].

The dipole trap is based on interaction between the intensity gradient of the light field and the induced dipole moment of the atom. However, the light field produces a spatial dependent differential AC Stark shift between the different internal states of the atoms. In general the AC stark shifts of the ground and excited states of an optical transition of interest are different. Such a differential light shift has to be taken into account as it causes severe drawbacks. For instance, it causes a line shift and its spatial dependence leads to a line broadening, which introduces difficulties in continuous

monitoring of trapped atoms. Moreover, it significantly limits the coherence time, which is an important parameter in experiments involving quantum state manipulation [20]. It also affects the operation of free space laser cooling techniques. It prevents efficient loading of atoms from a magneto-optical trap into an optical trap, and causes motion-induced dephasing of the atoms [21, 22].

In 1999 Katori *et* al. proposed a new approach to cancel the differential light shift in the context of optical lattice clocks [23]. By taking advantage of the interaction of the dipole trap laser field with all the different transitions of the multilevel atom, he suggested to tune the trapping laser wavelength in a way that the light shift of the ground and the excited state of a transition of interest become equal. The specific wavelength fulfilling this condition is called "*magic*" wavelength. The use of the magic wavelength was first demonstrated for a strontium optical lattice clock, allowing for simultaneous laser cooling and dipole trapping. Later in 2003, it was demonstrated by McKeever et al. that state-insensitive trapping of caesium atoms within an optical cavity provides for an extended lifetime and allows continuous monitoring of trapped atoms [62].

In addition to strontium and caesium atoms the magic wavelengths of several other atoms such as magnesium [63], barium [64], radium [64], mercury [65], lithium [66], rubidium [67] and calcium [68] have been determined. However, some of the determined magic wavelengths are impractical in terms of experimental realization of state-insensitive trapping. More specifically, the identified magic wavelengths may be in an inappropriate frequency range for current laser technology, either in terms of wavelength or power required. Additionally, the polarizability of the atom at the required wavelength may be too small to achieve efficient trapping. The former was the case for the Caesium atom with 290 mW output power at free space. However, the MOPA system was broken due to destruction of tapered amplifier chip. The total output power using only the master oscillator (35 mW) was barely enough for performing efficient dipole trap experiment. The power obtained after optics, intensity stabilization and the fiber was 20 mW, which provides 0.35 mK trap depth for beam waist of 5μ. To be able to obtain a trap depth more

than 1 mK a light source with output power more than 100 mW is required.

We thus propose bichromatic state-insensitive trapping to address the aforementioned problems associated with single frequency state-insensitive trapping. Bichromatic trapping was first proposed by Arora et al. [69] for rubidium atom since the magic wavelength for monochromatic trapping was inconvenient due to the atomic polarizability being too small for efficient trapping. In contrast to rubidium, the main difficulty for single frequency state-insensitive trapping of caesium atoms in free space is the lack of laser sources with sufficiently high power. We thus investigated bichromatic state-insensitive trapping of caesium atoms to identify magic wavelength combinations more convenient than the monochromatic magic wavelength of 935.6 nm.

Bichromatic state-insensitive trapping mechanism is based on the combined effect of the two independent light fields. One of the lasers is used as the trap laser and the other one is used as a control laser to compensate for the different AC Stark shifts in the ground and excited states of the optical transition of interest. At variance from monochromatic trapping scheme, there are four experimental control parameters; the intensity and wavelength of both lasers. Thus, the combined effect of the two lasers may cancel the differential shift between the two states of a particular optical transition for various combinations of parameters leading to state-insensitive trapping over a wide range of wavelengths. By choosing appropriate sets of parameters, state-insensitive trapping can be achieved at a specific value of wavelength combination. Therefore, bichromatic trapping may be a viable tool to extend the range of magic wavelengths.

4.2 AC Stark Shift with Two Laser Fields

In this chapter, we present our study of bichromatic trapping of Cesium atom to determine the combinations of trap and control laser wavelengths providing state-insensitive trapping. The AC Stark shift in the presence of a single laser field was previously calculated by using time-independent per-

turbation theory in subsection 2.5.2 and given by the formula 2.46 including all the hyperfine levels and the corresponding Zeeman sublevels. This is particularly important whenever the trapped atoms are prepared in a specific Zeeman sublevel. Following the same approach, we evaluate the AC Stark shift of the ground and excited states of the Caesium atom separately as functions of the trapping laser wavelength in the presence of two lasers with the aim of determining convenient sets of wavelengths to eliminate the differential AC Stark shift between the ground and excited states of the D_2 line transition. In the presence of the two laser fields the modified Hamiltonian can be written as

$$H = H_0 + V_1 + V_2, \tag{4.1}$$

where H_0 is the unperturbed Hamiltonian, V_1 is the perturbation due to first laser field and V_2 is the perturbation due to second laser field. Therefore, the resulting effective AC Stark shift can be obtained by adding the AC Stark shift for each laser field

$$\Delta E = \Delta E_1 + \Delta E_2. \tag{4.2}$$

The AC Stark shift of the $6S_{1/2}$ ground state and $6P_{3/2}$ excited state of the Caesium atom in the presence of a single laser source was computed and plotted in subsection 2.5.2 using mathematica. The calculations presented in this chapter are also carried out for linear polarization of both lasers as it is the most widely used configuration for optical dipole trap. Contributions from the couplings to the excited states up to 12S, 12P and 9D were taken into account. The corresponding transition frequencies and Einstein coefficients are taken from the references [34–36] and listed in appendix B.

4.3 Calculation of Wavelength Pairs For Fixed Ratio of Wavelengths

Calculations performed start with considering the particular case of laser wavelengths in the 1 : 2 and 1 : 3 ratio, with particular attention to the infrared region of the spectrum. This corresponds to pairs of laser fields with one obtained from the other one via second-harmonic and third-harmonic generation respectively. The appropriate combinations were first determined for equal intensity of 2×10^9 W/m^2 of the trap and the control lasers. To identify the magic wavelengths, the AC Stark shift of the ground and excited states of the $6S_{1/2}(F = 4) \rightarrow 6P_{3/2}(F = 5)$ transition are plotted as functions of trap laser wavelength for $\lambda_{control} = 2\lambda_{trap}$ and $\lambda_{control} = 3\lambda_{trap}$ in figures 4.1 and 4.2 respectively. As shown in the figures, the Zeeman sublevels of the excited state are splitted whereas they remain degenerate for the ground state. The results of the numerical calculations of the figures 4.1 and 4.2 indicate that the magic wavelength combinations of the trap and control lasers are $931.8 - 1863.6$ nm and $927.5 - 2782.5$ nm for the case of $\lambda_{control} = 2\lambda_{trap}$ and $\lambda_{control} = 3\lambda_{trap}$ respectively.

Given that state-insensitive trapping in bichromatic schemes requires an appropriate choice of the relative intensities of the trap and control lasers at specific wavelength combinations, it introduces a degree of tunability of the magic wavelength combinations. The flexibility it offers in the range of magic wavelengths is illustrated in figure 4.3 for both $\lambda_{control} = 2\lambda_{trap}$ and $\lambda_{control} = 3\lambda_{trap}$ cases, where the magic trapping wavelength is calculated as a function of the intensity ratio of the trap and control lasers. The data reported demonstrates the tunability of the magic wavelength in a range of 10 nm, by changing the relative intensities of the lasers. This shows that the bichromatic trapping scheme allows to tune the magic wavelength by varying the relative intensities of the lasers. Therefore, it significantly extends the range of possible magic wavelength sets compared to the monochromatic case.

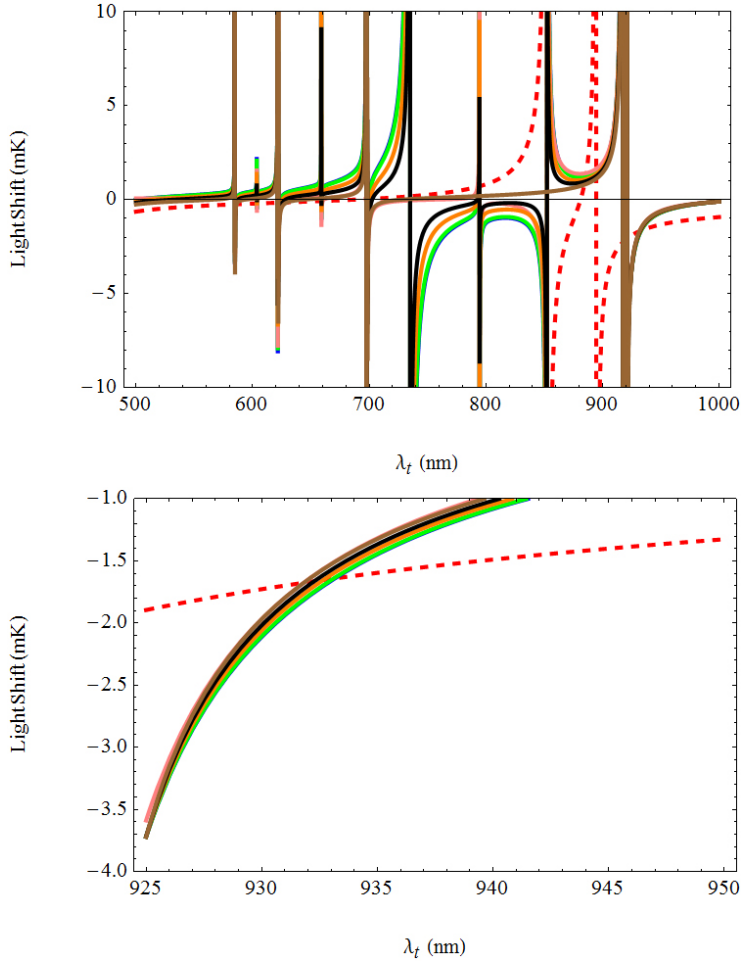

Figure 4.1: AC Stark shift for $F_g = 4 \rightarrow F_e = 5$ transition with $\lambda_{control} = 2\lambda_{trap}$ as function of the trap laser wavelength. The intensities of the trap and control laser are equal and kept at 2×10^9 W/m^2. Red dashed line refers to the ground state $6S_{1/2}$, blue, green, pink, orange, black and brown lines refer to the excited state $6P_{3/2}$ with $m = 0, \pm1, \pm2, \pm3, \pm4, \pm5$ Zeeman sublevels respectively. The bottom panel is the magnification of the region around a wavelength defining a state insensitive trap.

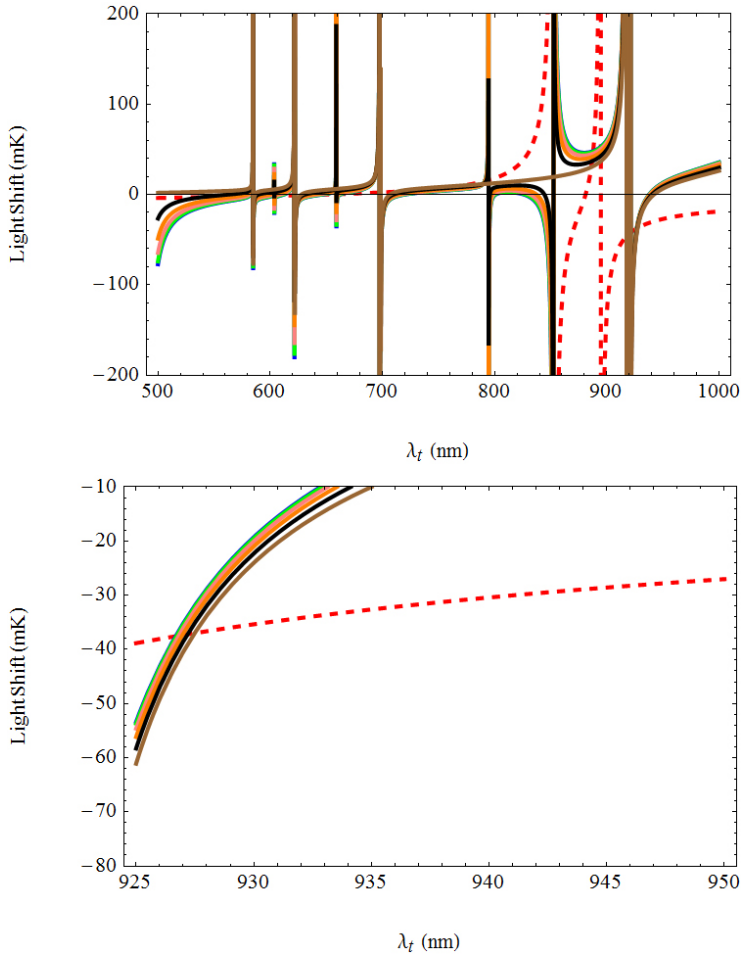

Figure 4.2: AC Stark shift for the $F_g = 4 \rightarrow F_e = 5$ transition with $\lambda_{control} = 3\lambda_{trap}$ as a function of the trap laser wavelength. The intensities of the trap and control laser are equal and kept at 2×10^9 W/m^2. Red dashed line refers to the ground state $6S_{1/2}$, blue, green, pink, orange, black and brown lines refer to the excited state $6P_{3/2}$ with $m = 0, \pm1, \pm2, \pm3, \pm4, \pm5$ Zeeman sublevels respectively. The bottom panel is the magnification of the region around a wavelength defining a state insensitive trap.

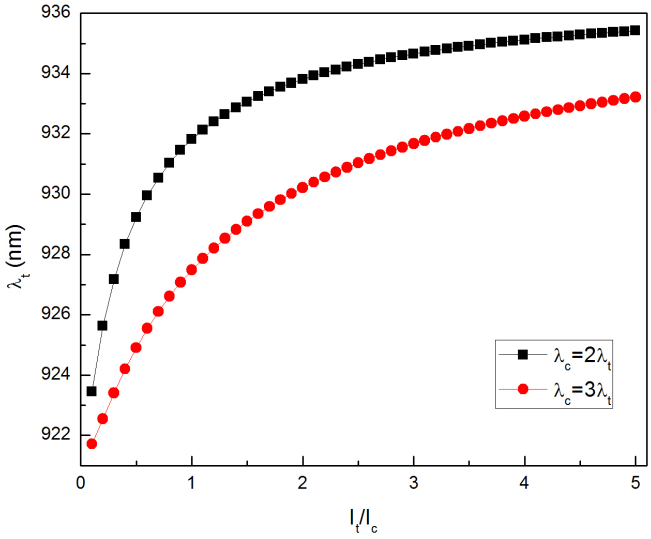

Figure 4.3: Trap laser wavelength versus intensity ratio of trap and control lasers.

4.4 Determination of Magic Wavelength Pairs Accessible by High Power Lasers

As pointed out previously, our main motivation for investigating bichromatic state-insensitive trapping schemes for Caesium atom was the lack of a single laser source operating at the magic wavelength of 935.6 nm with sufficiently high power (> 100 mW). Therefore, the bichromatic state-insensitive trapping approach is considered to identify possible magic wavelength combinations, which can be obtained by commercially available high power lasers.

For all calculations carried out in this section the control laser power was fixed to 2 W and the beam waists of both trap and control lasers to 10 μm. The appropriate magic wavelengths of control laser to achieve state-insensitive trapping were found to be 1064 nm, 1070 nm, 1075 nm and 1080 nm, which can be obtained by employing Nd:YAG and Ytterbium fiber lasers. And, the corresponding magic trap wavelength accessible by high power lasers for all these control laser wavelengths were found in range of $585 - 588$ nm

and $623-629$ nm which can be achieved by employing orange and red Raman fiber lasers respectively, in which a Yb-fiber laser produces stimulated Raman scattering in a second fiber leading to infrared Raman emission frequency doubled into the orange/red region of the visible spectrum. The calculation of the AC Stark shift of the $6S_{1/2}(F = 4) \rightarrow 6P_{3/2}(F = 5)$ transition for the control laser wavelength of 1064 nm is presented in figure 4.4. The two corresponding magic trap wavelengths are identified as 586.1 and 627.8 nm. The uncertainty resulting from the input data [34–36] was observed to have negligible effect on the calculated magic wavelengths. For instance, at magic wavelength of 627.8 nm the uncertainty of the differential AC Stark shift of the $6S_{1/2}(F = 4) \rightarrow 6P_{3/2}(F = 5)$ transition is $3 \times 10^{-}5$ mK.

The calculations in the previous section 4.3 demonstrated the tunability of the magic wavelength combinations of the trap and control lasers by changing their relative intensities in bichromatic scheme. Such a tunability applies also to the laser wavelength combinations considered in this section. The dependence of the required ratio between the trap and the control laser intensities on the wavelength of the trap laser is shown in figure 4.5 for control laser wavelengths of 1064 nm, 1070 nm, 1075 nm and 1080 nm. As shown in figure 4.5, for all of the four control laser wavelengths, the required intensity ratio of the trap and the control lasers exhibit an approximately linear dependence on the corresponding wavelength of the trap laser. Thus, bichromatic trapping offers precise tunability over a wide range of wavelengths. Nevertheless, there is a limit on the possible tuning range of the magic wavelength. The displayed data in figure 4.5 demonstrates that as the magic trap wavelength increases, the intensity of the trap laser relative to the control laser also has to increase to maintain the condition of state-independent trapping. But, this leads to a decrease in the trap depth due to the increase in detuning. This is quantified in figure 4.6 for all the four magic wavelengths of the control laser, which confirms that the magnitude of the trap depth is inversely proportional to the trap wavelength. Indeed, this sets a limit to the range of trap wavelengths usable for state-independent trapping despite the flexibility introduced by bichromatic trapping scheme.

Another important aspect for practical applications is the removal of the

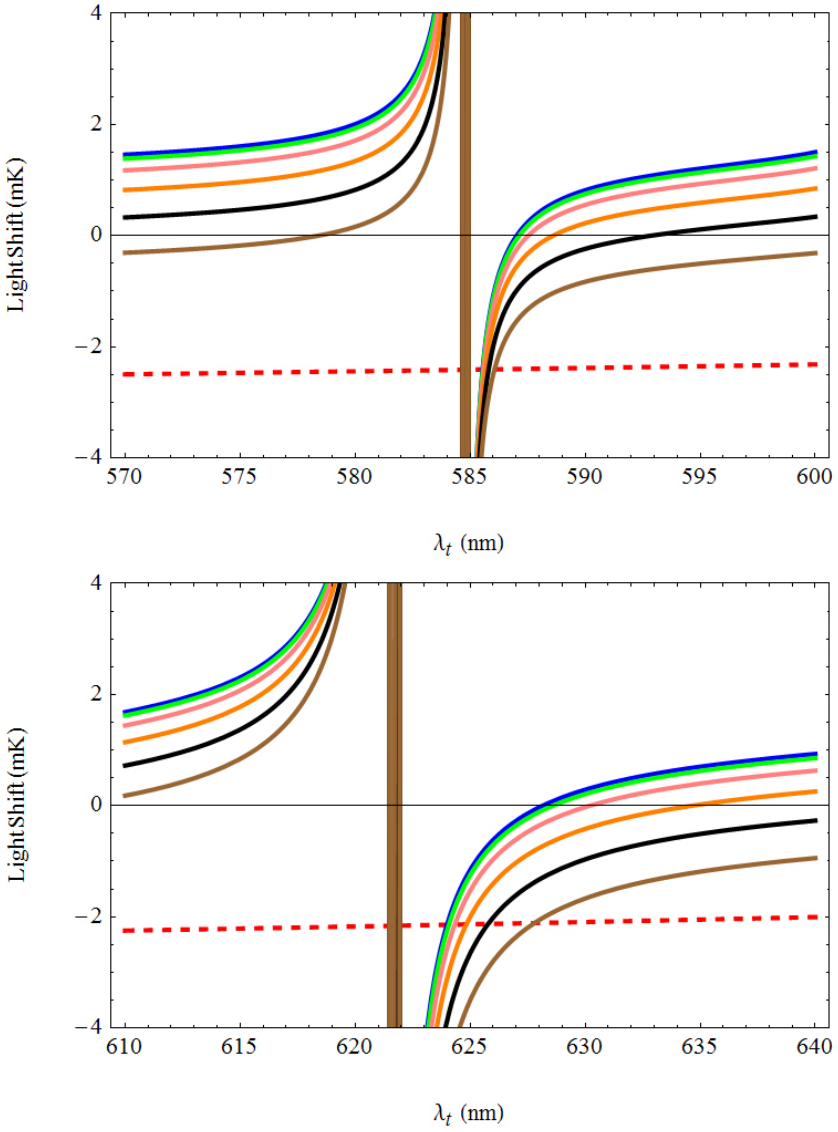

Figure 4.4: AC Stark shift for the $6S_{1/2}$ $F_g = 4 \rightarrow 6P_{3/2}F_e = 5$ transition as a function of the trap laser wavelength. The control laser wavelength is 1064 nm and power is 2W with beam waist of 10 μm. The red dashed line is the ground state $6S_{1/2}$ and the other bold lines are the are $m = 0, \pm1, \pm2, \pm3, \pm4, \pm5$ Zeeman sublevels of the excited state $6P_{3/2}$

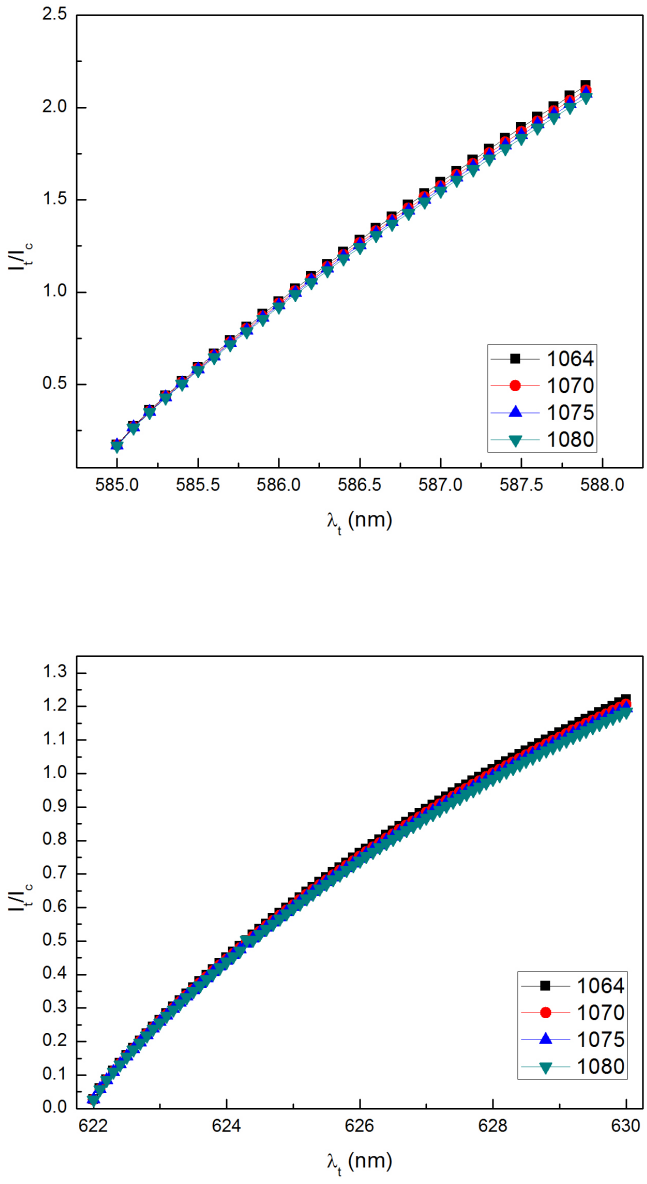

Figure 4.5: Dependence of the required intensity ratio between the trap and the control lasers on the wavelength of the trap laser for a control laser wavelength of 1064 nm, 1070 nm, 1075 nm and 1080 nm. The top panel refers to state-insensitive trapping obtained with a trap laser wavelength in the range of $585 - 587.9$ nm, the bottom panel refers to state-insensitive trapping obtained with a trap laser wavelength in the range of $623 - 630$ nm.

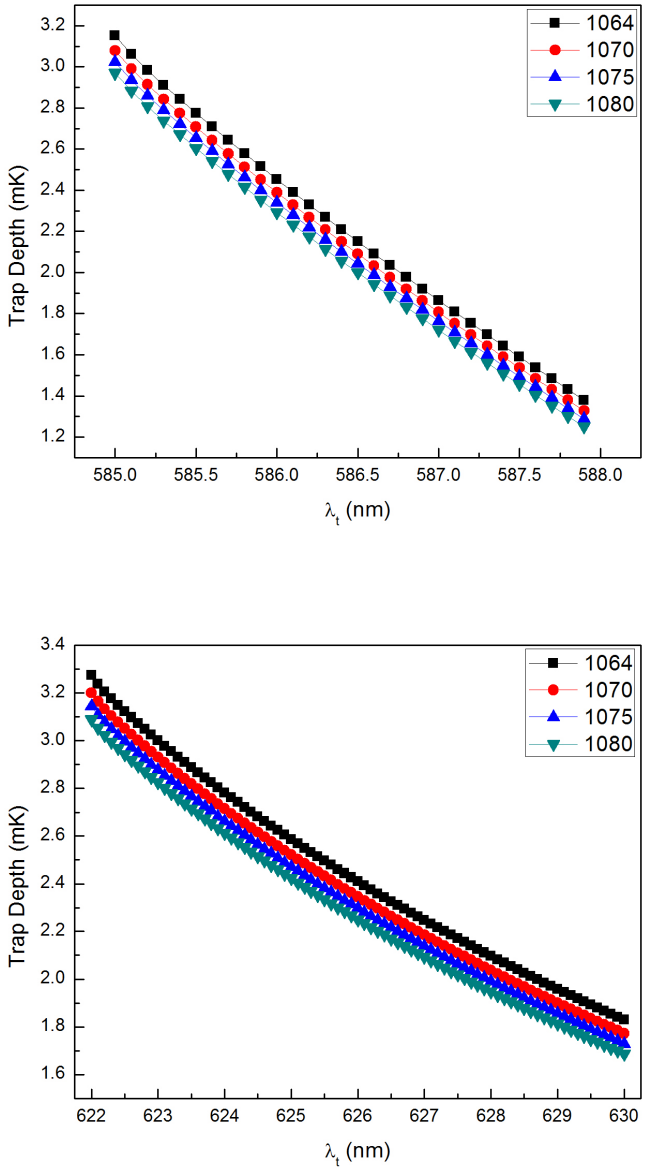

Figure 4.6: Variation of obtained trap depth with trapping laser wavelength for different control laser wavelengths such as 1064 nm, 1070 nm, 1075 nm and 1080 nm.

excited state degeneracy produced by the trapping light. As the figure 4.4 indicates the Zeeman sublevels of the excited state are split by an amount depending on the wavelength combinations of the lasers. Thus the each sublevel corresponds a different trap and control magic wavelength combination. This sets limits on the use of state-independent traps in conjunctions with other mechanisms, which may require efficient optical pumping. For instance, this is the case for optical molasses during the loading of a dipole trap from a magneto-optical trap. We thus investigated the splitting between excited state sublevels as a function of the experimental parameters leading to state-insensitive trapping. In particular, the conditions for the splitting between the sublevels to be less than -2Γ was examined, with Γ the atomic excited state linewidth, which is a typical detuning for optical molasses. The sublevels split further with increasing trap depth. Accordingly, to maintain the splitting between the sublevels below 2Γ, the trap depth should be kept under a certain value. To determine this specific value, the trap depth was evaluated as function of the magic trap wavelength for different control laser wavelengths for a fixed 2Γ splitting between the sublevels. The result of the calculation is plotted in figure 4.7. It follows that to be able to take advantage of simultaneous laser cooling and dipole trapping, the deepest trap achievable for the proposed laser combinations is 0.95 mK for a trap laser wavelength of 585.3 nm.

In addition, the dependence of the trapping wavelength on the the splitting between the Zeeman sublevels was investigated. The results are shown in figure 4.8, in which the data displayed points out that the actual value of the magic wavelength pairs affect the magnitude of the splitting between the sublevels. The lowest splittings occur at the magic wavelength pairs of $586.2 - 1064$ nm and $630 - 1064$ nm. As the reported data indicates, any deviation from these values results in an increase in the magnitude of the splitting. Considering the very different trap depth obtainable at these different wavelengths, the magic wavelength pair $586.2 - 1064$ nm is more favourable for state-independent trapping.

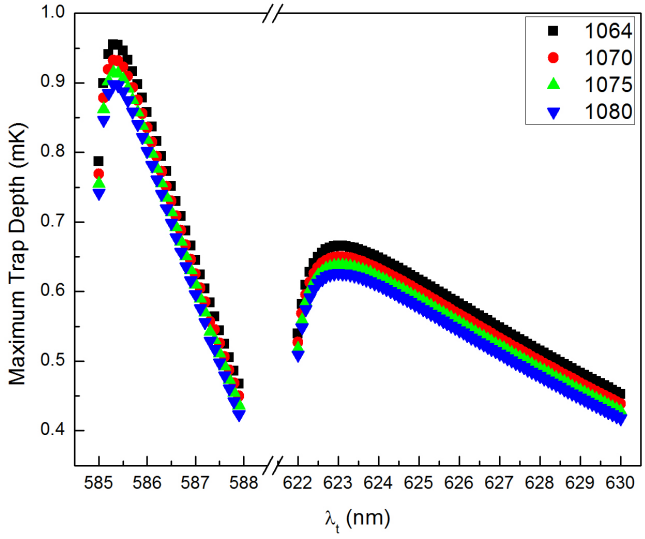

Figure 4.7: Trap depth versus wavelength of the trap lasers when the splitting between sublevels of the excited state equals to 2Γ.

4.5 Effects of variations in experimental parameters

Fluctuations in laser intensity or wavelength lead to a violation of the condition for state-insensitive trapping. The effect of these fuctuations is quantitatively investigated in this section. More specifically, we investigated the effect of intensity variations of the trap and control lasers on the AC Stark shift experienced by the ground and the excited states for the magic wavelength pair of $623.5 - 1064$ nm and a trap depth of 1 mK. The data displayed indicates that variations in the intensity ratios causes variations in the differential light shift. Different excited state Zeeman sublevels indeed experience different shifts induced by the variations in laser intensity. The differential AC Stark shift between the ground and the excited states of Caesium was calculated for $\pm 15\%$ variation in the intensity ratio of the trap and the control lasers, with results shown in figure 4.9. The data shown in the figure indicates that the different shift of the different Zeeman sublevels of the

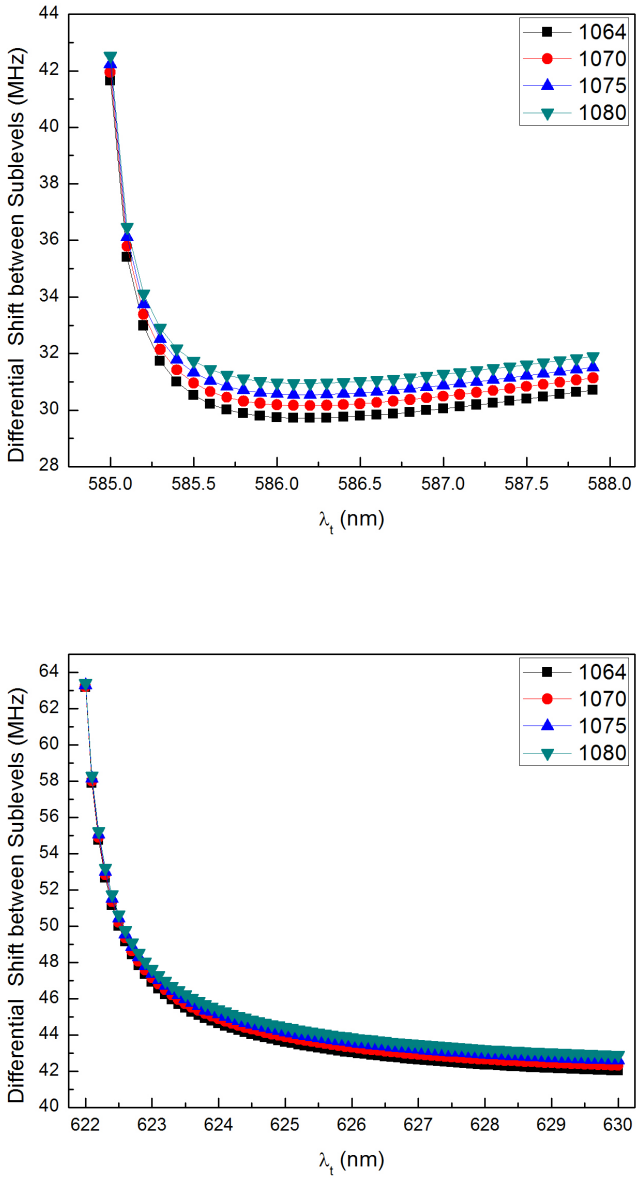

Figure 4.8: The effect of variations in the trap laser wavelength on the splittings between the Zeeman subleves of the $6P_{3/2}$ excites state for different control laser wavelengths of 1064 nm, 1070 nm, 1075 nm and 1080 nm.

excited state varies linearly with the intensity ratio. It also demonstrates that a variation in the relative intensities of lasers causes a variation in the magic wavelength of each Zeeman sublevel. As the intensity ratio deviates from the required value for a specific sublevel of the excited state, it approaches the required value of the intensity ratio for the next sublevel. Thus, despite state-insensitive trapping conditions for one sublevel is violated, it is maintained for the next sublevel. Consequently, intensity fluctuation of the lasers does not have a significant effect on bichromatic state-insensitive trapping of caesium atoms.

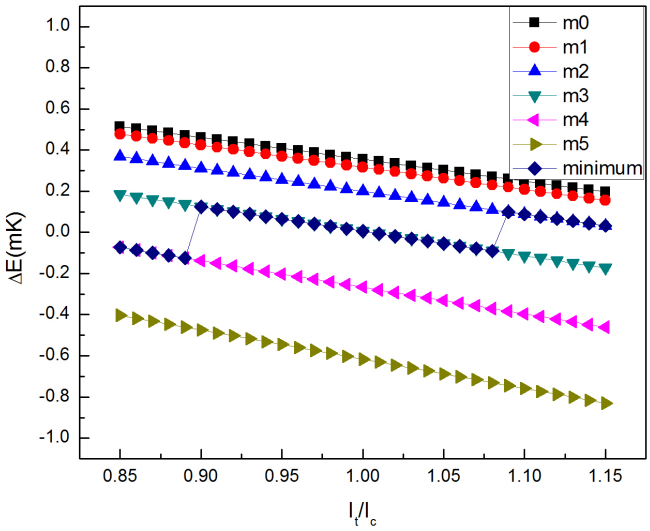

Figure 4.9: The differential AC Stark shift experienced by the excited and the ground state of the Caesium atoms in case of intensity variations around the value for state-independent trapping.

The other experimental parameter whose variations affect the condition of state-independent trapping is the wavelength of the two lasers. Such an effect was investigated by considering the variation of the wavelength from the required magic value. The differential AC Stark shift between the ground and the excited states of the caesium atom was evaluated for a variation of the trap laser wavelength up to a value $\Delta\lambda_t = 1.5$ nm while keeping the intensity

ratio fixed for the magic wavelength combination of $623.5-1064$ nm. Results of the calculations are presented in figure 4.10. The data reported indicates that as the trapping wavelength approaches the $8D_{3/2}$ transition at 621.7 nm the differential AC Stark shift increases significantly. Away from this transition, as the trap laser wavelength increases the differential AC Stark shift exhibits an oscillatory value around zero.

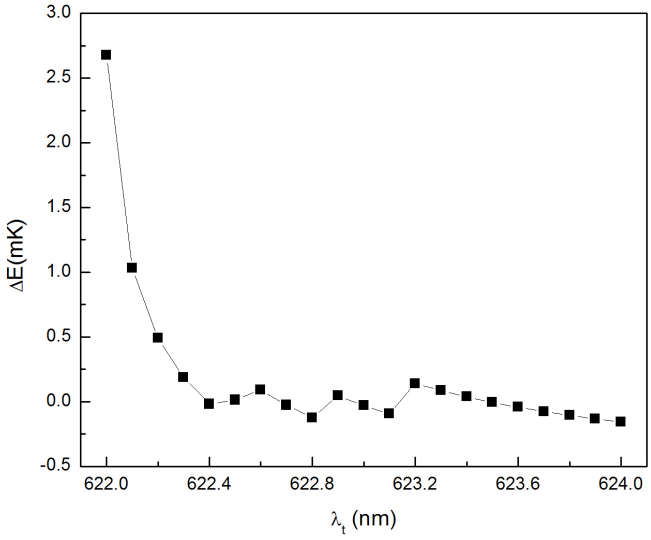

Figure 4.10: The differential AC Stark shift experienced by the excited and the ground state of the Caesium in case of fluctuations in the trap laser wavelength.

To realize the bichromatic trapping, the trap and control laser beams must be spatially overlapped. More specifically, focus positions of the two beams should be transversely overlapped and remain stable at this position. Thus, pointing instability of the laser beams is an important factor in bichromatic optical trapping. The error caused by beam pointing instability can be reduced by coupling the optical trapping beams to an optical fiber. However, in this way beam pointing instability problem is converted into intensity fluctuation. As shown in figure 4.9 state-insensitive trapping is preserved for $\pm 15\%$ intensity fluctuation of the trap and the control lasers.

4.6 Conclusion

In summary, bichromatic state-insensitive dipole trapping was proposed as a solution to overcome the problem of lack of sufficiently high power laser sources for free space monochromatic trapping of Caesium atoms. A number of magic wavelength combinations promising for experimental realizations were numerically identified. First, the magic wavelength sets of $931.8 - 1863.6$ nm and $927.5 - 2782.5$ nm were identified for the special cases of $2\lambda_{trap} = \lambda_{control}$ and $2\lambda_{trap} = \lambda_{control}$ for equal intensities, which can be achieved via second and third harmonic generation from a single laser source. Then, the magic wavelength pairs achievable by employing two commercially available high power lasers were determined. The appropriate wavelengths for the control laser were found to be 1064 nm, 1070 nm, 1075 nm and 1080 nm and the corresponding magic trap wavelength for all these control laser wavelengths were identified in the range of $585 - 588$ nm and $623 - 629$ nm. These magic wavelength combination are accessible by high power lasers; they can be achieved by using Nd:YAG or Ytterbium fiber lasers as control laser and red and orange raman fiber lasers as the trap laser.

Consequently, it was shown that the bichromatic trapping scheme significantly extends the range of possible magic wavelengths compared to monochromatic trapping scheme. It introduces a degree of tunability of the magic wavelength by varying the relative intensities of the two lasers. Therefore, limitations posed in the case of single frequency state-insensitive trapping on the wavelength and the power of the laser are overcome by the bichromatic trapping. In this respect, bichromatic state-insensitive trapping is more advantageous than the one achieved by a single laser scheme.

Chapter 5

Bichromatic State-Insensitive Trapping of Multispecies Mixtures of Cold Atoms: ^{133}Cs-^{87}Rb

The core of the results presented in this chapter was also published in M. M. Metbulut, F. Renzoni, *Bichromatic state-insensitive trapping cold of atomic ^{133}Cs-^{87}Rb mixtures*, Journal of Modern Optics 62.sup2 (2015): S67-S71.

5.1 Introduction

Research on multispecies mixtures of cold atoms has been attracting increasing attention over the last decade. Recent progress opened new research areas beyond the experiments with single species. Highlights of these studies include the exploration of phase transitions in optical lattices [70, 71], the demonstration of tuning of interatomic interaction between two species [72–75], the creation of molecules via photoassociation [76–78], sympathetic cooling of one species by another [79–81], the demonstration of quantum degenerate systems [82–84], precision metrology [85], quantum computation [77] and simulation [86].

The significance of optical dipole trapping as a standard tool for the creation and manipulation of ultracold atomic mixtures is undisputed. An optical trap creates a potential independent of hyperfine state and spin projection of an atom [14, 15], which is not possible with other trapping mechanisms. In addition, the use of far-off resonance laser light for trapping ensures low scattering rates so to achieve long coherence times [15, 30]. As explained in the previous chapter state-insensitive trapping plays an important role in experiments involving optical dipole trap Until present state-insensitive trapping of several single atomic species have been studied but the possibility of state-independent trapping of mixtures of different atomic species has remained unexplored. In this chapter dual-species state-insensitive trapping is theoretically investigated.

A mixture of caesium and rubidium atoms is considered here to investigate the possibility of their simultaneous state-insensitive trapping. Previously in chapters 2 and 4 both the monochromatic and bichromatic state-insensitive trapping of caesium atom were presented. It was shown that by using two independent laser fields it is possible to tune the magic wavelength of caesium atoms to an appropriate frequency range. By taking advantage of the tunability offered, we considered bichromatic trapping approach to investigate the existence of common magic wavelengths for the two atomic species.

5.2 Magic Wavelength Combinations

In this section, the AC Stark shifts of the ground and excited states of the transitions $6S_{1/2}(F = 4) \rightarrow 6P_{3/2}(F = 5)$ and $5S_{1/2}(F = 2) \rightarrow 5P_{3/2}(F = 3)$ of Caesium and Rubidium atoms are evaluated by using mathematica and following the same procedure described in section 2.5.2, including all the hyperfine levels and the corresponding Zeeman sublevels. In our calculations, contributions from excited states up to 11S, 12P and 12D for Caesium and 10S, 10P and 8D for Rubidium were taken into account respectively. The input data for transition wavelengths and Einstein coefficients are taken from

the references [34, 35, 87]. Linear polarization, beam waist of 10 μm for both trap and control lasers and fixed power of 2 W for the control laser were considered. In this way, the intensity of the trap laser and the wavelengths of both lasers were used as variables to tune the magic wavelength combinations of the two atoms to a common value.

5.2.1 Magic Wavelength of Rubidium

The magic wavelength for Caesium was identified in section 2.5.2 for a monochromatic trapping scheme. Therefore, in this section our calculations start with the determination of the magic wavelength for Rubidium. The light shift of the D_2 line transition of the Rubidium atom is calculated in the presence of a single laser field, with the result plotted in figure 5.1. As the data displayed in 5.1 indicates, the magic wavelength of Rubidium was determined to be 789.97 nm.

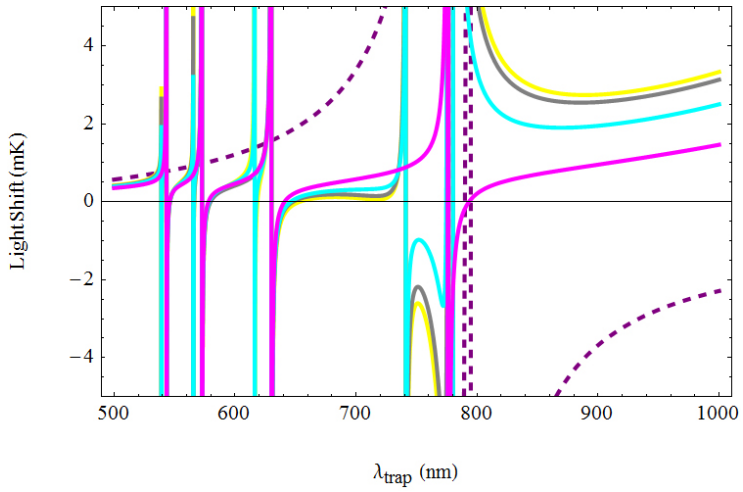

Figure 5.1: AC Stark shift for the $F_g = 2 \rightarrow F_e = 3$ transition of a ^{87}Rb as a function of the trap laser wavelength for laser power of 2 W and a beam waists of 10 μm. The purple dashed line refers to the ground state $5S_{1/2}$, yellow, gray, cyan and magenta lines are the excited state $5P_{3/2}$ with $m = 0, \pm 1, \pm 2, \pm 3$ Zeeman sublevels respectively.

5.2.2 Magic Wavelength Combinations of Rubidium and Caesium

The calculations proceed with the evaluation of the light shifts of the Caesium and Rubidium atoms separately as functions of the trap laser wavelength in the presence of two laser fields. The numerical calculations demonstrate that six common magic wavelength combinations are appropriate for the simultaneous state-insensitive trapping of the two atoms. These combinations are listed in table 5.1 together with the required intensity ratios of the lasers and the corresponding trap depths. Small uncertainties in the input parameters for the differential AC Stark shift calculations resulted in small uncertainty in values of the $6S_{1/2}(F = 4) \rightarrow 6P_{3/2}(F = 5)$ and $5S_{1/2}(F = 2) \rightarrow 5P_{3/2}(F = 3)$ transitions of Caesium and Rubidium atoms. Subsequently, negligibly small uncertainty ($< 1\%$) was observed in the determined magic trapping wavelengths as shown in table 5.1. Due to the different polarizability of the Caesium and Rubidium atoms, the same experimental parameters leads to different trap depths for the two species. The ratio of the trap depths of Caesium and Rubidium atoms increases from ≈2 to ≈2.8 as the magic trap wavelength increases from 868.8 nm to 936 nm. It is thus not possible to maintain simultaneous state-insensitive trapping with equal trap depth of the Rubidium and Caesium atom.

λ_t (nm)	λ_c (nm)	I_t/I_c	Rb U (mK)	Cs U (mK)
$868.80 \pm 1 \times 10^{-3}$	10060	0.240	2.04	4.14
$868.94 \pm 1 \times 10^{-3}$	10600	0.239	2.03	4.08
$931.00 \pm 2 \times 10^{-3}$	2038.8	0.939	3.89	10.17
$932.90 \pm 1 \times 10^{-3}$	1843.5	1.408	5.31	14.18
$934.00 \pm 1 \times 10^{-3}$	1742.4	1.999	7.08	19.25
$936.00 \pm 5 \times 10^{-3}$	1580.9	7.832	24.36	68.95

Table 5.1: Magic wavelength combinations and corresponding required intensity ratios for a Cs-Rb mixture. The trap depths for Cs and Rb atoms are also reported, for a control laser power of 2 W and a laser beam waist of 10 μm for both lasers.

The light shifts of both atomic species are plotted in figure 5.2 as functions of the trap laser wavelength for all the six identified magic wavelength combinations, with the intensity ratio and the control laser wavelength in accordance with the values listed in Table 5.1. The displayed data evidences that at the magic trapping wavelength the differential light shifts for both atomic species is zero. As shown in both figures, the Zeeman sublevels of the ground state of both atoms remain degenerate, as expected for a linear polarization of the laser fields, whereas they are splitted for the excited state.

Out of the six identified magic wavelength combinations, the wavelength pair of $\lambda_t = 868.94 - \lambda_c = 10600$ nm is appealing for practical realizations given current laser technology. This wavelength pair can be achieved by employing a diode and CO_2 laser for the trap and control fields, respectively.

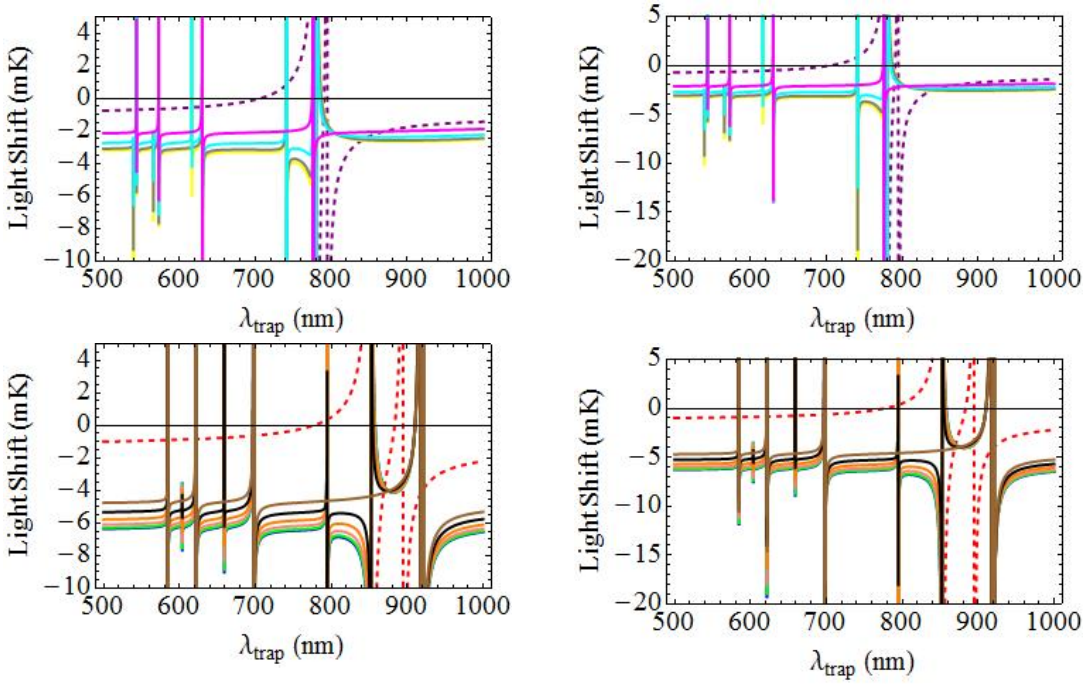

(a) $\lambda_t = 868.6\text{nm-}\lambda_c = 10060\text{nm}$

(b) $\lambda_t = 868.94\text{nm-}\lambda_c = 10600\text{nm}$

Figure 5.2: The top panel shows the AC Stark shift for ^{87}Rb as a function of the trapping wavelength. The purple dashed line is the ground state $5S_{1/2}$, yellow, gray, cyan and magenta lines are the excited state $5P_{3/2}$ with $m = 0, \pm1, \pm2, \pm3$ Zeeman sublevels respectively. The bottom panel shows AC Stark shift for ^{133}Cs as a function of the trapping wavelength. The red dashed line refers to the ground state $6S_{1/2}$, blue, green, pink, orange, black and brown lines are the excited state $6P_{3/2}$ of Caesium with $m = 0, \pm1, \pm2, \pm3, \pm4, \pm5$ Zeeman sublevels respectively.

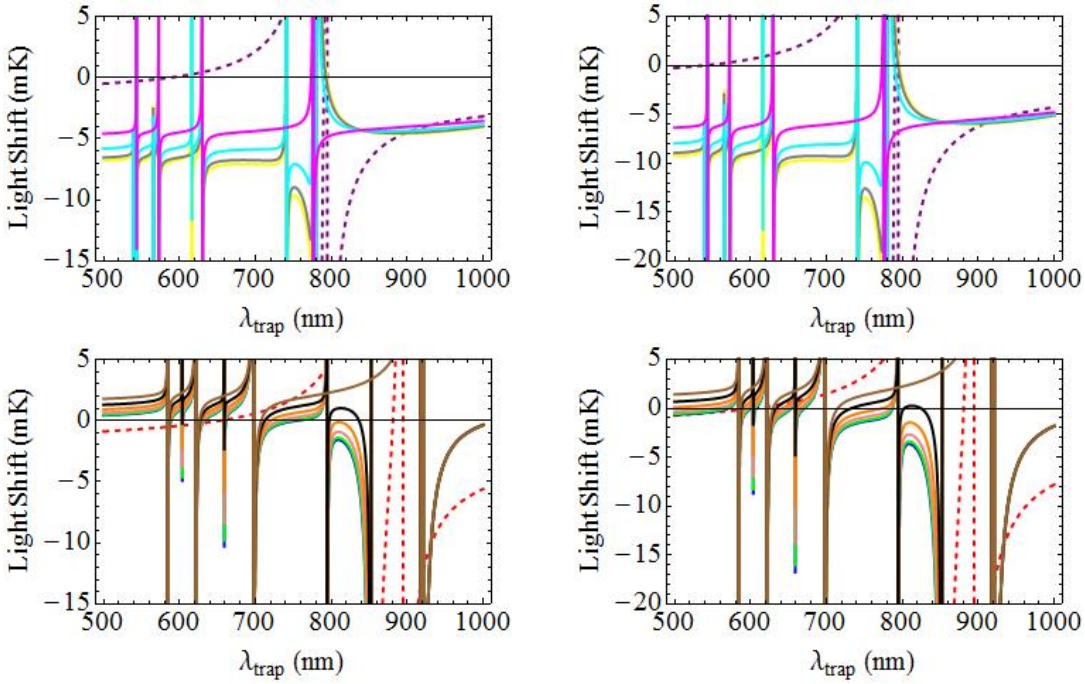

(c) $\lambda_t = 931\text{nm-}\lambda_c = 2038.8\text{nm}$ **(d)** $\lambda_t = 932.9\text{nm-}\lambda_c = 1843.5\text{nm}$

Figure 5.2: The top panel shows the AC Stark shift for ^{87}Rb as a function of the trapping wavelength. The purple dashed line is the ground state $5S_{1/2}$, yellow, gray, cyan and magenta lines are the excited state $5P_{3/2}$ with $m = 0, \pm1, \pm2, \pm3$ Zeeman sublevels respectively. The bottom panel shows AC Stark shift for ^{133}Cs as a function of the trapping wavelength. The red dashed line refers to the ground state $6S_{1/2}$, blue, green, pink, orange, black and brown lines are the excited state $6P_{3/2}$ of Caesium with $m = 0, \pm1, \pm2, \pm3, \pm4, \pm5$ Zeeman sublevels respectively.

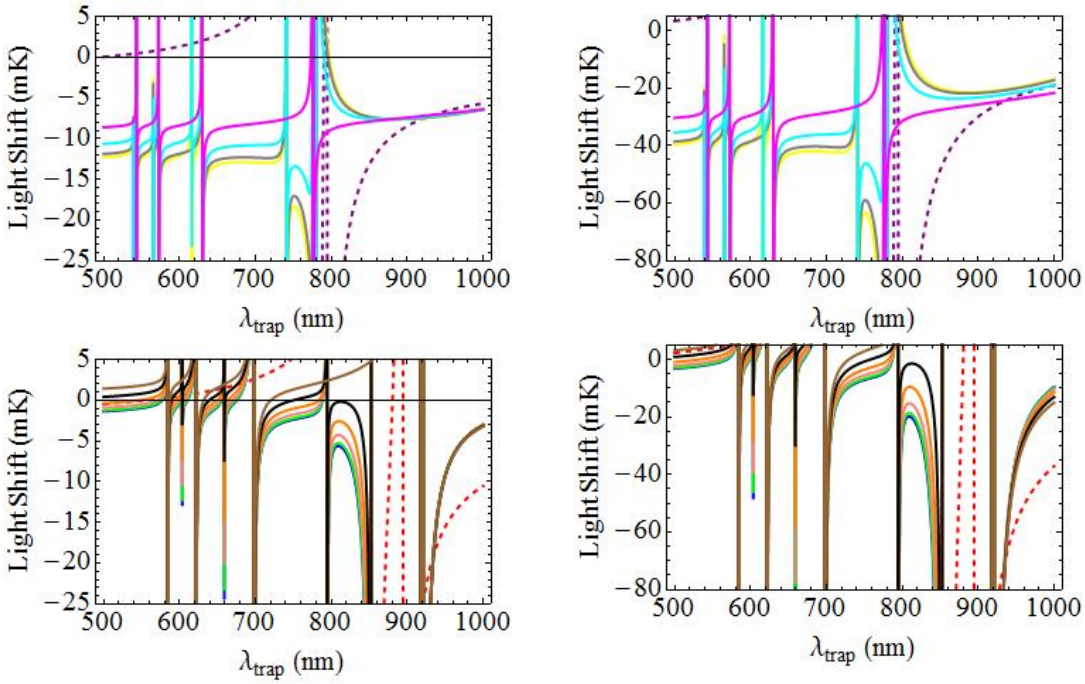

(e) $\lambda_t = 934\text{nm-}\lambda_c = 1742.4\text{nm}$

(f) $\lambda_t = 936\text{nm-}\lambda_c = 1580.9\text{nm}$

Figure 5.2: The top panel shows the AC Stark shift for ^{87}Rb as a function of the trapping wavelength. The purple dashed line is the ground state $5S_{1/2}$, yellow, gray, cyan and magenta lines are the excited state $5P_{3/2}$ with $m = 0, \pm1, \pm2, \pm3$ Zeeman sublevels respectively. The bottom panel shows AC Stark shift for ^{133}Cs as a function of the trapping wavelength. The red dashed line refers to the ground state $6S_{1/2}$, blue, green, pink, orange, black and brown lines are the excited state $6P_{3/2}$ of Caesium with $m = 0, \pm1, \pm2, \pm3, \pm4, \pm5$ Zeeman sublevels respectively.

5.3 Effect of variations in experimental parameters

The effect of variations in experimental parameters on state-insensitive trapping of the Cs-Rb mixture was also analyzed. First, we examine how a variation in wavelength of the trapping laser affects the possibility of simultaneous state-independent trapping of the two atomic species. Variations in trap laser wavelength for all of the six identified magic wavelength combinations were considered. The trap/control laser intensity ratio required for state-independent trapping of each individual species, Caesium and Rubidium, as a function of the trap laser wavelength was evaluated and results were displayed in figure 5.3. The data demonstrates that a variation in trap laser wavelength cannot be compensated by tuning the relative intensities of the trap and control lasers. In fact, deviation from the required trap laser wavelength for dual-species state-insensitive trapping, corresponds to different intensity ratio for the two atoms, and the discrepancy in the required value for the two species increases with the variation in the trapping wavelength. The data presented in figure 5.3 shows that state-insensitive trapping of Caesium atoms is more sensitive to the variation in the trapping wavelength compared to Rubidium atoms.

The difference between the trap/control intensity ratio required to produce state-independent trapping of Rubidium and Caesium are listed in table 5.2 for the cases of 0.01, 0.1 and 0.5 nm variation in wavelength of the trap laser. The presented data indicates that a small variation in the trap laser wavelength has a substantial effect on the possibility of dual-species state-independent trapping. The stability requirements to preserve the conditions for the state-insensitive trapping of the mixture are quantified in table 5.2. The data show that a 0.01 nm variation in the trapping laser wavelength corresponds to a negligible change in the required intensity ratio of the lasers for the magic wavelength combination of 868.94 nm-10.6 μm. This evidences that simultaneous state-independent trapping will be maintained for wave-

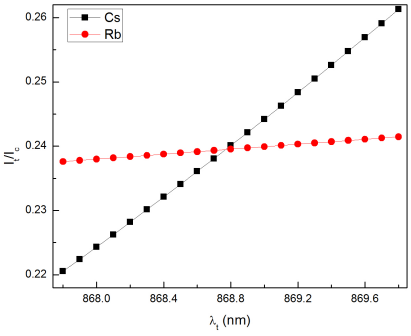

(a) $\lambda_t = 868.6\text{nm-}\lambda_c = 10060\text{nm}$

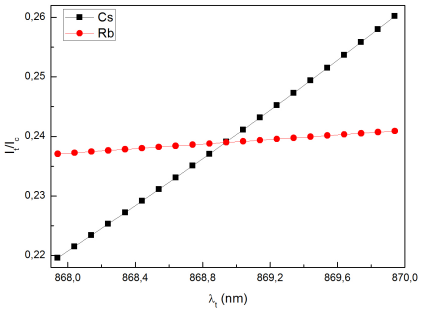

(b) $\lambda_t = 868.94\text{nm-}\lambda_c = 10600\text{nm}$

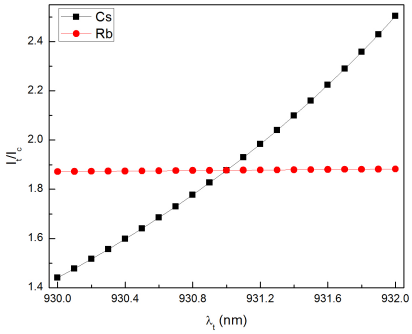

(c) $\lambda_t = 931\text{nm-}\lambda_c = 2038.8\text{nm}$

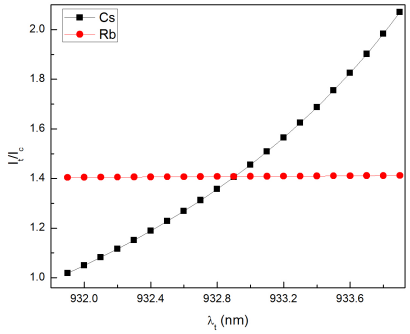

(d) $\lambda_t = 932.9\text{nm-}\lambda_c = 1843.5\text{nm}$

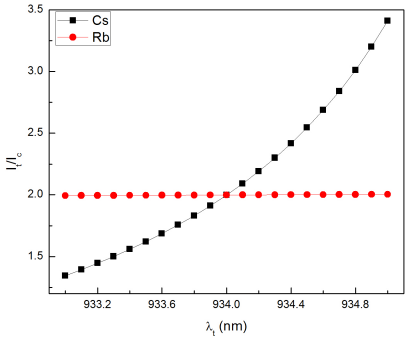

(e) $\lambda_t = 934\text{nm-}\lambda_c = 1742.4\text{nm}$

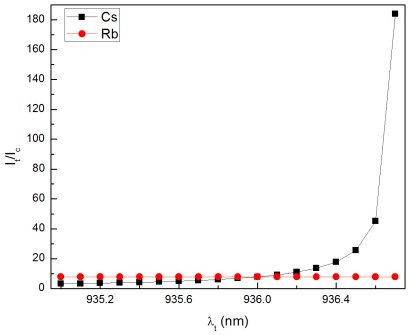

(f) $\lambda_t = 936\text{nm-}\lambda_c = 1580.9\text{nm}$

Figure 5.3: Effect of trap wavelength fluctuations on the required intensity ratio of trap and control lasers for Cs and Rb.

length variations below ±0.01 nm.

$\lambda_t - \lambda_c$ (nm)	$\Delta I_t/I_c$ for $\Delta\lambda_t = 0.01$ nm	$\Delta I_t/I_c$ for $\Delta\lambda_t = 0.1$ nm	$\Delta I_t/I_c$ for $\Delta\lambda_t = 0.5$ nm
$868.8 - 10060$	3.875×10^{-4}	6.303×10^{-4}	8.430×10^{-3}
$868.94 - 10600$	1.855×10^{-4}	1.734×10^{-3}	8.870×10^{-3}
$931 - 2038.8$	2.540×10^{-3}	5.013×10^{-2}	0.234
$932.9 - 1843.5$	7.785×10^{-3}	5.029×10^{-2}	0.217
$934 - 1742.4$	9.355×10^{-3}	8.628×10^{-2}	0.376
$936 - 1580.9$	1.062×10^{-1}	9.847×10^{-1}	3.334

Table 5.2: Difference between the required trap/control lasers intensity ratio of the Caesium and Rubidium atoms for maintaining state-insensitive trapping in case of $\lambda_t = 0.01, 0.1$ and 0.5 nm variation in trap laser wavelength.

Next, the effect of variations in another important parameter, the laser intensity is investigated. By considering intensity variations of the trap and control lasers, the deviations of the corresponding magic trap laser wavelengths of the two atomic species were analyzed. The effect of intensity variations in trap/control laser intensity ratio is illustrated in figure 5.4 for all the identified magic wavelength combinations. The data indicates that a variation in the intensity ratio leads to different magic wavelength for the two atomic species, with the magic trapping wavelength of the Rb species showing greater deviation than that of the Cs atoms. This effect was investigated considering the cases of 0.1% and 0.5% variation in the trap/control laser intensity ratio for all the identified magic wavelength combinations. The corresponding magic trap laser wavelengths of the Caesium and Rubidium atoms are listed in table 5.3. The data given demonstrate that larger intensity variations results in a larger deviation of the Rubidium and Caesium magic wavelengths from their common magic wavelength.

We notice that the differential deviation between the magic wavelengths of the two atoms is less than 1 nm for 0.1% variation in the trap/control lasers intensity ratio for all identified magic wavelength combinations as shown in

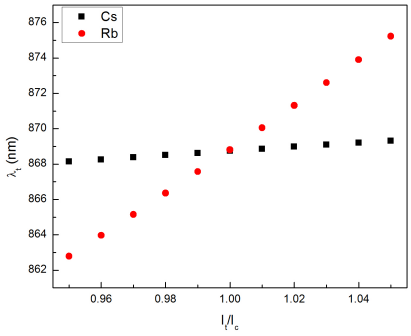

(a) $\lambda_t = 868.6\text{nm-}\lambda_c = 10060\text{nm}$

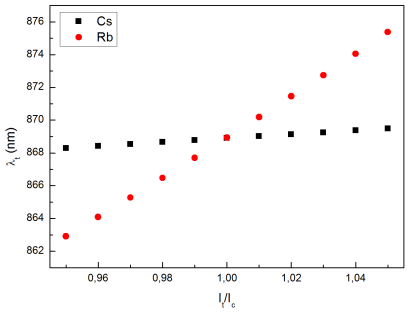

(b) $\lambda_t = 868.94\text{nm-}\lambda_c = 10600\text{nm}$

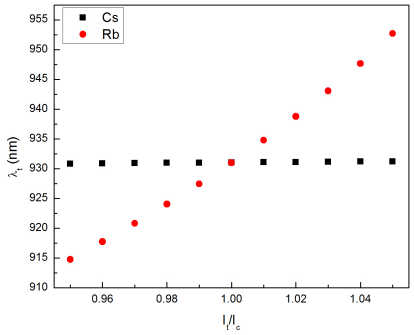

(c) $\lambda_t = 931\text{nm-}\lambda_c = 2038.8\text{nm}$

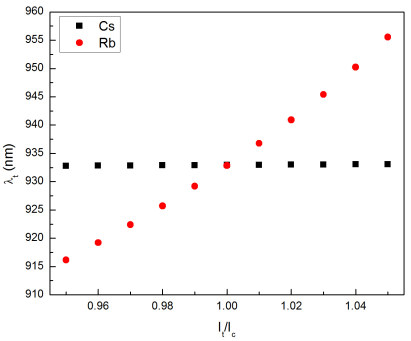

(d) $\lambda_t = 932.9\text{nm-}\lambda_c = 1843.5\text{nm}$

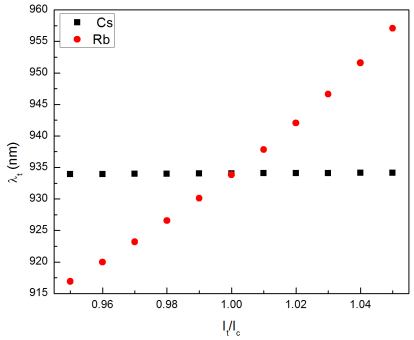

(e) $\lambda_t = 934\text{nm-}\lambda_c = 1742.4\text{nm}$

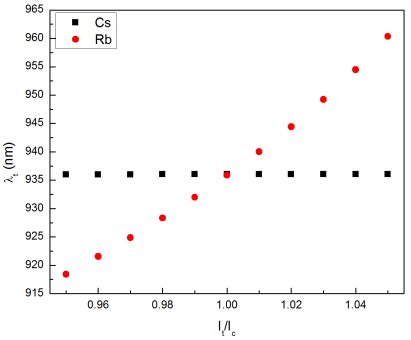

(f) $\lambda_t = 936\text{nm-}\lambda_c = 1580.9\text{nm}$

Figure 5.4: Effect of intensity ratio fluctuations on the required trap laser wavelength Cs and Rb.

$\lambda_t - \lambda_c$ (nm)	λ_t (nm) of Cs−Rb for $\Delta I_t/I_c =$ 0.1%	λ_t (nm) of Cs−Rb for $\Delta I_t/I_c =$ 0.5%
868.8 − 10060	868.73-868.67	868.68-868.18
868.94−10600	868.89-868.80	868.84-868.30
931 − 2038.8	931.02-930.64	931.01-929.20
932.9 − 1843.5	932.94-932.52	932.92-931.05
934 − 1742.4	934.03-933.62	934.02-932.10
936 − 1580.9	936.04-935.06	936.03-934.03

Table 5.3: List of common magic wavelength combinations and the deviated magic trap laser wavelengths of Cs and Rb for 0.1 and 0.5% variation in intensity ratios from the value leading to dual-species state-independent trapping. The data refer to a control laser power of 2 W and laser beam waists of 10 μm for both lasers.

table 5.3. Indeed, 0.1% variation in the laser intensity ratio for the magic wavelength pair of 868.94 nm −10.6 μm leads to 0.1 nm shift between the corresponding magic wavelengths of the two atoms. Hence, for a typical linewidth of 1 nm for the trap laser, we can assume that intensity variations below 0.1% will not affect the simultaneous state-insensitive trapping of the two atomic species.

5.4 Conclusion

In this chapter, the possibility of simultaneous state-independent trapping of two different atomic species was explored. We considered specifically a Caesium-Rubidium mixture as case study. The magic wavelengths of the Caesium and Rubidium atoms are different, 935.6 nm and 789.9 nm respectively, thus single-frequency simultaneous state-insensitive trapping is not possible. We identified bichromatic trapping as a viable approach to tune the two magic wavelengths to a common value. Correspondingly, we presented several common magic wavelength combinations appropriate for simultaneous state-insensitive trapping of the two atomic species. In particular, 868.94 nm-10.6 μm trap/control laser wavelength pair is marked as the

most promising for experimental realization considering the frequency range of the currently available lasers.

Chapter 6

Bichromatic State-Insensitive Trapping of Multispecies Mixtures of Cold Atoms: ^{133}Cs-^{6}Li

6.1 Introduction

Remarkable developments in experiments with ultracold atoms, in particular the observation of degenerate Fermi gases and Bose-Einstein condensate, have extended the focus of research to mixtures of atoms. The mixture of different atomic species with different mass, interactions, trapping properties and in particular with different quantum statistics opened a door to broad range of studies such as sympathetic cooling of one species by another [88, 89], study of BCS-BEC crossover [90, 91], Efimov states [92–94], interspecies Feshbach resonances [73, 95] and superfluidity [96].

In light of these developments, the possibility of simultaneous state-insensitive trapping of a Fermi and a Bose gas is discussed in this chapter. Specifically, Fermi-Bose mixture of ^{133}Cs-^{6}Li is considered as it is an ap-

pealing mixture in terms of experimental implementation for several reasons. First, the mixture of ^{133}Cs-^{6}Li has an extreme mass ratio of $m_{Cs}/m_{Li} = 22$ providing universal scaling factor of 4.88, instead of 22.7 for a system with equal masses [97], and thereby it provides excellent conditions to observe Efimov resonances. Moreover, the permanent electric dipole moment of 5.5 Debye of LiCs molecules is the largest among combinations of alkalis [98], which is suitable to study dipolar effects. The possibility of sympathetic cooling of one atomic specie by the other one is another factor making this mixture attractive. Caesium atoms can be cooled to very low temperature via sub-Doppler cooling while it is difficult for Lithium atoms. The unresolved hyperfine splittings of the $2P_{3/2}$ state limits the Doppler temperature of the Lithium to be ≈ 300 μK [99], however with use of narrow linewidth cooling technique temperatures as low as 59 μK was reported [99]. In the narrow linewidth cooling technique, the atoms are transferred form the $2S_{1/2} \rightarrow 2P_{3/2}$ transition to the narrow uv transition of $2S_{1/2} \rightarrow 3P_{3/2}$ to attain second stage cooling in MOT. By sympathetic cooling of lithium with caesium atom further reduction in the temperature of lithium atom can be achieved. The AC stark shift produced by the trapping light has a substantial effect on the narrow linewidth of the cooling transition of lithium. In this regard, light shifts in the energy levels of both lithium and caesium atom become considerably important, which highlights the important role played by the state-insensitive trapping. Although there are works devoted to identify the magic wavelengths of both species, previous study related to the existence of a common magic wavelength for the two species has not been reported. We propose the bichromatic trapping approach to investigate the possibility of common magic wavelength for dual-species state-insensitive trapping of ^{133}Cs-^{6}Li mixtures.

6.2 Magic Wavelength Combinations

In this section, the light shifts of the caesium and lithium atoms were evaluated for the transition of relevance to the two stage laser cooling of lithium atoms in magneto-optical trap. The simultaneous elimination of the differential AC stark shift of the $2S_{1/2} \rightarrow 3P_{3/2}$ transition for lithium and $6S_{1/2} \rightarrow 6P_{3/2}$ transition for caesium allows to cool the atoms more efficiently during loading from a magneto-optical trap into an optical dipole trap.

6.2.1 Magic Wavelengths of Lithium

We start the investigation of state-independent trapping with $2S_{1/2} \rightarrow 2P_{3/2}$ and $2S_{1/2} \rightarrow 3P_{3/2}$ transitions of Lithium by considering a single frequency scheme. The AC Stark shift of the ground state $2S_{1/2}(F = 3/2)$ and the excited states $2P_{3/2}(F = 5/2)$ and $3P_{3/2}(F = 5/2)$ are evaluated separately as functions of laser wavelength. All calculations are carried out for linear polarization of the laser by taking into account contributions from the excited states up to 8S, 12P and 9D. The results of the calculation for the D_2 line transition are displayed in figures 6.1, with the magic wavelengths determined as 862.46 nm and 840.95 nm for the $m = 1/2$ and $m = 3/2$ Zeeman sublevels respectively.

The light shift of the ground and the excited states of the uv MOT transition is plotted in figure 6.2 and the magic wavelengths identified in range of $200 - 2000$ nm are listed in table 6.1. As reported by the data in table 6.1, the magic wavelengths of the Lithium and Cesium are very different. This indicates that simultaneous state-insensitive trapping of these species cannot be achieved by a single laser frequency. Therefore, bichromatic trapping approach is proposed to investigate the possible common magic wavelength combinations of the two species.

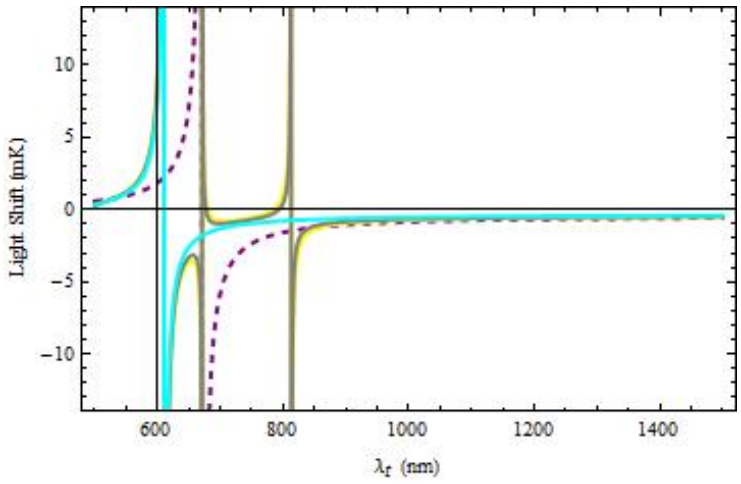

Figure 6.1: AC Stark shift for the $2S_{1/2}(F_g = 3/2) \rightarrow 2P_{3/2}(F_e = 5/2)$ transition of ^{6}Li as a function of trap laser wavelength for laser power of 2 W and beam waists of 10 μm. Purple dashed line is the ground state $2S_{1/2}$, yellow, gray and cyan lines are the excited state $2P_{3/2}$ with $m = \pm 1/2, \pm 3/2, \pm 5/2$ Zeeman sublevels respectively.

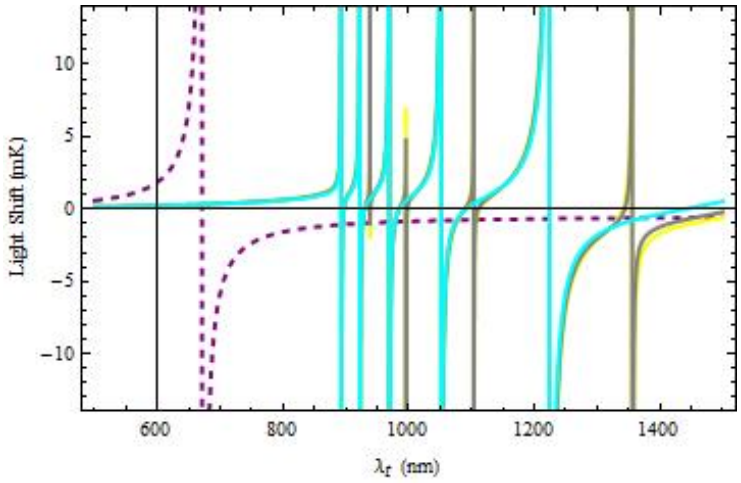

Figure 6.2: AC Stark shift for the $2S_{1/2}(F_g = 3/2) \rightarrow 3P_{3/2}(F_e = 5/2)$ transition of ^{6}Li as a function of the trap laser wavelength for laser power of 2 W and beam waists of 10 μm. Purple dashed line is the ground state $2S_{1/2}$, yellow, gray and cyan lines are the excited state $3P_{3/2}$ with $m = \pm 1/2, \pm 3/2, \pm 5/2$ Zeeman sublevels respectively.

λ_t (nm) for $m = 1/2$	λ_t (nm) for $m = 3/2$	λ_t (nm) for $m = 5/2$
894.797	894.731	894.589
926.524	926.433	926.231
978.638	978.429	977.956
1077.63	1077.19	1076.11
1107.87	1106.44	1371.54
1334.09	1336.8	
1500.9	1454.98	

Table 6.1: List of magic wavelengths of Lithium uv MOT transition.

6.2.2 Magic Wavelength Combinations of Lithium and Caesium

In presence of two laser fields, calculations for the light shift of the uv $2S_{1/2}$ ($F_g = 3/2$)→$3P_{3/2}$ ($F_e = 5/2$) transition of Lithium and $6S_{1/2}(F_g = 4) \rightarrow 6P_{3/2}(F_e = 5)$ transition of Caesium are presented separately as a function of trapping laser wavelength. All the calculations were performed for the linear polarization and 10 μm beam waists of both lasers, and fixed 2 W power of the control laser. Thus, intensity of the trapping laser and the frequency of the lasers are kept as variable parameters to tune the magic wavelength. Contributions from the couplings to states up to 8S, 12P, 9D and 11S, 12P, 9D were taken into account for Lithium and Caesium respectively.

For an appropriate choice of parameters, bichromatic trapping yielded ten common magic wavelength combinations for the two species, which are listed in table 6.2 with the required intensity ratio of the trap and control lasers and corresponding trap depths. As shown in the reported data, Lithium and Caesium atoms have different trap depths for the same experimental parameters due to different polarizabilities. The ratio of the trap depths of the Lithium and Caesium ranges from ≈ 0.7 to 4. It thus allows to choose one specie to have a larger trap depth than the other one. Although the magic wavelength combination of $\lambda_t = 701.4 - \lambda_c = 1063$ nm gives trap depth ratio of $U_{Li}/U_{Cs} = 0.97 \approx 1$, it is not possible the achieve simultaneous

state-insensitive trapping with exactly equal trap depths for both species.

Among these ten combinations, three of the wavelength sets are promising in terms of experimental realizations considering present laser technology. The combinations of $\lambda_c = 1064 - \lambda_t = 700.7$ nm, $\lambda_c = 1070 - \lambda_t = 814.8$ and $\lambda_c = 1075 - \lambda_t = 846.7$ can be implemented by employing a Nd:YAG or an ytterbium fiber lasers as control laser and a diode laser as trap laser. Uncertainties of these magic wavelengths resulting from the input parameters of the calculation were less than 1 nm as listed in table 6.2. Considering that linewidth of dipole trap lasers is typically ≈ 1 nm, these uncertainties do not have a effect on experimental realization of simultaneous state-insensitive trapping.

The light shifts of both Lithium and Caesium are plotted in figure 6.3 as functions of the trap laser wavelength, for all the magic wavelength combinations listed in table 6.2 in accordance with the given parameters. The data presented reveals that at the magic trapping wavelength the differential light shifts of both atomic species vanishes. As expected for the linear polarization of the laser fields, the Zeeman sublevels of the excited state are split in all displayed figures while they remain degenerate for the ground state.

λ_t (nm)	λ_c (nm)	I_t/I_c	Li U (mK)	Cs U (mK)
700.7 ± 0.546	1064	0.270	2.30	2.75
701.4 ± 0.561	1063	0.322	2.56	2.65
701.8 ± 0.172	1286	0.282	2.18	1.43
702.9 ± 0.185	1280.3	0.337	2.42	1.33
794.2 ± 0.547	1067.3	0.428	1.48	0.65
800.1 ± 0.248	974.8	0.456	1.61	2.37
814.8 ± 0.167	1070	0.271	1.17	0.69
846.7 ± 0.180	1075	0.040	0.82	0.92
1268.1 ± 0.190	711.4	1.735	5.37	1.32
1284.2 ± 0.290	702.1	3.350	7.56	4.69

Table 6.2: List of magic wavelengths of Caesium D2 line and Lithium uv MOT transition with required intensity ratio of trap and control lasers and the corrresponding trap depths.

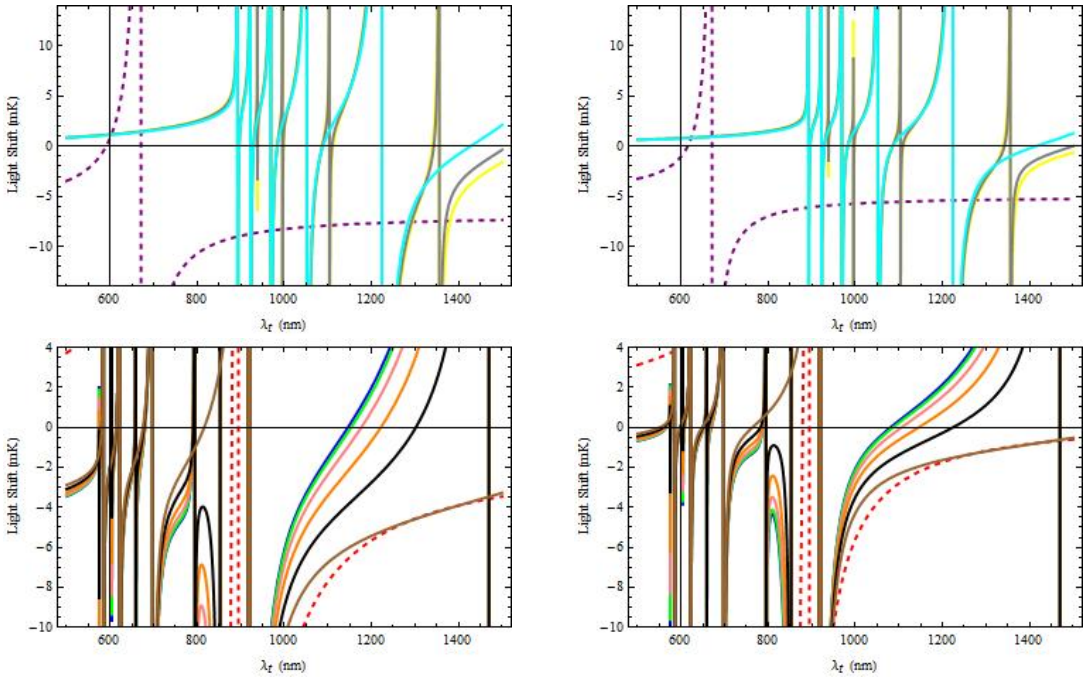

(a) $\lambda_t = 1284.2\text{nm-}\lambda_c = 702.1\text{nm}$ **(b)** $\lambda_t = 1268.1\text{nm-}\lambda_c = 711.4\text{nm}$

Figure 6.3: The top panel shows the AC Stark shift for ^{6}Li as a function of the trap laser wavelength where the purple dashed line is the ground state $2S_{1/2}$, yellow, gray and cyan lines are the excited state $3P_{3/2}$ of Lithium with $m = \pm 1/2, \pm 3/2, \pm 5/2$ Zeeman sublevels respectively. The bottom panel shows the AC Stark shift for ^{133}Cs as a function of trap laser wavelength where the red dashed line refers to the ground state $6S_{1/2}$, blue, green, pink, orange, black and brown lines refer to the excited state $6P_{3/2}$ of Caesium with $m = 0, \pm 1, \pm 2, \pm 3, \pm 4, \pm 5$ Zeeman sublevels respectively.

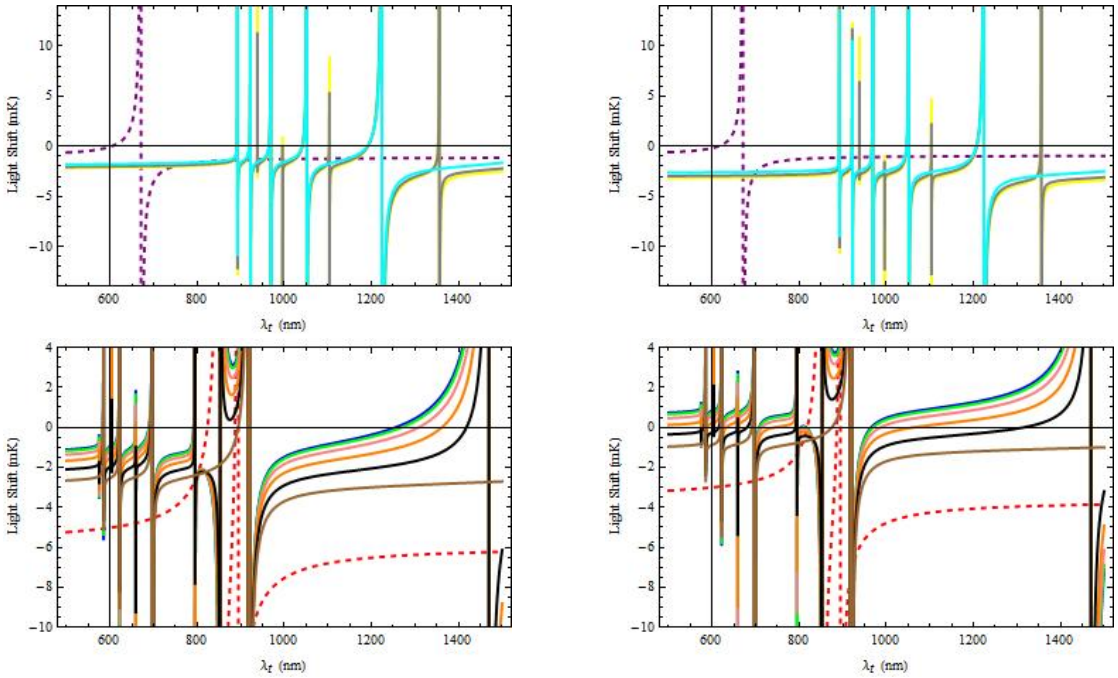

(c) $\lambda_t = 800.1\text{nm-}\lambda_c = 974.8\text{nm}$ **(d)** $\lambda_t = 701.4\text{nm-}\lambda_c = 1063\text{nm}$

Figure 6.3: The top panel shows the AC Stark shift for ^{6}Li as a function of the trap laser wavelength where the purple dashed line is the ground state $2S_{1/2}$, yellow, gray and cyan lines are the excited state $3P_{3/2}$ of Lithium with $m = \pm 1/2, \pm 3/2, \pm 5/2$ Zeeman sublevels respectively. The bottom panel shows the AC Stark shift for ^{133}Cs as a function of trap laser wavelength where the red dashed line refers to the ground state $6S_{1/2}$, blue, green, pink, orange, black and brown lines refer to the excited state $6P_{3/2}$ of Caesium with $m = 0, \pm 1, \pm 2, \pm 3, \pm 4, \pm 5$ Zeeman sublevels respectively.

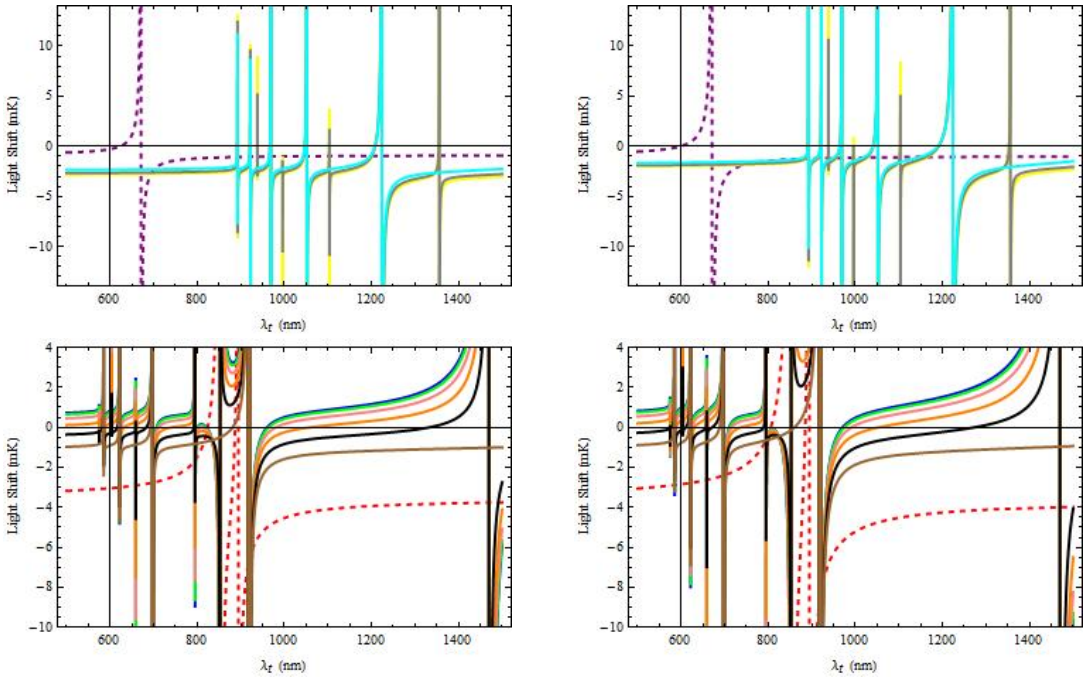

(e) $\lambda_t = 700.7$nm-$\lambda_c = 1064$nm **(f)** $\lambda_t = 794.2$nm-$\lambda_c = 1067.3$nm

Figure 6.3: The top panel shows the AC Stark shift for ^{6}Li as a function of the trap laser wavelength where the purple dashed line is the ground state $2S_{1/2}$, yellow, gray and cyan lines are the excited state $3P_{3/2}$ of Lithium with $m = \pm 1/2, \pm 3/2, \pm 5/2$ Zeeman sublevels respectively. The bottom panel shows the AC Stark shift for ^{133}Cs as a function of trap laser wavelength where the red dashed line refers to the ground state $6S_{1/2}$, blue, green, pink, orange, black and brown lines refer to the excited state $6P_{3/2}$ of Caesium with $m = 0, \pm 1, \pm 2, \pm 3, \pm 4, \pm 5$ Zeeman sublevels respectively.

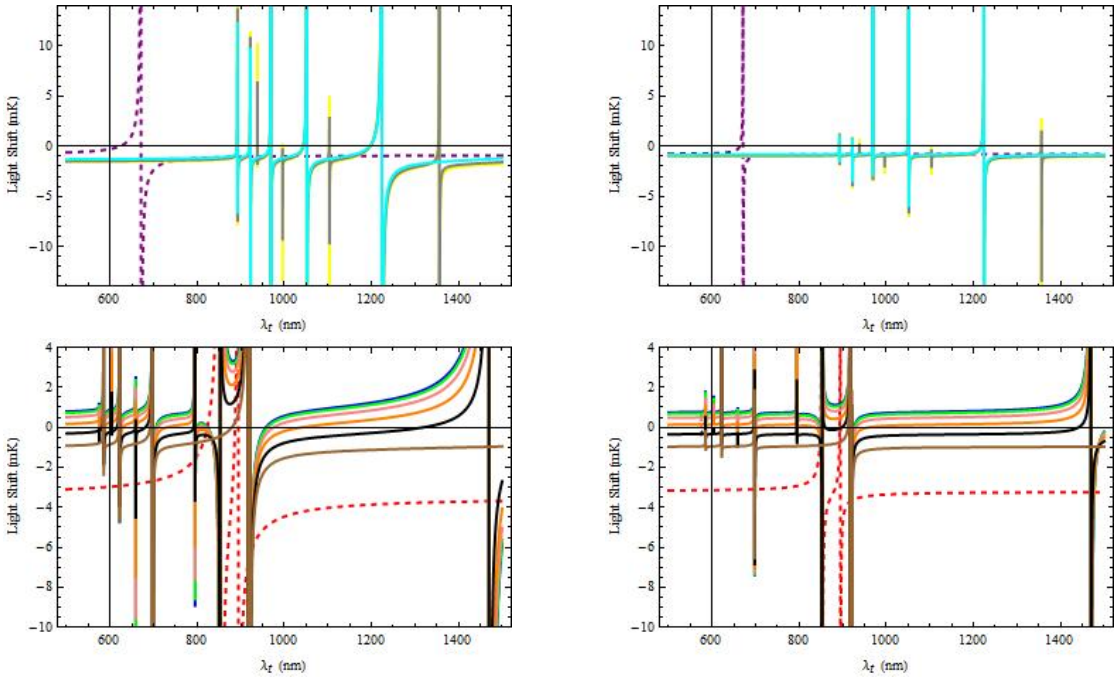

(g) $\lambda_t = 814.8\text{nm-}\lambda_c = 1070\text{nm}$ **(h)** $\lambda_t = 846.7\text{nm-}\lambda_c = 1075\text{nm}$

Figure 6.3: The top panel shows the AC Stark shift for ^{6}Li as a function of the trap laser wavelength where the purple dashed line is the ground state $2S_{1/2}$, yellow, gray and cyan lines are the excited state $3P_{3/2}$ of Lithium with $m = \pm 1/2, \pm 3/2, \pm 5/2$ Zeeman sublevels respectively. The bottom panel shows the AC Stark shift for ^{133}Cs as a function of trap laser wavelength where the red dashed line refers to the ground state $6S_{1/2}$, blue, green, pink, orange, black and brown lines refer to the excited state $6P_{3/2}$ of Caesium with $m = 0, \pm 1, \pm 2, \pm 3, \pm 4, \pm 5$ Zeeman sublevels respectively.

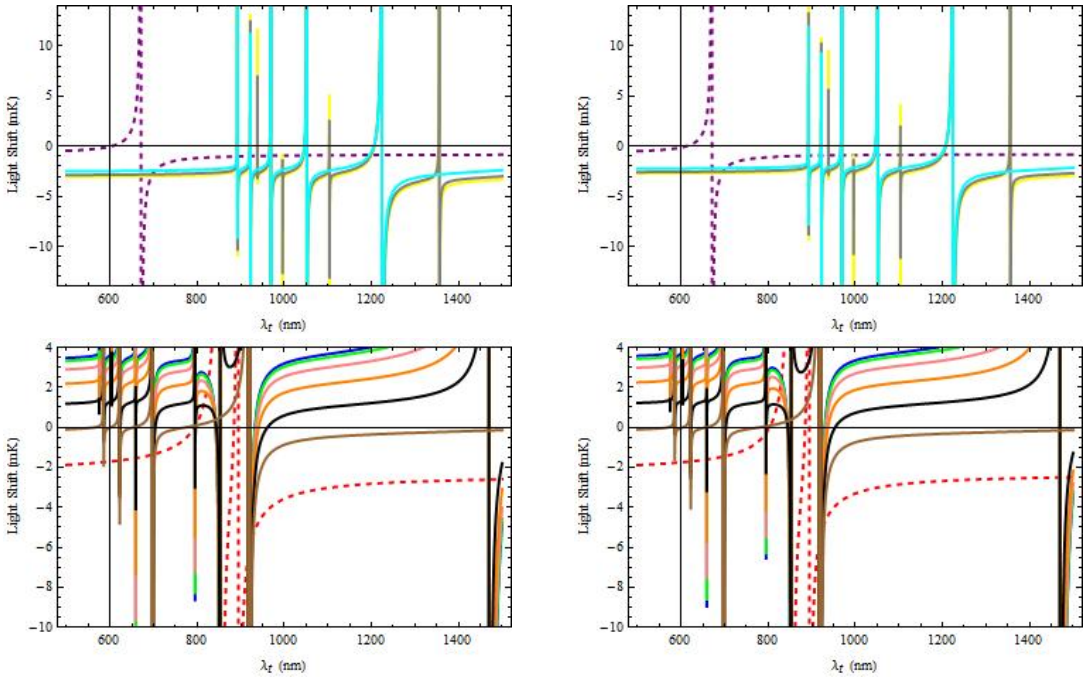

(i) $\lambda_t = 702.9\text{nm-}\lambda_c = 1280.3\text{nm}$ **(j)** $\lambda_t = 701.8\text{nm-}\lambda_c = 1286\text{nm}$

Figure 6.3: The top panel shows the AC Stark shift for ^{6}Li as a function of the trap laser wavelength where the purple dashed line is the ground state $2S_{1/2}$, yellow, gray and cyan lines are the excited state $3P_{3/2}$ of Lithium with $m = \pm 1/2, \pm 3/2, \pm 5/2$ Zeeman sublevels respectively. The bottom panel shows the AC Stark shift for ^{133}Cs as a function of trap laser wavelength where the red dashed line refers to the ground state $6S_{1/2}$, blue, green, pink, orange, black and brown lines refer to the excited state $6P_{3/2}$ of Caesium with $m = 0, \pm 1, \pm 2, \pm 3, \pm 4, \pm 5$ Zeeman sublevels respectively.

6.3 Effect of variations in experimental parameters

In this section the effect of variations in the wavelength of the trapping laser on dual-species state-independent trapping is investigated. The relative intensities of the trap and control lasers required for Caesium and Lithium are evaluated as a function of the trapping wavelength, with results presented in figure 6.5 for all ten wavelength combinations. The presented data indicates that it is not possible to counterbalance the variation in the wavelength by changing the intensity ratio of the lasers. Beyond the required value of the trapping wavelength, the corresponding intensity ratio of the lasers are different. As the variation in the wavelength of the trapping laser increases, the discrepancy in the required value of the relative intensities of the lasers for the simultaneous state-insensitive trapping increases further. Depending on the actual value of the magic wavelength combinations the conditions of the state-insensitive trapping differs for the two species. More specifically, for two of the magic wavelength combinations state-independent trapping of Lithium atom is more sensitive to the wavelength variations compared to the Caesium atom. This effect is quantified in table 6.3. The presented data indicates that all the magic wavelength combinations require a negligible change in the relative intensities of the lasers for the case of 0.1 nm variation in the wavelength of the trapping laser. Out of the ten magic wavelength combinations $814.8 - 1070$ nm and $846.7 - 1075$ nm trap/control laser wavelength combinations, which are of particular interest, require negligible change in the intensity ratio of the lasers even for the case of 0.5 nm variation in the trapping wavelength. This indeed assures that dual species state-insensitive can be maintained for wavelength variations below 0.5 nm.

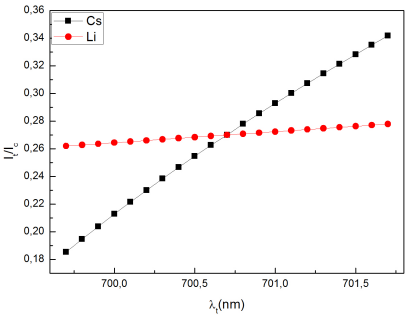

(a) $\lambda_t = 700.7\text{nm-}\lambda_c = 1064\text{nm}$

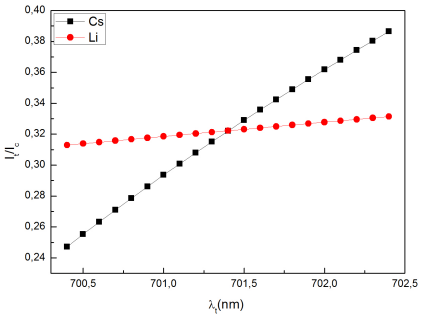

(b) $\lambda_t = 701.4\text{nm-}\lambda_c = 1063\text{nm}$

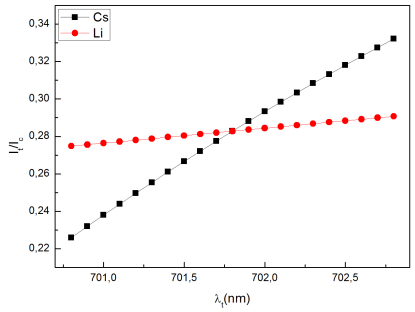

(c) $\lambda_t 701.8\text{nm-}\lambda_c = 1286\text{nm}$

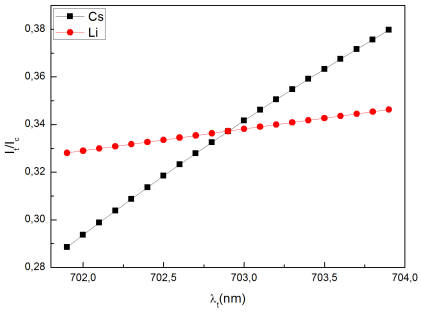

(d) $\lambda_t = 702.9\text{nm-}\lambda_c = 1280.3\text{nm}$

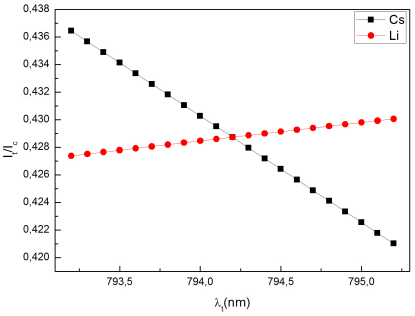

(e) $\lambda_t = 794.2\text{nm-}\lambda_c = 1067.3\text{nm}$

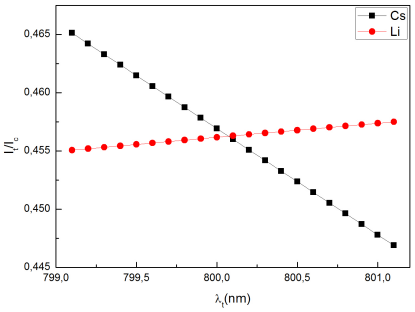

(f) $\lambda_t = 800.1\text{nm-}\lambda_c = 974.8\text{nm}$

Figure 6.4: Effect of trap wavelength fluctuations on the required intensity ratio of trap and control lasers for Cs and Li.

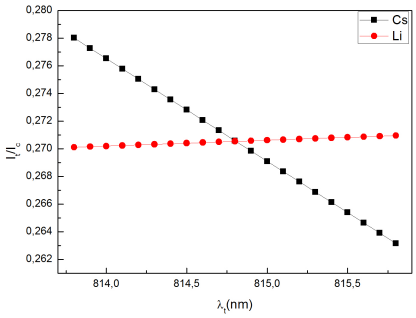

(g) $\lambda_t = 814.8\text{nm-}\lambda_c = 1070\text{nm}$

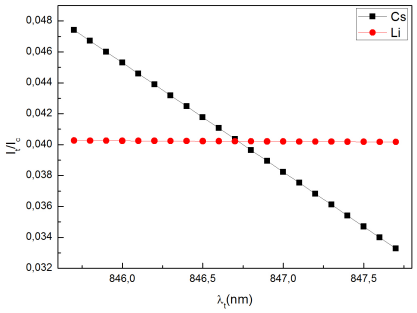

(h) $\lambda_t = 846.7\text{nm-}\lambda_c = 1075\text{nm}$

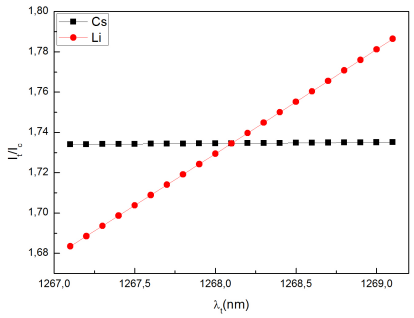

(i) $\lambda_t = 1268.1\text{nm-}\lambda_c = 711.4\text{nm}$

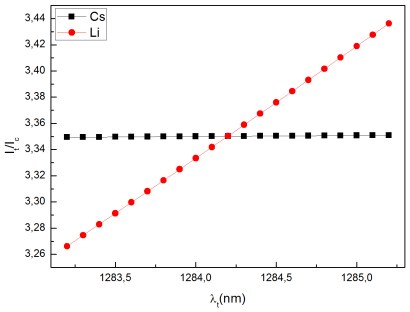

(j) $\lambda_t = 1284.2\text{nm-}\lambda_c = 702.1\text{nm}$

Figure 6.4: Effect of trap wavelength fluctuations on the required intensity ratio of trap and control lasers for Cs and Li.

$\lambda_t - \lambda_c$ (nm)	$\Delta I_t/I_c$ for $\Delta\lambda_t = 0.01$ nm	$\Delta I_t/I_c$ for $\Delta\lambda_t = 0.1$ nm	$\Delta I_t/I_c$ for $\Delta\lambda_t = 0.5$ nm
$700.7 - 1064$	1.090×10^{-3}	7.250×10^{-3}	3.348×10^{-2}
$701.4 - 1063$	4.670×10^{-4}	5.810×10^{-3}	2.861×10^{-2}
$701.8 - 1286$	4.670×10^{-4}	4.480×10^{-3}	2.156×10^{-2}
$702.9 - 1280.3$	1.688×10^{-1}	1.708×10^{-1}	1.796×10^{-1}
$794.2 - 1067.3$	9.450×10^{-5}	9.085×10^{-4}	4.530×10^{-3}
$800.1 - 974.8$	3.975×10^{-4}	1.330×10^{-3}	5.450×10^{-3}
$814.8 - 1070$	3.350×10^{-5}	7.395×10^{-4}	3.870×10^{-3}
$846.7 - 1075$	6.620×10^{-5}	5.659×10^{-4}	3.380×10^{-3}
$1268.1 - 711.4$	4.700×10^{-4}	5.070×10^{-3}	2.555×10^{-2}
$1284.2 - 7002.1$	1.070×10^{-3}	8.660×10^{-3}	4.256×10^{-2}

Table 6.3: Difference between the required trap/control lasers intensity ratio of the Caesium and Lithium atoms for maintaining state-insensitive trapping in case of $\lambda_t = 0.01, 0.1$ and 0.5 nm variation in trap laser wavelength.

Effects of the another experimental parameter, laser intensity, was also investigated. The divergence in the corresponding magic trap laser wavelengths of the two atomic species was analyzed by considering intensity variations of the trap and control lasers. The effect of intensity variations in trap/control laser intensity ratio is illustrated in figure 6.5 for all the ten magic wavelength combinations. The data indicates that a variation in the intensity ratio leads to different magic wavelength for the two atomic species, with the magic trapping wavelength of the Lithium atom showing greater deviation than that of the Cs atoms for most of the wavelength combinations. Notably, for the wavelength combinations $700.7 - 1064$ nm, $814.8 - 1070$ nm and $864.7 - 1075$ nm, which are of particular interest, conditions of state-independent trapping of Lithium atoms are more susceptible to variation in the relative intensities of the lasers. On the other hand, a peculiar effect was observed for the wavelength sets of $846.7 - 1075$ nm and $1284.2 - 702.1$ nm. The data given in figure 6.5 shows that an increase in the trapping laser wavelength indeed violates conditions of state-insensitive trapping of the Lithium and Caesium species respectively. To analyze this effect more

quantitatively, the magic trap laser wavelength of both atomic species are evaluated for 0.1% and 0.5% variation in the trap/control laser intensity ratio and listed in table 6.4. The data presented indicates that the deviations of the Lithium and Caesium from their magic trapping wavelengths increases with increasing intensity variations. It reveals that the discrepancy in the deviations between the magic wavelengths of the two atoms remains less than 1 nm for 0.1% variation in the relative intensities of the lasers for most of the magic wavelength combinations. Indeed, 0.5% variation in the intensity ratio of the trap and control lasers causes a shift less then 0.1 nm in the magic trapping wavelength of $700.7 - 1064$ nm wavelength combination. Therefore, small variations in the intensities of the lasers do not have a significant effect on the simultaneous state-insensitive trapping of the two atomic species.

$\lambda_t - \lambda_c$ (nm)	λ_t (nm) of Cs−Li for $\Delta I_t/I_c = 0.1\%$	λ_t (nm) of Cs−Li for $\Delta I_t/I_c = 0.5\%$
$700.7 - 1064$	700.66-700.36	700.52-699.06
$701.4 - 1063$	701.35-701.03	701.17-699.64
$701.8 - 1286$	701.75-701.45	701.54-700.04
$702.9 - 1280.3$	702.82-702.51	702.54-701.04
$794.2 - 1067.3$	794.76-791.10	769.98-780.37
$800.1 - 974.8$	800.60-796.28	802.60-794.32
$814.8 - 1070$	815.18-809.02	816.64-793.07
$846.7 - 1075$	846.78-853.37	874.00-866.47
$1268.1 - 711.4$	1240.27-1267.76	1175.01-1266.39
$1284.2 - 702.1$	1250.36-1283.8	1179.92-1282.19

Table 6.4: List of common magic wavelength combinations and the deviated magic trap laser wavelengths of Cs and Li for 0.1 and 0.5% variation in intensity ratios from the value leading to dual-species state-independent trapping. The data refer to a control laser power of 2 W and laser beam waists of 10 μm for both lasers.

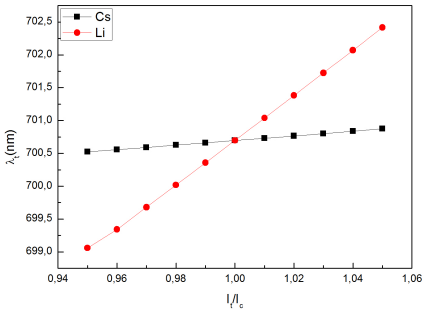

(a) $\lambda_t = 700.7$nm-$\lambda_c = 1064$nm

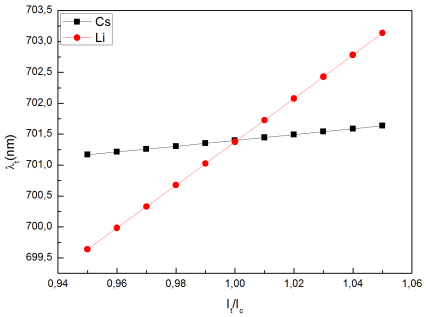

(b) $\lambda_t = 701.4$nm-$\lambda_c = 1063$nm

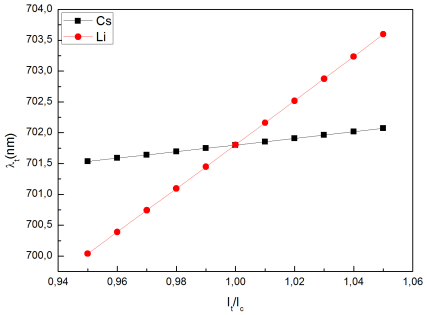

(c) λ_t701.8nm-$\lambda_c = 1286$nm

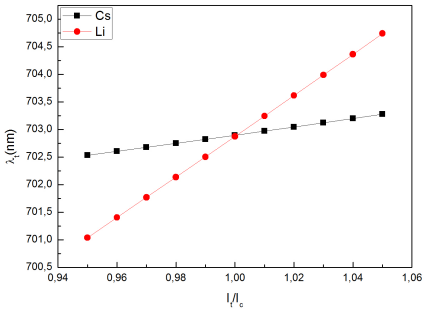

(d) $\lambda_t = 702.9$nm-$\lambda_c = 1280.3$nm

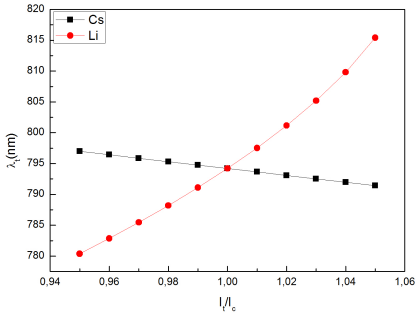

(e) $\lambda_t = 794.2$nm-$\lambda_c = 1067.3$nm

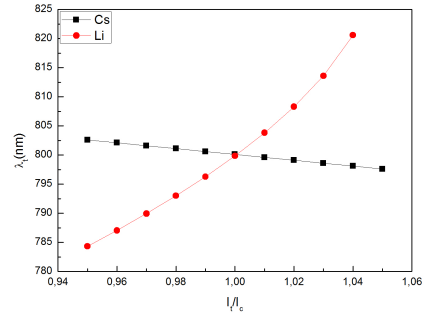

(f) $\lambda_t = 800.1$nm-$\lambda_c = 974.8$nm

Figure 6.5: Effect of trap wavelength fluctuations on the required intensity ratio of trap and control lasers for Cs and Li.

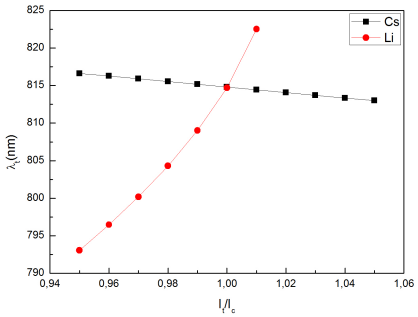

(g) $\lambda_t = 814.8\text{nm-}\lambda_c = 1070\text{nm}$

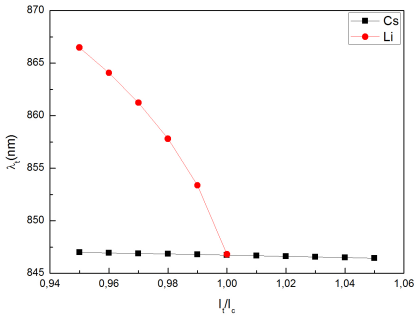

(h) $\lambda_t = 846.7\text{nm-}\lambda_c = 1075\text{nm}$

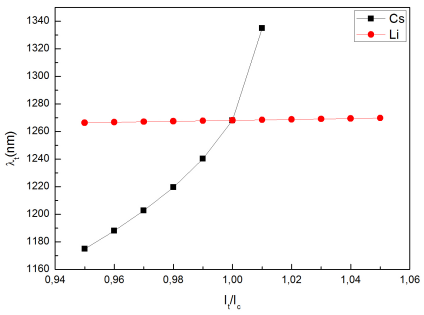

(i) $\lambda_t = 1268.1\text{nm-}\lambda_c = 711.4\text{nm}$

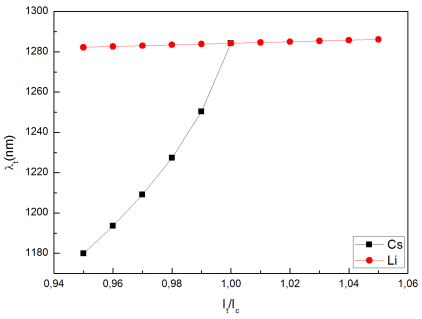

(j) $\lambda_t = 1284.2\text{nm-}\lambda_c = 702.1\text{nm}$

Figure 6.5: Effect of trap intensity fluctuations on the required intensity ratio of trap and control lasers for Cs and Li.

6.4 Species Selective State-Insensitive Trapping

Species selective trapping introduces flexibility to individually control the simultaneously trapped two atomic species in a mixture. In this technique the main purpose is to address one of the atomic species in a common trap either with little effect on the other one or no effect. As a matter of fact optical trapping is not species selective in contrast to other trapping methods such as magneto-optical trapping. However, there are techniques to engineer the trap depths of specific atomic species.

Optical trapping of different atomic species with selective confinement strengths was proposed by Onofrio and Presilla [100] using two overlapping optical traps. In this way the corresponding trap depths of each atomic specie of the mixture is adjusted by balancing the intensity of the two trapping lasers fields. Later, single frequency species-specific optical lattice is introduced by LeBlanc and Thywissen [101] considering tune-in and tune-out schemes. In the former trapping scheme, the light field is tuned close to resonance of one specie to achieve stonger induced dipole moment compared to the other species whereas in the latter scheme the light field is tuned to obtain vanishing induced dipole moment for one of the atomic species in a mixture. But, both approaches have disadvantages. The former causes significant increase in the scattering rates of the trapped atoms while the latter allows trapping of solely one atomic specie.

For certain cases, individual confinement of atomic species is of particular importance. Unique polarizabilities of the atoms result in a different trapping potential for each species leading to severe limitations in many experiments. Cooling fermionic atomic species by themselves using standard techniques is difficult since the Pauli principle limits the efficiency of the evaporative cooling among fermions in the same state. Thus sympathetic cooling of fermionic atom with coupling to bosonic atom is an alternative method. Manipulation of the trap depths of the atoms in a mixture via species-selective trap offers a degree of freedom to improve sympathetic cooling. Additionally, it allows

to remove the atomic species used for sympathetic cooling when the other atomic specie becomes sufficiently cool.

The different trap depths of the atoms in Lithium-Caesium mixture were reported to cause a fast loss in the number of lithium atoms during forced evaporative cooling towards quantum degeneracy which limits the lowest achievable temperature [102]. The ability to independently address each atom in Li-Cs mixture is crucial to achieve low temperatures. This makes species-specific optical trapping a promising technique to control the temperature and density of a specific atomic specie in a mixture. In this chapter selective bichromatic state-insensitive trapping of atoms in a Li-Cs mixture is explored. At a specific wavelength, called tune-out wavelength, the polarizability of an atom vanishes. Hence, the presence of the optical trap does not affect the atoms since they do not experience a dipole force. The tune-out wavelength combinations for both atoms are explored. By taking advantage of the tunability offered by bichromatic trapping the possibility of common wavelength sets, which the tune-out wavelength of one atomic specie coincides with the magic wavelength of the another one is investigated. Following the same approach for identification of the magic wavelength combinations, the results of the calculations indicated the presence of five wavelength sets for selective state-independent trapping of each specie in convenient frequency range for practical realization. These common wavelength sets for selective state-independent trapping of Ceasium and Lithium are listed in tables 6.5 and 6.6 respectively, with required intensity ratios of the trap/control lasers and the corresponding trap depths for contol laser power of 0.5 W and beam sizes of 10 μm for both lasers. Such an effect is also illustrated in figures 6.6 and 6.7 for Caesium and Lithium respectively. The data given in figure 6.6 indicates the selective state-independent trapping of Cs for $6S_{1/2}(F_g = 4) \rightarrow 6P_{3/2}(F_e = 5)$ transition at wavelength combination of $873.8 - 585$ nm. Similarly, the figure 6.7 shows that at wavelength combination of $778.2 - 1063.9$ nm the Caesium is not trapped whereas it corresponds to the magic wavelength set of the Lithium atom for $2S_{1/2}(F_g = 3/2) \rightarrow 2P_{3/2}(F_e = 5/2)$ tran-

sition.

$\lambda_t - \lambda_c$ (nm)	I_t/I_c	U_{Cs} (mK)
$873.8 - 585$	1.297	1.96
$1043.2 - 585.4$	1.862	1.45
$1049.4 - 622.4$	3.634	2.90
$1592.1 - 585.3$	2.606	0.80
$1813.6 - 585.2$	2.730	0.75

Table 6.5: List of magic wavelength combinations for selective state-independent trapping of Caesium with corresponding intensity ratio of the lasers and the trap depth for 0.5 W control laser power and 10 μm beam size.

$\lambda_t - \lambda_c$ (nm)	I_t/I_c	U_{Li} (mK)
$778.2 - 1063.9$	0.698	0.51
$824.7 - 1070.3$	0.257	0.28
$849.1 - 1075.2$	0.033	0.20
$892.4 - 878.8$	0.021	0.29
$892.9 - 1079.7$	0.034	0.20

Table 6.6: List of magic wavelength combinations for selective state-independent trapping of Lithium with corresponding intensity ratio of the lasers and the trap depth for 0.5 W control laser power and 10 μm beam size.

6.5 Conclusion

In this chapter the possibility of simultaneous state-independent trapping of two different atomic species was investigated. More specifically, a Fermi-Bose mixture of lithium and caesium was considered. As the magic wavelengths of the lithium and caesium atoms are different, dual-species state-insensitive trapping is not possible with a single frequency. Therefore, bichromatic trapping was proposed as an effective tool to tune the two magic

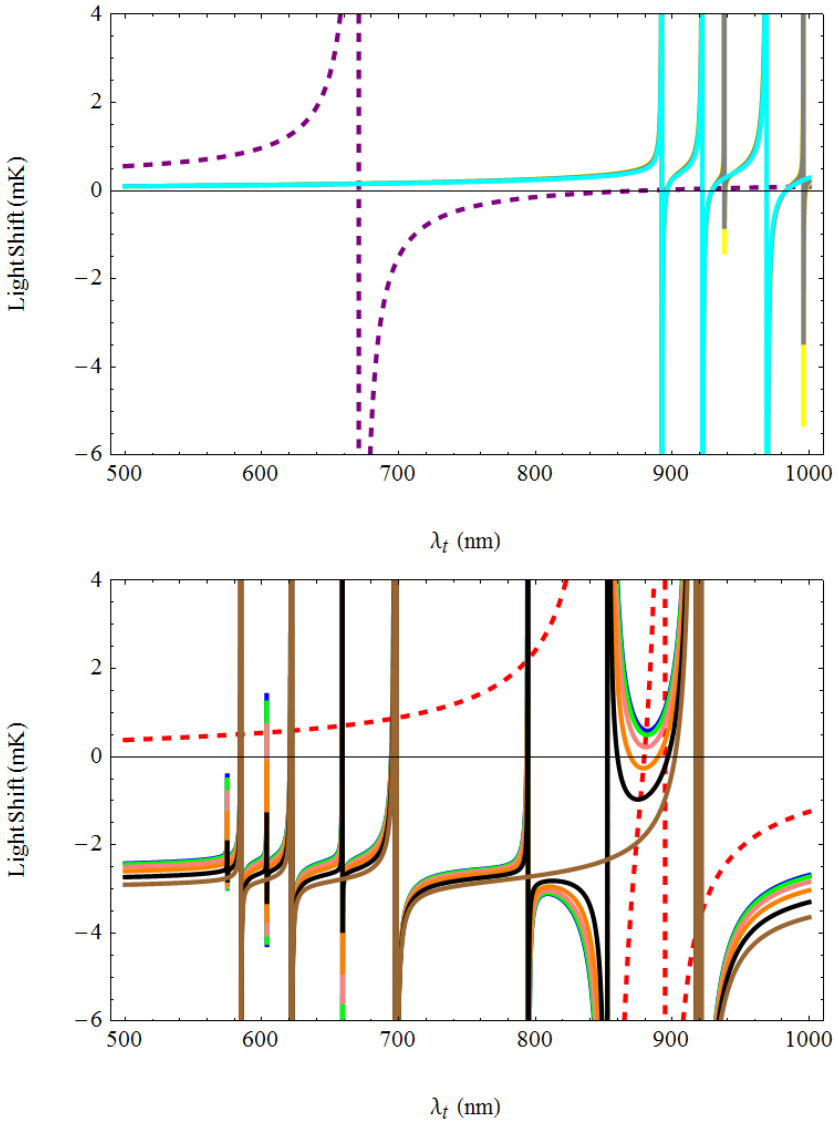

Figure 6.6: The top panel shows AC Stark shift for ^{6}Li as function of trap laser wavelength where purple dashed line is the ground state $2S_{1/2}$, yellow, gray and cyan lines are the excited state $3P_{3/2}$ of Lithium with $m = \pm 1/2, \pm 3/2, \pm 5/2$ Zeeman sublevels respectively. The bottom panel shows AC Stark shift for ^{133}Cs as function of trap laser wavelength where red dashed line is the ground state $6S_{1/2}$, blue, green, pink, orange, black and brown lines are the excited state $6P_{3/2}$ of Caesium with $m = 0, \pm 1, \pm 2, \pm 3, \pm 4, \pm 5$ Zeeman sublevels respectively.

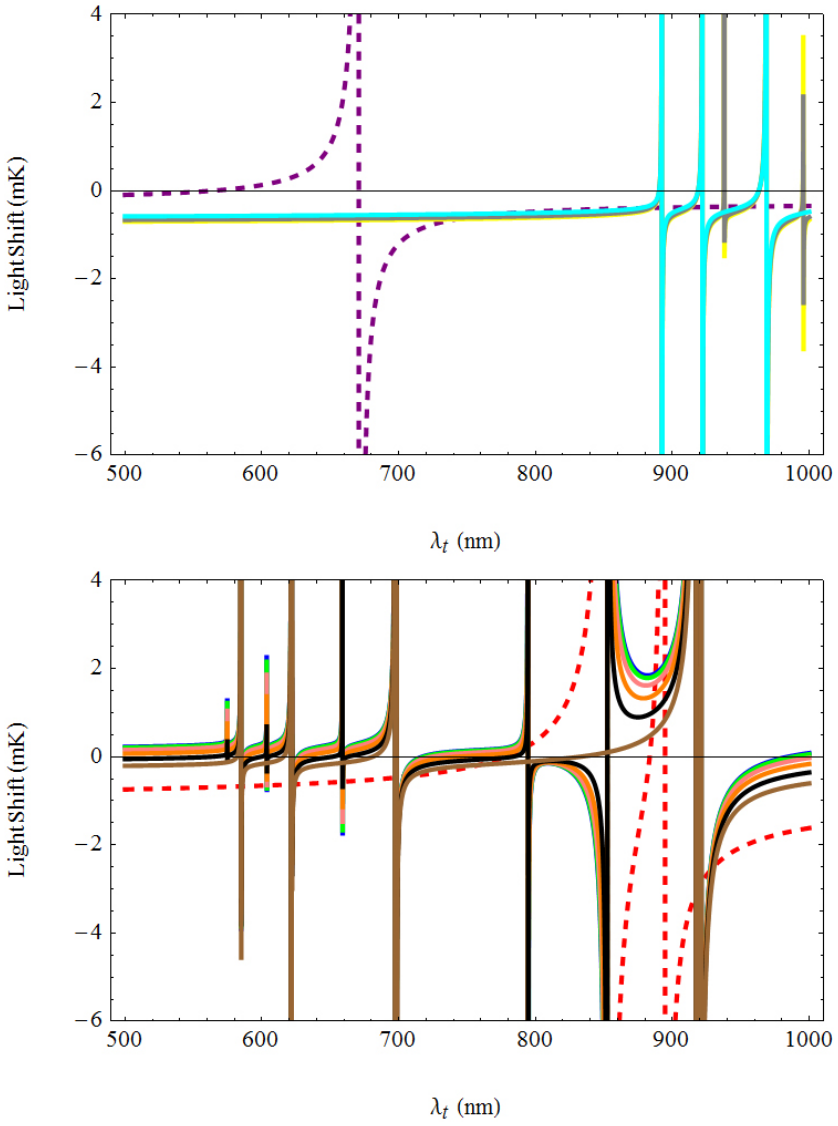

Figure 6.7: The top panel shows AC Stark shift for ^{6}Li as function of trap laser wavelength where purple dashed line is the ground state $2S_{1/2}$, yellow, gray and cyan lines are the excited state $3P_{3/2}$ of Lithium with $m = \pm 1/2, \pm 3/2, \pm 5/2$ Zeeman sublevels respectively. The bottom panel shows AC Stark shift for ^{133}Cs as function of trap laser wavelength where red dashed line is the ground state $6S_{1/2}$, blue, green, pink, orange, black and brown lines are the excited state $6P_{3/2}$ of Caesium with $m = 0, \pm 1, \pm 2, \pm 3, \pm 4, \pm 5$ Zeeman sublevels respectively.

wavelengths of the two atoms to a common value. Accordingly, ten common magic wavelength combinations were identified to achieve simultaneous state-insensitive trapping of the two atomic species. In particular, the identified combinations of $700.7 - 1064$ nm, $814.8 - 1070$ nm and $846.7 - 1075$ nm are appealing in terms of experimental implementation. These wavelengths can be accessed by utilizing a diode laser as trap laser, and a Nd:YAG or a ytterbium fiber lasers as control laser. The effects of uncertainties were observed to be negligible for implementing the state-insensitive trapping. The effects of undesired variations in experimental parameters on the simultaneous state-independent trapping of the two species were also discussed. Additionally species selective state-independent trapping of caesium and lithium atoms in mixture was investigated. Wavelength combinations for selective trapping of each atoms were identified.

Chapter 7

Conclusion

In the presented work, state-insensitive trapping of Caesium atom and its mixtures with Rubidium and Lithium atoms is theoretically investigated. The magic wavelength of 935 nm for single frequency state-insensitive trapping of Caesium atom is sometimes of limited use for practical implementation, when the light sources with sufficiently high power is not available. To address this problem, bichromatic trapping scheme was proposed and appropriate magic wavelength combinations were numerically determined. The approach for computing the AC Stark shift induced by the dipole trap laser was described and the equation to evaluate the light shift in terms of experimental parameters was determined. All the calculations were performed using mathematica and the required input data were taken from references [34–36]. For the special cases of $2\lambda_{trap} = \lambda_{control}$ and $3\lambda_{trap} = \lambda_{control}$ for equal intensities, which can be achieved via second and third harmonic generation from a single laser source, the magic wavelength combinations were determined as $931.8 - 1863.6$ nm and $927.5 - 2782.5$ nm respectively. Then the magic wavelength combinations accessible by commercially available high power lasers were identified. The appropriate control laser wavelengths were found to be 1064 nm, 1070 nm, 1075 nm and 1080 nm, and the corresponding trap wavelengths were identified in the range of $585 - 588$ nm and $623 - 629$ nm. All these control laser wavelengths can be obtained by using a Nd:YAG or a Ytterbium fiber laser as the control laser and red and orange Raman

fiber lasers as the trap laser. The uncertainties in the input parameters of the calculations led to negligible small uncertainties in values of the identified magic trapping wavelengths. Thus, they do not have an effect on implementation of the state-insensitive trap. As a result, it was shown that bichromatic trapping scheme offers wide range of possible magic wavelengths compared to monochromatic trapping scheme. It allows tunability in either the magic wavelength or intensity requirements by varying the other parameters of the two lasers. In this way, limitations introduced in the case of single frequency state-independent trapping on the frequency range and power of the laser field are overcome by the bichromatic trapping method. In this respect, bichromatic state-insensitive trapping is more advantageous than the monochromatic trapping.

The possibility of dual-species state-independent trapping was also investigated. First, simultaneous state-insensitive trapping of the two different atomic species with same statistical properties was explored. We extended the calculations for state-insensitive trapping of caesium atom to its mixture with Rubidium atom. As the magic wavelengths of these two atoms are very different, it is not possible to obtain simultaneous state-insensitive trapping with monochromatic trapping schemes. We noticed that bichromatic trapping schemes offers tunability to a sufficient extent to obtain same magic wavelength combinations for the two atomic species. Among these identified magic wavelengths, the set of 868.94 nm and 10.6 μm has potential for experimental realization as can be accessed by a diode and a CO_2 laser. The other mixture considered was the Fermi-Bose mixture of lithium and caesium. Considering the narrow line cooling of the lithium atoms, magic wavelength of the two species were reported to be different. Therefore, we used the bichromatic approach to tune their magic wavelength to a common value. In this way, a number of common magic wavelength combinations were found. Three of them are of particular interest as they can be accessible by the current laser technology. These wavelengths can be achieved by utilizing a diode laser as trap laser, and Nd:YAG or ytterbium fiber lasers as control laser. In addition to the identification of the magic wavelengths, unwanted effects of the intensity and wavelength fluctuations on the possibility

of dual-species state-insensitive trapping was analyzed and the conditions to preserve the state-independent trapping was determined. Moreover, species selective state-independent trapping was investigated and wavelength combinations were determined. In all calculations performed, uncertainty in the input data used led to negligible uncertainty in values of the identified magic wavelength for caesium atom, rubidium-caesium and lithium-caesium atomic mixtures as previously stated.

For both single and dual species trapping, state-independent trapping plays significant role in many experiments. In addition to being a solution for the inconvenient magic wavelength, bichromatic state-independent trapping can be used to selectively address a specific atomic species as in free space. Demonstration of the presence of the identified wavelength combinations would open a way to various experiments. More specifically, selective state-independent trapping can be used to achieve colder temperatures and thus to access to low energy regime of many-body physics. Moreover, extra degree of freedom introduced is useful to prepare more detailed conditions for the atoms. Despite the previous experiments with two colour fields aiming to decrease the amount of differential light shift, there is no work reported for realization of the bichromatic state-insensitive trapping.

Experimental verification of the identified magic wavelengths for bichromatic trapping of caesium atom is the next step for the presented work. Therefore, an experimental setup for bichromatic optical trapping scheme will be implemented to test the state-insensitive trapping at determined magic wavelength combinations.

Appendix A

MOT Coil Current Control System

The current passing through the MOT coil is ramped, switch on and off by a control circuit. It is a MOSFET circuit connected between the power supply and the coils. In this appendix its schematic is given.

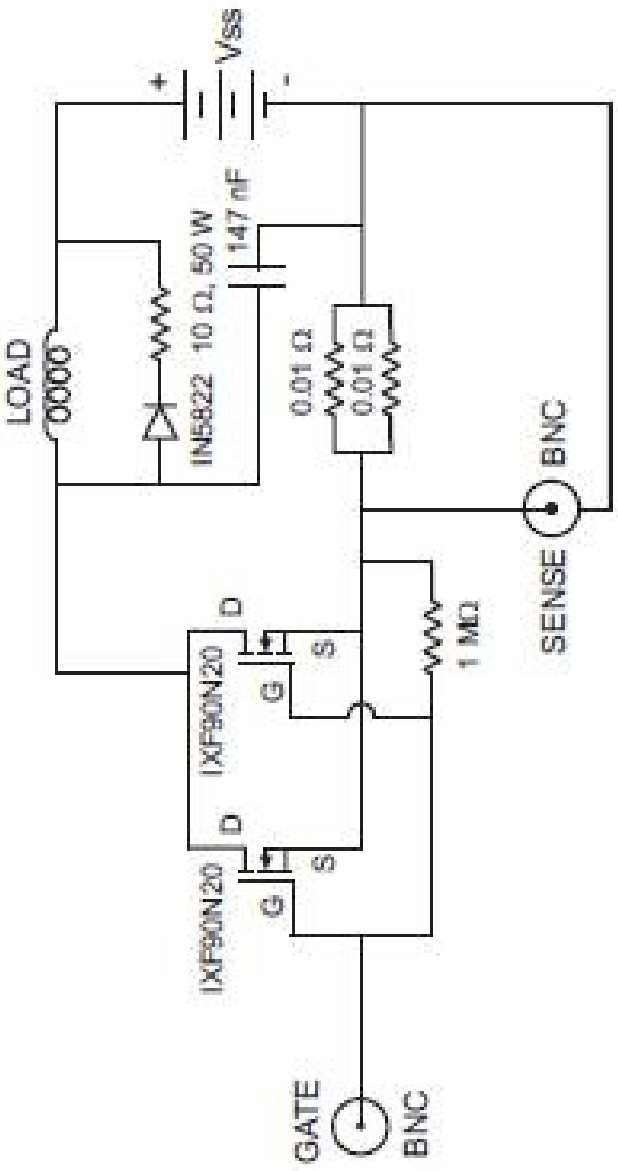

Figure A.1: MOSFET Circuit Schematic

Appendix B

Transition Wavelengths and Corresponding Transition Probabilities of ^{133}Cs

Level $nP_{1/2}$	$\lambda_{1/2}$ (nm)	Uncertainty in $\lambda_{1/2}$ (nm)	$A_{1/2}$ (1/s)
$6P_{1/2}$	894.5928	6.0×10^{-9}	2.89×10^{7}
$7P_{1/2}$	459.4395	5.0×10^{-5}	1.576×10^{6}
$8P_{1/2}$	388.9667	5.0×10^{-7}	4.429×10^{5}
$9P_{1/2}$	361.83	19×10^{-6}	1.923×10^{5}
$10P_{1/2}$	348.1035	5.0×10^{-5}	1.015×10^{5}
$11P_{1/2}$	340.0935	5.0×10^{-5}	5.969×10^{4}
$12P_{1/2}$	334.9764	5.0×10^{-5}	3.716×10^{4}

Table B.1: List of transition wavelengths and partial lifetimes for $nP_{1/2} \rightarrow 6S_{1/2}$ transition [34–36].

Level $nP_{3/2}$	$\lambda_{1/2}$ (nm)	Uncertainty in $\lambda_{1/2}$ (nm)	$A_{1/2}$ (1/s)
$6P_{3/2}$	852.3472	2.0×10^{-8}	3.257×10^{7}
$7P_{3/2}$	455.6502	5.0×10^{-5}	4.186×10^{6}
$8P_{3/2}$	387.7205	5.0×10^{-7}	1.574×10^{6}
$9P_{3/2}$	361.2461	19×10^{-5}	7.933×10^{5}
$10P_{3/2}$	347.7785	5.0×10^{-4}	4.65×10^{5}
$11P_{3/2}$	339.8921	5.0×10^{-4}	3.002×10^{5}
$12P_{3/2}$	334.8432	5.0×10^{-4}	2.082×10^{5}

Table B.2: List of transition wavelengths and partial lifetimes for $nP_{3/2} \rightarrow 6S_{1/2}$ transition [34–36].

Level $nS_{1/2}$	$\lambda_{3/2}$ (nm)	Uncertainty in $\lambda_{3/2}$ (nm)	$A_{3/2}$ (1/s)
$7S_{1/2}$	1469.8941	21×10^{-5}	1.218×10^{7}
$8S_{1/2}$	794.6067	5.0×10^{-5}	3.621×10^{6}
$9S_{1/2}$	658.8329	5.0×10^{-5}	1.681×10^{6}
$10S_{1/2}$	603.5761	5.0×10^{-5}	9.091×10^{5}
$11S_{1/2}$	574.7318	5.0×10^{-5}	5.226×10^{5}

Table B.3: List of transition wavelengths and partial lifetimes for $nS_{1/2} \rightarrow 6P_{3/2}$ transition [34–36].

Level $nD_{3/2}$	$\lambda_{3/2}$ (nm)	Uncertainty in $\lambda_{3/2}$ (nm)	$A_{3/2}$ (1/s)
$5D_{3/2}$	3614.0890	24×10^{-4}	1.222×10^{5}
$6D_{3/2}$	921.1002	8.0×10^{-5}	2.676×10^{6}
$7D_{3/2}$	698.5410	5.0×10^{-5}	1.296×10^{6}
$8D_{3/2}$	621.9315	5.0×10^{-5}	6.992×10^{5}
$9D_{3/2}$	584.9119	5.0×10^{-5}	4.196×10^{5}

Table B.4: List of transition wavelengths and partial lifetimes for $nD_{3/2} \rightarrow 6P_{3/2}$ transition [34–36].

Level $nD_{5/2}$	$\lambda_{5/2}$ (nm)	Uncertainty in $\lambda_{5/2}$ (nm)	$A_{5/2}$ (1/s)
$5D_{5/2}$	3490.9656	3.0×10^{-3}	8.396×10^{5}
$6D_{5/2}$	917.4714	8.0×10^{-5}	1.492×10^{7}
$7D_{5/2}$	697.5192	5.0×10^{-5}	7.514×10^{6}
$8D_{5/2}$	621.4796	5.0×10^{-5}	4.170×10^{6}
$9D_{5/2}$	584.6670	5.0×10^{-5}	2.589×10^{6}

Table B.5: List of transition wavelengths and partial lifetimes for $nD_{5/2} \rightarrow 6P_{3/2}$ transition [34–36].

Appendix C

Transition Wavelengths and Corresponding Transition Probabilities of ^{87}Rb

Level $nP_{1/2}$	$\lambda_{1/2}$ (nm)	Uncertainty in $\lambda_{1/2}$ (nm)	$A_{1/2}$ (1/s)
$5P_{1/2}$	794.9783	1.0×10^{-3}	3.592×10^{7}
$6P_{1/2}$	421.6706	5.0×10^{-4}	2.456×10^{6}
$7P_{1/2}$	359.2593	5.0×10^{-4}	7.266×10^{5}
$8P_{1/2}$	335.1772	6.0×10^{-4}	3.233×10^{5}
$9P_{1/2}$	323.0085	5.0×10^{-4}	1.732×10^{5}
$10P_{1/2}$	315.9170	5.0×10^{-4}	1.033×10^{5}

Table C.1: List of transition wavelengths and partial lifetimes for $nP_{1/2} \rightarrow 5S_{1/2}$ transition [34, 35, 87].

Level $nP_{3/2}$	$\lambda_{1/2}$ (nm)	Uncertainty in $\lambda_{1/2}$ (nm)	$A_{1/2}$ (1/s)
$5P_{3/2}$	780.2405	1.0×10^{-3}	3.755×10^{7}
$6P_{3/2}$	420.2972	5.0×10^{-4}	3.664×10^{6}
$7P_{3/2}$	358.8070	5.0×10^{-4}	1.266×10^{6}
$8P_{3/2}$	334.9655	6.0×10^{-4}	5.835×10^{5}
$9P_{3/2}$	322.8908	5.0×10^{-4}	3.296×10^{5}
$10P_{3/2}$	315.8441	5.0×10^{-4}	2.071×10^{5}

Table C.2: List of transition wavelengths and partial lifetimes for $nP_{3/2} \rightarrow 5S_{1/2}$ transition [34, 35, 87].

Level $nS_{1/2}$	$\lambda_{3/2}$ (nm)	Uncertainty in $\lambda_{3/2}$ (nm)	$A_{3/2}$ (1/s)
$6S_{1/2}$	1366.6729	1.0×10^{-3}	1.311×10^{7}
$7S_{1/2}$	741.0207	1.0×10^{-4}	4.400×10^{6}
$8S_{1/2}$	616.1324	1.0×10^{-4}	2.192×10^{6}
$9S_{1/2}$	565.5309	1.0×10^{-4}	1.130×10^{6}
$10S_{1/2}$	539.2057	1.0×10^{-4}	7.073×10^{5}

Table C.3: List of transition wavelengths and partial lifetimes for $nS_{1/2} \rightarrow 5P_{3/2}$ transition [34, 35, 87].

Level $nD_{3/2}$	$\lambda_{3/2}$ (nm)	Uncertainty in $\lambda_{3/2}$ (nm)	$A_{3/2}$ (1/s)
$4D_{3/2}$	1529.3116	1.0×10^{-3}	2.080×10^{6}
$5D_{3/2}$	776.1564	1.0×10^{-3}	4.788×10^{5}
$6D_{3/2}$	630.0963	1.0×10^{-3}	5.312×10^{5}
$7D_{3/2}$	572.6190	1.0×10^{-3}	3.966×10^{5}
$8D_{3/2}$	543.3333	1.0×10^{-3}	2.824×10^{5}

Table C.4: List of transition wavelengths and partial lifetimes for $nD_{3/2} \rightarrow 5P_{3/2}$ transition [34, 35, 87].

Level $nD_{5/2}$	$\lambda_{5/2}$ (nm)	Uncertainty in $\lambda_{5/2}$ (nm)	$A_{5/2}$ (1/s)
$4D_{5/2}$	1529.4144	1.0×10^{-3}	1.250×10^{7}
$5D_{5/2}$	775.9782	1.0×10^{-4}	2.706×10^{6}
$6D_{5/2}$	630.0066	1.0×10^{-4}	3.157×10^{6}
$7D_{5/2}$	572.5695	1.0×10^{-4}	2.457×10^{6}
$8D_{5/2}$	543.3035	1.0×10^{-4}	1.659×10^{6}

Table C.5: List of transition wavelengths and partial lifetimes for $nD_{5/2} \rightarrow 5P_{3/2}$ transition [34, 35, 87].

Appendix D

Transition Wavelengths and Corresponding Transition Probabilities of ^{6}Li

Level $nP_{1/2}$	$\lambda_{1/2}$ (nm)	Uncertainty in $\lambda_{1/2}$ (nm)	$A_{1/2}$ (1/s)
$2P_{1/2}$	670.9926	1.7×10^{-2}	3.721×10^{7}
$3P_{1/2}$	323.3564	2.6×10^{-3}	8.928×10^{5}
$4P_{1/2}$	274.1996	1.4×10^{-3}	1.161×10^{6}
$5P_{1/2}$	256.3070	1.0×10^{-3}	7.991×10^{5}
$6P_{1/2}$	247.5780	3.0×10^{-3}	5.268×10^{5}
$7P_{1/2}$	242.6149	2.1×10^{-3}	3.567×10^{5}
$8P_{1/2}$	239.5116	4.0×10^{-4}	2.573×10^{5}
$9P_{1/2}$	237.4267	7.0×10^{-4}	1.791×10^{5}
$10P_{1/2}$	235.9650	1.0×10^{-10}	1.723×10^{5}
$11P_{1/2}$	234.9122	1.8×10^{-2}	1.404×10^{5}
$12P_{1/2}$	234.0871	1.0×10^{-4}	7.877×10^{4}

Table D.1: List of transition wavelengths and partial lifetimes for $nP_{1/2} \rightarrow 2S_{1/2}$ transition [34–36].

Level $nP_{3/2}$	$\lambda_{1/2}$ (nm)	Uncertainty in $\lambda_{1/2}$ (nm)	$A_{1/2}$ (1/s)
$2P_{3/2}$	670.9776	1.7×10^{-2}	3.721×10^{7}
$3P_{3/2}$	323.3564	2.6×10^{-3}	8.906×10^{5}
$4P_{3/2}$	274.1996	1.4×10^{-3}	1.159×10^{6}
$5P_{3/2}$	256.3070	1.0×10^{-3}	7.972×10^{5}
$6P_{3/2}$	247.5780	3.0×10^{-3}	5.256×10^{5}
$7P_{3/2}$	242.6149	2.1×10^{-3}	3.558×10^{5}
$8P_{3/2}$	239.5116	4.0×10^{-4}	2.567×10^{5}
$9P_{3/2}$	237.4267	7.0×10^{-4}	1.787×10^{5}
$10P_{3/2}$	235.9650	1.0×10^{-10}	1.719×10^{5}
$11P_{3/2}$	234.9122	1.8×10^{-2}	1.400×10^{5}
$12P_{3/2}$	234.0871	1.0×10^{-4}	7.858×10^{4}

Table D.2: List of transition wavelengths and partial lifetimes for $nP_{3/2} \rightarrow 2S_{1/2}$ transition [34–36].

Level $nS_{1/2}$	$\lambda_{3/2}$ (nm)	Uncertainty in $\lambda_{3/2}$ (nm)	$A_{3/2}$ (1/s)
$2S_{1/2}$	670.9776	1.7×10^{-2}	3.721×10^{7}
$3S_{1/2}$	812.8686	6.0×10^{-4}	2.178×10^{7}
$4S_{1/2}$	497.3131	9.0×10^{-4}	6.758×10^{6}
$5S_{1/2}$	427.4330	1.0×10^{-10}	3.072×10^{6}
$6S_{1/2}$	398.6665	5.0×10^{-4}	1.667×10^{6}
$7S_{1/2}$	383.6709	1.0×10^{-10}	1.005×10^{6}
$8S_{1/2}$	374.7643	1.0×10^{-10}	6.540×10^{5}

Table D.3: List of transition wavelengths and partial lifetimes for $nS_{1/2} \rightarrow 2P_{3/2}$ transition [34–36].

Level $nS_{1/2}$	$\lambda_{3/2}$ (nm)	Uncertainty in $\lambda_{3/2}$ (nm)	$A_{3/2}$ (1/s)
$2S_{1/2}$	323.3564	2.6×10^{-3}	8.906×10^{5}
$3S_{1/2}$	2688.5104	1.0×10^{-10}	3.690×10^{6}
$4S_{1/2}$	2447.1346	2.4×10^{-1}	4.907×10^{6}
$5S_{1/2}$	1356.1454	8.5×10^{-1}	1.856×10^{6}
$6S_{1/2}$	1103.5117	1.0×10^{-10}	9.606×10^{5}
$7S_{1/2}$	995.7820	1.0×10^{-10}	5.659×10^{5}
$8S_{1/2}$	937.9281	1.0×10^{-10}	3.629×10^{5}

Table D.4: List of transition wavelengths and partial lifetimes for $nS_{1/2} \rightarrow 3P_{3/2}$ transition [34–36].

Level $nD_{3/2}$	$\lambda_{3/2}$ (nm)	Uncertainty in $\lambda_{3/2}$ (nm)	$A_{3/2}$ (1/s)
$3D_{3/2}$	610.5354	1.4×10^{-3}	1.126×10^{7}
$4D_{3/2}$	460.4187	7.0×10^{-4}	3.826×10^{6}
$5D_{3/2}$	413.3785	5.5×10^{-3}	1.788×10^{6}
$6D_{3/2}$	391.6456	4.0×10^{-4}	9.892×10^{5}
$7D_{3/2}$	379.6133	3.3×10^{-2}	6.059×10^{5}
$8D_{3/2}$	372.1927	2.1×10^{-2}	3.995×10^{5}
$9D_{3/2}$	367.2704	1.0×10^{-10}	2.768×10^{6}

Table D.5: List of transition wavelengths and partial lifetimes for $nD_{3/2} \rightarrow 2P_{3/2}$ transition [34–36].

Level $nD_{3/2}$	$\lambda_{3/2}$ (nm)	Uncertainty in $\lambda_{3/2}$ (nm)	$A_{3/2}$ (1/s)
$4D_{3/2}$	1755.0874	6.1×10^{-1}	1.118×10^{6}
$5D_{3/2}$	1224.1004	6.0×10^{-1}	5.720×10^{5}
$6D_{3/2}$	1051.3424	1.0×10^{-10}	3.255×10^{5}
$7D_{3/2}$	968.9024	1.0×10^{-10}	2.016×10^{5}
$8D_{3/2}$	921.9855	1.0×10^{-10}	1.335×10^{5}
$9D_{3/2}$	892.3585	1.0×10^{-10}	9.289×10^{4}

Table D.6: List of transition wavelengths and partial lifetimes for $nD_{3/2} \rightarrow 3P_{1/2}$ transition [34–36].

Level $nD_{5/2}$	$\lambda_{5/2}$ (nm)	Uncertainty in $\lambda_{5/2}$ (nm)	$A_{5/2}$ (1/s)
$3D_{5/2}$	610.5339	1.0×10^{-10}	6.848×10^{7}
$4D_{5/2}$	460.4184	4.0×10^{-4}	2.326×10^{7}
$5D_{5/2}$	413.3784	6.0×10^{-4}	1.087×10^{7}
$6D_{5/2}$	391.6455	5.0×10^{-4}	6.014×10^{6}
$7D_{5/2}$	379.6133	3.3×10^{-2}	3.684×10^{6}
$8D_{5/2}$	372.1927	2.1×10^{-1}	2.429×10^{6}
$9D_{5/2}$	367.2704	1.0×10^{-10}	1.683×10^{6}

Table D.7: List of transition wavelengths and partial lifetimes for $nD_{5/2} \rightarrow 2P_{3/2}$ transition [34–36].

Level $nD_{5/2}$	$\lambda_{5/2}$ (nm)	Uncertainty in $\lambda_{5/2}$ (nm)	$A_{5/2}$ (1/s)
$4D_{5/2}$	1755.0828	6.2×10^{-1}	6.798×10^5
$5D_{5/2}$	1224.0992	5.9×10^{-1}	3.478×10^6
$6D_{5/2}$	1051.3421	1.0×10^{-10}	1.979×10^6
$7D_{5/2}$	968.9024	1.0×10^{-10}	1.226×10^6
$8D_{5/2}$	921.9855	1.0×10^{-10}	8.119×10^5
$9D_{5/2}$	892.3585	1.0×10^{-10}	5.648×10^5

Table D.8: List of transition wavelengths and partial lifetimes for $nD_{5/2} \rightarrow 3P_{3/2}$ transition [34–36].

Bibliography

[1] C. N. Cohen-Tannoudji. Nobel lecture: Manipulating atoms with photons. *Rev. of Mod. Phys.*, 70(3):707, 1998.

[2] W. D. Phillips. Nobel lecture: Laser cooling and trapping of neutral atoms. *Rev. of Mod. Phys.*, 70(3):721, 1998.

[3] S. Chu. Nobel lecture: The manipulation of neutral particles. *Rev. of Mod. Phys.*, 70(3):685, 1998.

[4] W. Ketterle. Nobel lecture: When atoms behave as waves: Bose-einstein condensation and the atom laser. *Rev. of Mod. Phys.*, 74(4):1131, 2002.

[5] E. A. Cornell and C. E. Wieman. Nobel lecture: Bose-einstein condensation in a dilute gas, the first 70 years and some recent experiments. *Rev. of Mod. Phys.*, 74(3):875, 2002.

[6] T. W. Hänsch and A. L. Schawlow. Cooling of gases by laser radiation. *Opt. Comm.*, 13(1):68–69, 1975.

[7] D. J. Wineland, R. E. Drullinger, and F. L. Walls. Radiation-pressure cooling of bound resonant absorbers. *Phys. Rev. Lett.*, 40:1639–1642, Jun 1978.

[8] W. Neuhauser, M. Hohenstatt, P. Toschek, and H. Dehmelt. Optical-sideband cooling of visible atom cloud confined in parabolic well. *Phys. Rev. Lett.*, 41:233–236, Jul 1978.

[9] S. Chu, L. Hollberg, J. E. Bjorkholm, A. Cable, and A. Ashkin. Three-dimensional viscous confinement and cooling of atoms by resonance radiation pressure. *Phys. Rev. Lett.*, 55(1):48, 1985.

[10] E. L. Raab, M. Prentiss, A. Cable, S. Chu, and D. E. Pritchard. Trapping of neutral sodium atoms with radiation pressure. *Phys. Rev. Lett.*, 59(23):2631, 1987.

[11] G. A. Askar'yan. Effects of the gradient of a strong electromagnetic beam on electrons and atoms. *Sov. Phys. JETP*, 15(8), 1962.

[12] J. E. Bjorkholm, R. R. Freeman, A. Ashkin, and D. B. Pearson. Observation of focusing of neutral atoms by the dipole forces of resonance-radiation pressure. *Phys. Rev. Lett.*, 41:1361–1364, Nov 1978.

[13] S. Chu, J. E. Bjorkholm, A. Ashkin, and A. Cable. Experimental observation of optically trapped atoms. *Phys. Rev. Lett.*, 57(3):314, 1986.

[14] T. Takekoshi, B. M. Patterson, and R. J. Knize. Observation of optically trapped cold cesium molecules. *Phys. Rev. Lett.*, 81(23):5105, 1998.

[15] R. Grimm, M. Weidemüller, and Y. B. Ovchinnikov. Optical dipole traps for neutral atoms. *Adv. in At. Mol. and Opt. Phys.*, 42:95–170, 2000.

[16] M. D. Barrett, J. A. Sauer, and M. S. Chapman. All-optical formation of an atomic bose-einstein condensate. *Phys. Rev. Lett.*, 87(1):010404, 2001.

[17] S. R. Granade, M. E. Gehm, K. M. O'Hara, and J. E. Thomas. All-optical production of a degenerate fermi gas. *Phys. Rev. Lett.*, 88(12):120405, 2002.

[18] K. Günter, T. Stöferle, H. Moritz, M. Köhl, and T. Esslinger. Bose-fermi mixtures in a three-dimensional optical lattice. *Phys. Rev. Lett.*, 96:180402, May 2006.

[19] R. Onofrio and C. Presilla. Ultracold atomic fermi–bose mixtures in bichromatic optical dipole traps: A novel route to study fermion superfluidity. *Jour. of Stat. Phys.*, 115(1-2):57–89, 2004.

[20] M. Çetinbaş. Emergence of decoherence by incoherent manifestation of coherent quantum fluctuations. *Jour. of Phys. A: Math. and Theor.*, 42(14):145302, 2009.

[21] K. L. Corwin, S. J. M. Kuppens, D. Cho, and C. E. Wieman. Spin-polarized atoms in a circularly polarized optical dipole trap. *Phys. Rev. Lett.*, 83(7):1311, 1999.

[22] J. Ye, H. J. Kimble, and H. Katori. Quantum state engineering and precision metrology using state-insensitive light traps. *science*, 320(5884):1734–1738, 2008.

[23] H. Katori, T. Ido, and M. Kuwata-Gonokami. Optimal design of dipole potentials for efficient loading of sr atoms. *Jour. of the Phys. Soc. of Japan*, 68(8):2479–2482, 1999.

[24] J. P. Gordon and A. Ashkin. Motion of atoms in a radiation trap. *Phys. Rev. A*, 21(5):1606, 1980.

[25] P. J. Ungar, D. S. Weiss, E. Riis, and S. Chu. Optical molasses and multilevel atoms: theory. *Jour. of the Opt. Soc. of Am. B*, 6(11):2058, November 1989.

[26] J. Dalibard and C. Cohen-Tannoudji. Laser cooling below the doppler limit by polarization gradients: simple theoretical models. *JOSA B*, 6(11):2023–2045, 1989.

[27] P. D. Lett, R. N. Watts, C. I. Westbrook, W. D. Phillips, P. L. Gould, and H. J. Metcalf. Observation of atoms laser cooled below the doppler limit. *Phys. Rev. Lett.*, 61(2):169–172, 1988.

[28] C. J. Foot. *Atomic physics*. Oxford University Press, 2005.

[29] K. M. O'Hara, S. R. Granade, M. E. Gehm, T. A. Savard, S. Bali, C. Freed, and J. E. Thomas. Ultrastable co_2 laser trapping of lithium fermions. *Phys. Rev. Lett.*, 82(21):4204, 1999.

[30] J. D. Miller, R. A. Cline, and D. J. Heinzen. Far-off-resonance optical trapping of atoms. *Phys. Rev. A*, 47(6):R4567, 1993.

[31] K. L. Corwin. *A Circularly-Polarized Optical Dipole Trap and Other Developments in Laser Trapping of Atoms*. PhD thesis, 1999.

[32] C. Cohen-Tannoudji and J. Dupont-Roc. Experimental study of zeeman light shifts in weak magnetic fields. *Phys. Rev. A*, 5(2):968, 1972.

[33] M. Zielonkowski, J. Steiger, U. Schünemann, M. DeKieviet, and R. Grimm. Optically induced spin precession and echo in an atomic beam. *Phys. Rev. A*, 58(5):3993, 1998.

[34] R. L. Kurucz. Kurucz Database. `http://www.pmp.uni-hannover.de/cgi-bin/ssi/test/kurucz/sekur.html`.

[35] Nist Database. `http://www.pmp.uni-hannover.de/cgi-bin/ssi/test/kurucz/sekur.html`.

[36] JE Sansonetti. Wavelengths, transition probabilities, and energy levels for the spectra of cesium (cs i-cs lv). *Journal of Physical and Chemical Reference Data*, 38(4):761, 2009.

[37] A Ashkin. Trapping of atoms by resonance radiation pressure. *Phys. Rev. Lett.*, 40:729–733, 1978.

[38] C. J. Myatt, N. R. Newbury, R. W. Ghrist, S. Loutzenhiser, and C. E. Wieman. Multiply loaded magneto-optical trap. *Opt. Lett.*, 21(4):290–292, 1996.

[39] Z. T. Lu, K. L. Corwin, M. J. Renn, M. H. Anderson, E. A. Cornell, and C. E. Wieman. Low-velocity intense source of atoms from a magneto-optical trap. *Phys. Rev. Lett.*, 77(16):3331, 1996.

[40] W. D. Phillips and H. Metcalf. Laser deceleration of an atomic beam. *Phys. Rev. Lett.*, 48(9):596, 1982.

[41] T. E. Barrett, S. W. Dapore-Schwartz, M. D. Ray, and G. P. Lafyatis. Slowing atoms with sigma-polarized light. *Phys. Rev. Lett.*, 67:3483–3486, 1991.

[42] W. Ertmer, R. Blatt, J. L. Hall, and M. Zhu. Laser manipulation of atomic beam velocities: Demonstration of stopped atoms and velocity reversal. *Phys. Rev. Lett.*, 54(10):996–999, 1985.

[43] M. Zhu, C. W. Oates, and J. L. Hall. Continuous high-flux monovelocity atomic beam based on a broadband laser-cooling technique. *Phys. Rev. Lett.*, 67:46–49, Jul 1991.

[44] W. Ketterle, A. Martin, M. A. Joffe, and D. E. Pritchard. Slowing and cooling atoms in isotropic laser light. *Phys. Rev. Lett.*, 69(17):2483, 1992.

[45] K. Dieckmann, R. J. C. Spreeuw, M. Weidemüller, and J. T. M. Walraven. Two-dimensional magneto-optical trap as a source of slow atoms. *Phys. Rev. A*, 58(5):3891, 1998.

[46] R. N. Watts and C. E. Wieman. Manipulating atomic velocities using diode lasers. *Opt. Lett.*, 11(5):291–293, 1986.

[47] D. Sesko, C. G. Fan, and C. E. Wieman. Production of a cold atomic vapor using diode-laser cooling. *JOSA B*, 5(6):1225–1227, 1988.

[48] M. De Labachelerie and G. Passedat. Mode-hop suppression of littrow grating-tuned lasers. *Appl. Opt.*, 32(3):269–274, 1993.

[49] C. E. Wieman and L. Hollberg. Using diode lasers for atomic physics. *Rev. of Sci. Inst.*, 62(1):1–20, 1991.

[50] T. Petelski, M. Fattori, G. Lamporesi, J. Stuhler, and G. M. Tino. Doppler-free spectroscopy using magnetically induced dichroism of

atomic vapor: a new scheme for laser frequency locking. *The Eur. Phys. Jour. D At. Mol. Opt. and Plasma Phys.*, 22(2):279–283, 2003.

[51] V. Rossin, E. Zucker, M. Peters, M. Everett, and B. Acklin. High-power high-efficiency 910 to 980 nm broad-area laser diodes. In *Las. and Appl. in Science and Engineering*, pages 196–202. International Society for Optics and Photonics, 2004.

[52] D. Mehuys, D. F. Welch, and L. Goldberg. 2.0 w cw diffraction-limited tapered amplifier with diode injection. *Elec. Lett.*, 28(21):1944–1946, 1992.

[53] W. Alt. An objective lens for efficient fluorescence detection of single atoms. *Opt.-Int. Jour. for Light and Elec. Opt.*, 113(3):142–144, 2002.

[54] S. Kuhr, W. Alt, D. Schrader, M. Müller, V. Gomer, and D. Meschede. Deterministic delivery of a single atom. *Science*, 293(5528):278–280, 2001.

[55] A. Louchet-Chauvet, J. Appel, J. J. Renema, D. Oblak, N. Kjaergaard, and E. S. Polzik. Entanglement-assisted atomic clock beyond the projection noise limit. *New Jour. of Phys.*, 12(6):065032, 2010.

[56] T. Loftus, C. A. Regal, C. Ticknor, J. L. Bohn, and D. S. Jin. Resonant control of elastic collisions in an optically trapped fermi gas of atoms. *Phys. Rev. Lett.*, 88(17):173201, 2002.

[57] M. W. Zwierlein, J. R. Abo-Shaeer, A. Schirotzek, C. H. Schunck, and W. Ketterle. Vortices and superfluidity in a strongly interacting fermi gas. *Nature*, 435(7045):1047–1051, 2005.

[58] A. Micheli, G. Pupillo, H. P. Büchler, and P. Zoller. Cold polar molecules in two-dimensional traps: Tailoring interactions with external fields for novel quantum phases. *Phys. Rev. A*, 76(4):043604, 2007.

[59] T. Kinoshita, T. Wenger, and D. S. Weiss. All-optical bose-einstein condensation using a compressible crossed dipole trap. *Phys. Rev. A*, 71(1):011602, 2005.

[60] M. P. A. Jones, J. Beugnon, A. Gaëtan, J. Zhang, G. Messin, A. Browaeys, and P. Grangier. Fast quantum state control of a single trapped neutral atom. *Phys. Rev. A*, 75(4):040301, 2007.

[61] R. Dumke, M. Volk, T. Müther, F. B. J. Buchkremer, G. Birkl, and W. Ertmer. Micro-optical realization of arrays of selectively addressable dipole traps: a scalable configuration for quantum computation with atomic qubits. *Phys. Rev. Lett.*, 89(9):097903, 2002.

[62] J. McKeever, J. R. Buck, A. D. Boozer, A. Kuzmich, H.-C. Nägerl, D. M. Stamper-Kurn, and H. J. Kimble. State-insensitive cooling and trapping of single atoms in an optical cavity. *Phys. Rev. Lett.*, 90:133602, Apr 2003.

[63] V. D. Ovsiannikov, V. G. Pal'chikov, A. V. Taichenachev, V. I. Yudin, H. Katori, and M. Takamoto. Magic-wave-induced $^1\mathbf{S}_0$-$^3\mathbf{P}_0$ transition in even isotopes of alkaline-earth-metal-like atoms. *Phys. Rev. A*, 75:020501, Feb 2007.

[64] U. Dammalapati, B. Santra, and L. Willmann. Light shifts and magic wavelengths for heavy alkaline earth elements: Ba and ra. *Jour. of Phys. B: At. Mol. and Opt. Phys.*, 45(2):025001, 2012.

[65] L. Yi, S. Mejri, J. J. McFerran, Y. Le Coq, and S. Bize. Optical lattice trapping of ^{199}hg and determination of the magic wavelength for the ultraviolet $^1s_0 \leftrightarrow ^3p_0$ clock transition. *Phys. Rev. Lett.*, 106(7):073005, 2011.

[66] M. S. Safronova, U. I. Safronova, and C. W. Clark. Magic wavelengths for optical cooling and trapping of lithium. *Phys. Rev. A*, 86(4):042505, 2012.

[67] N. Lundblad, M. Schlosser, and J. V. Porto. Experimental observation of magic-wavelength behavior of ^{87}rb atoms in an optical lattice. *Phys. Rev. A*, 81:031611, Mar 2010.

[68] C. Degenhardt, H. Stoehr, U. Sterr, F. Riehle, and C. Lisdat. Wavelength-dependent ac stark shift of the $^1s_0$- $^3p_1$ transition at 657 nm in ca. *Phys. Rev. A*, 70(2):023414, 2004.

[69] B. Arora, M. S. Safronova, and C. W. Clark. State-insensitive bichromatic optical trapping. *Phys. Rev. A*, 82(2):022509, 2010.

[70] E. Altman, W. Hofstetter, E. Demler, and M. D. Lukin. Phase diagram of two-component bosons on an optical lattice. *New Jour. of Phys.*, 5(1):113, 2003.

[71] M. Lewenstein, L. Santos, M. A. Baranov, and H. Fehrmann. Atomic bose-fermi mixtures in an optical lattice. *Phys. Rev. Lett.*, 92(5):050401, 2004.

[72] K. Pilch, A. D. Lange, A. Prantner, G. Kerner, F. Ferlaino, H. C. Nägerl, and R. Grimm. Observation of interspecies feshbach resonances in an ultracold *rb-cs* mixture. *Phys. Rev. A*, 79(4):042718, 2009.

[73] C. A. Stan, M. W. Zwierlein, C. H. Schunck, S. M. F. Raupach, and W. Ketterle. Observation of feshbach resonances between two different atomic species. *Phys. Rev. Lett.*, 93(14):143001, 2004.

[74] S. Inouye, J. Goldwin, M. L. Olsen, C. Ticknor, J. L. Bohn, and D. S. Jin. Observation of heteronuclear feshbach resonances in a mixture of bosons and fermions. *Phys. Rev. Lett.*, 93(18):183201, 2004.

[75] F. Ferlaino, C. D'Errico, G. Roati, M. Zaccanti, M. Inguscio, G. Modugno, and A. Simoni. Feshbach spectroscopy of a k-rb atomic mixture. *Phys. Rev. A*, 73(4):040702, 2006.

[76] S. Papp, J. Pino, and C. Wieman. Tunable miscibility in a dual-species bose-einstein condensate. *Phys. Rev. Lett.*, 101:040402, Jul 2008.

[77] A. J. Kerman, J. M. Sage, S. Sainis, T. Bergeman, and D. DeMille. Production and state-selective detection of ultracold rbcs molecules. *Phys. Rev. Lett.*, 92(15):153001, 2004.

[78] M. W. Mancini, G. D. Telles, A. R. L. Caires, V. S. Bagnato, and L. G. Marcassa. Observation of ultracold ground-state heteronuclear molecules. *Phys. Rev. Lett.*, 92(13):133203, 2004.

[79] A. Mosk, S. Kraft, M. Mudrich, K. Singer, W. Wohlleben, R. Grimm, and M. Weidemüller. Mixture of ultracold lithium and cesium atoms in an optical dipole trap. *Appl. Phys. B*, 73(8):791–799, 2001.

[80] M. Mudrich, S. Kraft, K. Singer, R. Grimm, A. Mosk, and M. Weidemüller. Sympathetic cooling with two atomic species in an optical trap. *Phys. Rev. Lett.*, 88(25):253001, 2002.

[81] G. Modugno, G. Ferrari, G. Roati, R. J. Brecha, A. Simoni, and M. Inguscio. Bose-einstein condensation of potassium atoms by sympathetic cooling. *Science*, 294(5545):1320–1322, 2001.

[82] J. Catani, L. De Sarlo, G. Barontini, F. Minardi, and M. Inguscio. Degenerate bose-bose mixture in a three-dimensional optical lattice. *Phys. Rev. A*, 77(1):011603, 2008.

[83] Z. Hadzibabic, C. A. Stan, K. Dieckmann, S. Gupta, M. W. Zwierlein, A. Görlitz, and W. Ketterle. Two-species mixture of quantum degenerate bose and fermi gases. *Phys. Rev. Lett.*, 88(16):160401, 2002.

[84] G. Roati, F. Riboli, G. Modugno, and M. Inguscio. Fermi-bose quantum degenerate k^{40}-rb^{87} mixture with attractive interaction. *Phys. Rev. Lett.*, 89(15):150403, 2002.

[85] T. Zelevinsky, S. Kotochigova, and J. Ye. Precision test of mass-ratio variations with lattice-confined ultracold molecules. *Phys. Rev. Lett.*, 100(4):043201, 2008.

[86] D. DeMille. Quantum computation with trapped polar molecules. *Phys. Rev. Lett.*, 88:067901, Jan 2002.

[87] JE Sansonetti. Wavelengths, transition probabilities, and energy levels for the spectra of rubidium (rbi through rbxxxvii). *J. Phys. Chem. Ref. Data*, 35(1):301–421, 2006.

[88] M. Taglieber, A.-C. Voigt, T. Aoki, T. W. Hänsch, and K. Dieckmann. Quantum degenerate two-species fermi-fermi mixture coexisting with a bose-einstein condensate. *Phys. Rev. Lett.*, 100:010401, Jan 2008.

[89] S. Aubin, S. Myrskog, M. H. T. Extavour, L. J. LeBlanc, D. McKay, A. Stummer, and J. H. Thywissen. Rapid sympathetic cooling to fermi degeneracy on a chip. *Nature Phys.*, 2(6):384–387, 2006.

[90] H. Shibata, N. Yokoshi, and S. Kurihara. Collective modes and stability of bose-fermi mixtures with a bcs-bec crossover. *Phys. Rev. A*, 75:053615, May 2007.

[91] J. J. Kinnunen and G. M. Bruun. Induced interactions in a superfluid bose-fermi mixture. *Phys. Rev. A*, 91:041605, Apr 2015.

[92] M. Zaccanti, C. D'Errico, F. Ferlaino, G. Roati, M. Inguscio, and G. Modugno. Control of the interaction in a fermi-bose mixture. *Phys. Rev. A*, 74:041605, Oct 2006.

[93] S. Tung, K. Jiménez-García, J. Johansen, C. V. Parker, and C. Chin. Geometric scaling of efimov states in a li^6-cs^{133} mixture. *Phys. Rev. Lett.*, 113(24):240402, 2014.

[94] S. Tung, C. Parker, J. Johansen, C. Chin, Y. Wang, and P. S. Julienne. Ultracold mixtures of atomic ^6li and ^{133}cs with tunable interactions. *Phys. Rev. A*, 87:010702, Jan 2013.

[95] E. Wille, F. M. Spiegelhalder, G. Kerner, D. Naik, A. Trenkwalder, G. Hendl, F. Schreck, R. Grimm, T. G. Tiecke, J. T. M. Walraven, et al. Exploring an ultracold fermi-fermi mixture: Interspecies feshbach

resonances and scattering properties of li^6 and k^{40}. *Physical review letters*, 100(5):053201, 2008.

[96] I. Ferrier-Barbut, M. Delehaye, S. Laurent, A. T. Grier, M. Pierce, B. S. Rem, F. Chevy, and C. Salomon. A mixture of bose and fermi superfluids. *Science*, 345(6200):1035–1038, 2014.

[97] J. P. D'Incao and B. D. Esry. Enhancing the observability of the efimov effect in ultracold atomic gas mixtures. *Phys. Rev. A*, 73:030703, Mar 2006.

[98] M. Aymar and O. Dulieu. Calculation of accurate permanent dipole moments of the lowest $^{1,3}\sum^+$ states of heteronuclear alkali dimers using extended basis sets. *The Jour. of Chem Phys.*, 122(20):204302, 2005.

[99] P. M. Duarte, R. A. Hart, J. M. Hitchcock, T. A. Corcovilos, T. L. Yang, A. Reed, and R. G. Hulet. All-optical production of a lithium quantum gas using narrow-line laser cooling. *Phys. Rev. A*, 84(6):061406, 2011.

[100] R. Onofrio and C. Presilla. Reaching fermi degeneracy in two-species optical dipole traps. *Phys. Rev. Lett.*, 89(10):100401, 2002.

[101] L. J. LeBlanc and J. H. Thywissen. Species-specific optical lattices. *Phys. Rev. A*, 75(5):053612, 2007.

[102] M. Repp, J. Pires, R.and Ulmanis, R. Heck, E. D. Kuhnle, M. Weidemüller, and E. Tiemann. Observation of interspecies ^6li-^{133}cs feshbach resonances. *Phys. Rev. A*, 87(1):010701, 2013.

[103] K. L. Corwin, Z. Lu, C. F. Hand, R. J. Epstein, and C. E. Wieman. Frequency-stabilized diode laser with the zeeman shift in an atomic vapor. *Appl. Opt.*, 37(15):3295–3298, 1998.

[104] N. Schlosser, G. Reymond, I. Protsenko, and P. Grangier. Sub-poissonian loading of single atoms in a microscopic dipole trap. *Nature*, 411(6841):1024–1027, 2001.

[105] A. Micheli, G. K. Brennen, and P. Zoller. A toolbox for lattice-spin models with polar molecules. *Nature Phys.*, 2(5):341–347, 2006.